

1995

Electronic and photonic devices: experimental investigations of hydrogenated amorphous silicon substrate n+/i/p+ solar cell and fundamental properties of quantum wells with cylindrical geometry and applications to electronics and photonics

Er-Xuan Ping
Iowa State University

Follow this and additional works at: <https://lib.dr.iastate.edu/rtd>

 Part of the [Condensed Matter Physics Commons](#), [Electrical and Electronics Commons](#), [Materials Science and Engineering Commons](#), and the [Oil, Gas, and Energy Commons](#)

Recommended Citation

Ping, Er-Xuan, "Electronic and photonic devices: experimental investigations of hydrogenated amorphous silicon substrate n+/i/p+ solar cell and fundamental properties of quantum wells with cylindrical geometry and applications to electronics and photonics " (1995). *Retrospective Theses and Dissertations*. 11078.

<https://lib.dr.iastate.edu/rtd/11078>

This Dissertation is brought to you for free and open access by the Iowa State University Capstones, Theses and Dissertations at Iowa State University Digital Repository. It has been accepted for inclusion in Retrospective Theses and Dissertations by an authorized administrator of Iowa State University Digital Repository. For more information, please contact digirep@iastate.edu.

INFORMATION TO USERS

This manuscript has been reproduced from the microfilm master. UMI films the text directly from the original or copy submitted. Thus, some thesis and dissertation copies are in typewriter face, while others may be from any type of computer printer.

The quality of this reproduction is dependent upon the quality of the copy submitted. Broken or indistinct print, colored or poor quality illustrations and photographs, print bleedthrough, substandard margins, and improper alignment can adversely affect reproduction.

In the unlikely event that the author did not send UMI a complete manuscript and there are missing pages, these will be noted. Also, if unauthorized copyright material had to be removed, a note will indicate the deletion.

Oversize materials (e.g., maps, drawings, charts) are reproduced by sectioning the original, beginning at the upper left-hand corner and continuing from left to right in equal sections with small overlaps. Each original is also photographed in one exposure and is included in reduced form at the back of the book.

Photographs included in the original manuscript have been reproduced xerographically in this copy. Higher quality 6" x 9" black and white photographic prints are available for any photographs or illustrations appearing in this copy for an additional charge. Contact UMI directly to order.

UMI

A Bell & Howell Information Company
300 North Zeeb Road, Ann Arbor, MI 48106-1346 USA
313:761-4700 800:521-0600

**Electronic and photonic devices: Experimental investigations of hydrogenated
amorphous silicon substrate n⁺/i/p⁺ solar cell and fundamental properties of
quantum wells with cylindrical geometry and applications to
electronics and photonics**

by

Er-Xuan Ping

**A Dissertation Submitted to the
Graduate Faculty in Partial Fulfillment of the
Requirement for the Degree of
DOCTOR OF PHILOSOPHY**

Department: Electrical and Computer Engineering

Major: Electrical Engineering (Microelectronics)

Approved:

Signature was redacted for privacy.

In Charge of Major Work

Signature was redacted for privacy.

For the Major Department

Signature was redacted for privacy.

For the Graduate College

**Iowa State University
Ames, Iowa**

1995

UMI Number: 9610979

UMI Microform 9610979
Copyright 1996, by UMI Company. All rights reserved.

**This microform edition is protected against unauthorized
copying under Title 17, United States Code.**

UMI

**300 North Zeeb Road
Ann Arbor, MI 48103**

TABLE OF CONTENTS

GENERAL INTRODUCTION	1
PART 1. EXPERIMENTAL INVESTIGATIONS OF HYDROGENATED AMORPHOUS SILICON SUBSTRATE n⁺/i/p⁺ SOLAR CELLS	2
1. INTRODUCTION	3
Statement of purpose	3
Overview	3
2. a-Si:H FILM AND SOLAR CELL BY TRIODE PECVD	8
General properties of a-Si:H material	8
The Triode PECVD system	12
Typical a-Si:H film by triode PECVD	14
The physics of a-Si:H solar cell	18
3. SUBSTRATE a-Si:H SOLAR CELL	26
The advantages of substrate a-Si:H solar cells	26
The indium-tin-oxide transparent conductive film	27
The substrate a-Si:H solar cell	30
Effects of front contacts	31
Effects of p ⁺ /i interface smoothing	33
Effects of the I layer thickness	37
Effects of ppm boron compensation in the I layer	41
Effects of temperature grading	44
Effects of the n ⁺ layer as a template layer	49
4. CONCLUSIONS	56
PART 2. FUNDAMENTAL PROPERTIES OF QUANTUM WELLS WITH CYLINDRICAL GEOMETRY AND THEIR APPLICATIONS TO ELECTRONICS AND PHOTONICS	57
5. INTRODUCTION	58

Statement of purpose	58
Overview	58
6. BASIC THEORY	64
The band structure of III-V semiconductor compounds	64
The envelope function approximation	65
Basic properties of QW	67
Applications of QW	70
7. FUNDAMENTAL PROPERTIES OF CQW	73
Energy levels of CQW	73
Tunneling in CQW	82
Analog systems in electromagnetism	99
8. CONCLUSIONS	100
GENERAL CONCLUSIONS	101
REFERENCES	102
ACKNOWLEDGMENTS	108

GENERAL INTRODUCTION

In the current knowledge explosion era, a successful individual needs skills in interdisciplinary fields. In some fields of electrical engineering, such as microelectronics, knowledge of physics, materials and sometimes even business are demanded for a person who can now hardly be distinguished between an engineer or a scientist. It is the belief of the current author that this trend will continue. It is this belief that motivated the author to study two seemingly unrelated subjects in one single thesis. One topic deals with traditional solar energy conversion by photovoltaic devices, and the other deals with an unexplored subject, geometry effects in quantum well structures.

This thesis is organized as follows: Part I), experimental investigations of hydrogenated amorphous silicon substrate $n^+/i/p^+$ solar cells. This section starts with an introduction that discusses the purpose of the work and gives an overview of the subject. This is then followed by a description of the fabrication and characterization techniques used in this work. Finally, the results and conclusions are presented. Part II), fundamental properties of quantum wells in cylindrical geometry and applications to electronics and photonics. This part includes an introduction containing a statement of purpose and an overview of the project. This is followed by a discussion of the methods which have been applied to study the particular structures. The analytical results, along with the several proposed applications in electronics and photonics, are presented in the subsequent sections. The thesis is concluded by a general conclusion.

**PART 1: EXPERIMENTAL INVESTIGATIONS OF HYDROGENATED
AMORPHOUS SILICON SUBSTRATE $n^+/i/p^+$ SOLAR CELLS**

1. INTRODUCTION

Statement of purpose

This work was aimed at developing a technique for fabricating substrate $n^+/i/p^+$ solar cells based on hydrogenated amorphous silicon (a-Si:H) material and to look for alternatives, by designing better structure, to improve the device stability which is a long standing technological problem encountered in the photovoltaic applications of a-Si:H solar cells. More specifically, this work was to show a very original idea that the active part of the device can provide more stable performance if it is grown on the top of a template layer which provides the needs for a better a-Si:H network. The significance of this idea is that the midgap a-Si:H cell in a tandem cell will not suffer from the degradation under prolonged light exposure when the bottom solar cell is designed properly and provides the template layer, such as a cell made by microcrystalline silicon ($\mu\text{c-Si}$).

Overview

Everything is a compromise and so is the a-Si:H based technology. While it enjoys the advantages of mass production and low temperature processing, it suffers the major drawback that a-Si:H material depends critically on the fabrication history as well as the environment it encounters. The study of amorphous semiconductors began in the 50's and 60's when growth technologies were becoming mature and the semiconductor industry was emerging. Silicon (Si), one of the most abundant materials which happens to fall into the category of a semiconductor, has been a material to be studied for many applications. In the late 60's [1], the study of non-crystalline Si started and resulted in several significant advances. Since then, enormous progress has been achieved and a large amount of experimental data has been accumulated. The a-Si:H photovoltaic technology, which aims at efficient energy conversion from non polluting sun light, was developed in the midst of the booming of a-Si:H research. Today, the energy conversion devices, solar cell in its conventional name, is being seen in many places from simple calculators to large solar plants in the desert.

The desire to eliminate potential energy problems in the future as well as the pollution

problems of conventional energy sources has been the main motivation to achieve high stable efficiency solar cells made from materials that could be deposited in the form of thin films. Due to the high absorption of a-Si:H material for the visible light, a-Si:H solar cells can be made as thin as 10^{-4} cm. The first a-Si:H solar cell [2] was made after successful doping of a-Si:H by boron (p type) and phosphorus (n type) in the presence of hydrogen was achieved. The hydrogen effectively reduces the defect states in the material so that the Fermi level can be moved [3]. As the research continued, it was realized that the single junction a-Si:H solar cell encountered limitations. Later on, a window concept [4] was introduced which involved alloying of a-Si:H with carbon so that the light absorbed in the p^+ layer could be minimized. Texturing the surface of the electrodes [5] was then introduced to yield high efficiency by trapping the light in the cell and keeping the minimum path for the photo-generated carriers to travel under the internal electric field. With anti-reflection coating on the surface, the conversion efficiency reached more than 11 %. The next step was to grade the p^+/i interface so that the p^+ and intrinsic (I) layers are smoothly connected and the interface states are reduced [6]. To achieve even higher conversion efficiency, highly conductive p^+ and n^+ layers are required to further reduce the carrier losses. This is where low-temperature deposited $\mu\text{-Si}$ plays an important role. The multilayer nature of the solar cell indicates that the interfaces among different layers are important, especially for the stability of the device. It is now realized that the limit of 15% stable efficient solar cell based on a-Si:H and its alloys will very likely be achieved by the tandem cell [7] in which light is effectively broken into several sections and collected effectively in each region.

One of the major problems of a-Si:H based solar cells is the unstable performance when subjected to prolonged light exposure. This is the result of the Staebler-Wronski effect [8]. The structural and electronic properties of a-Si:H material are degraded under illumination. The mechanism of this phenomenon is still under debate. Many have believed that the weak bonds in the a-Si:H network are broken by the recombination of the photo-generated electron and hole pairs in the vicinity of the weak bonds and more defect states are created [9]. These defect states can be eliminated again by thermal treatment, and the original

properties of the material are recovered. The creation of defect states causes several consequences for the a-Si:H solar cell. It first creates recombination centers for the photo-generated electrons and holes, and therefore reduces the probability for collect them. Second, it changes the previously optimized structure which provides the electric field in the solar cell. Finally, the change of material quality also affects the interfaces between different layers. When the interface is degraded, the space-charge region is reduced and the internal electric field decreases.

In general, there are two approaches to improve the stability of a-Si:H solar cells. The first is to improve the material quality so that the degradation of a-Si:H can be minimized. This is usually done by controlling the chemistry during the growth. It was found that a-Si:H films grown by electron cyclotron resonance (ECR) remote plasma deposition are more stable when subjected to light soaking [10]. The deposition method is used to control the surface chemical reaction in a regime that yields fewer unwanted radicals. It was recently proposed and demonstrated that $\mu\text{c-Si}$ material yields more stable solar cells by virtually eliminating the weak bonds [11].

Another approach is to design the device properly so that a strong electric field exists inside the cell, and the photo-generated electrons and holes would still be swept to the p^+ and n^+ regions even in the presence of increasing defect states. This is usually done by reducing the thickness of the I layer, introducing band grading by compositional variation and change of growth conditions such as the temperature, and invoking highly conductive $\mu\text{c-Si } n^+$ and p^+ layers so that a strong electric field can be built up. In general, $\mu\text{c-Si}$ meets the material requirement and yields the strong electric field. It is expected to be the future path toward stable, efficient solar cells after the following problems are solved: a) the interfacing with the I layer; b) the alloying with C and Ge, and the doping of these alloys; c) the tunneling junctions; d) the control of thickness.

Another important application of a-Si:H material is the thin-film transistor [12] which is widely used in flat panel displays. The operation of an a-Si:H TFT is very different from that of crystalline MOSFET due to the defective nature of a-Si:H. However, an a-Si:H TFT

usually displays similar behavior to the crystalline MOSFET in the normal operation condition. When the operation speed becomes high, the defective nature of a-Si:H starts to affect the performance of the a-Si:H TFT. Similar to a-Si:H solar cells, a-Si:H TFT's also face the degradation of performance after prolonged usage. The predominant effect is the shifting of the threshold voltage. This is due to the collision between high speed electrons and the a-Si:H network, leading to the breaking of the weak bonds and creation of defect states. Therefore, the voltage required to accumulate same amount of electrons near the channel moves toward a large value. This problem can be improved by realizing the asymmetric nature of the conduction and valence tail states [13]. When one incorporates metals that create a positive Schottky barrier which depletes the electron away from the a-Si:H, an internal electric field is induced. This electric field extends into the a-Si:H active layer. As the defect states increase after prolonged usage, the amount of electrons depleted from the valence tail state into the metal is larger than the electrons that are needed to fill the conduction tail states. Therefore, an additional electric field is induced, which compensates the electric field that is needed to accumulate same amount electrons near the channel after the increase of defect states. Figure 1.1 shows two different designs. In the left one, the electric field at the surface of the a-Si:H active layer is diminished to a very small value due to the passivation by the insulator, such as SiO_2 and Si_3N_4 . In the right design, the metal on the top of the a-Si:H active layer creates an electric field which extends into the active layer. The numerical results, shown in Figure 1.2, demonstrate that the change of the critical electric field that is needed to align the Fermi level with the conduction band edge, which is also proportional to the shift of threshold voltage, is

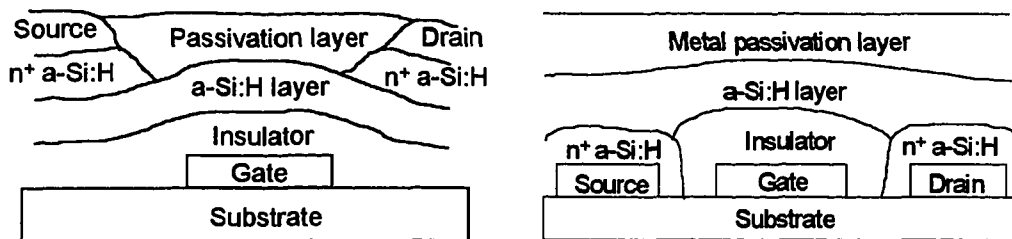


Figure 1.1. Two different designs of a-Si:H TFT using different passivation layers.

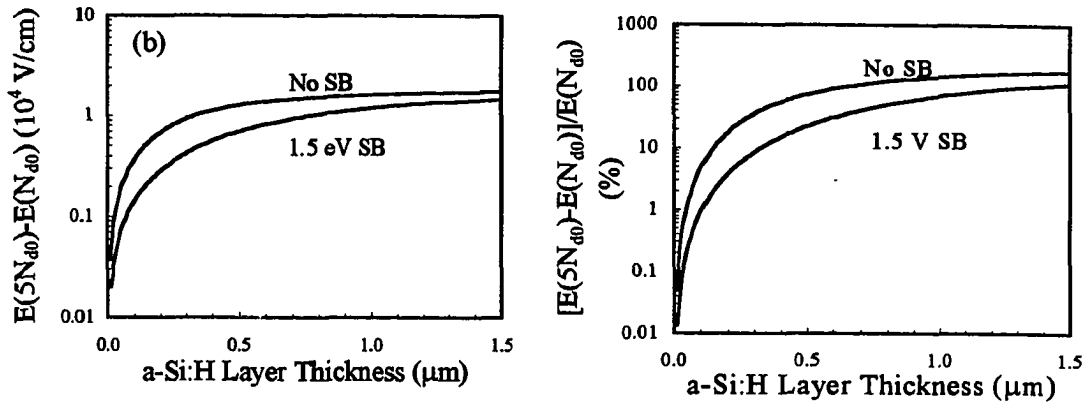


Figure 1.2. The change of the critical electric field for a virgin (N_{d0}) and degraded ($5N_{d0}$) a-Si:H active layer as a function of the a-Si:H active layer thickness of the a-Si:H TFT structure in Figure 1.1. The Schottky barriers are 0 and 1.5 eV.

improved by a factor of 4 for a 0.3 μm thick a-Si:H active layer, in the presence of a degradation that the defect states increase by a factor of five.

2. a-Si:H FILM AND SOLAR CELL BY TRIODE PECVD

General properties of a-Si:H material

a-Si:H material is a disordered network originating from the topological arrangement of Si atoms and the compositional substitution of other atoms as shown in Figure 2.1a. If one starts to consider a-Si:H in terms of crystals such as the band theory, one finds that the absence of the symmetry makes the task impossible. However, a-Si:H does show some features that a crystal displays, such as being transparent and opaque to certain light. Due to the lack of symmetry, a-Si:H has no crystal direction and the electron transition excited by photon absorption is a direct process, leading to a high absorption. The bonding theory [14,15] successfully explains many a-Si:H phenomena. The basic picture is shown in Figure 2.1b. The discrete energy levels of the single atom start to overlap each other as more and more atoms are brought together. When the wavefunction of each atom shares the same symmetry, the energy levels tend to stay close. Since only two symmetries are involved, the states distinguish themselves into two sets, the conduction band and the valence band. Meanwhile, the disordered nature of the material also introduces states in the middle, resulting in a continuum distribution of defect states.

In the presence of hydrogen, the quality of a-Si:H meets the general requirements for electronic and optical applications. What hydrogen does is to find the unbounded Si bonds in the network, also called dangling bonds, and to attach them to make the local charge neutral.

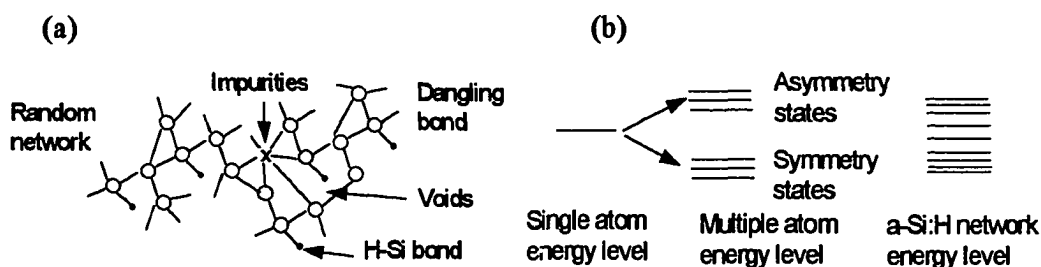


Figure 2.1. Schematic of a-Si:H network and the bonding theory to describe the network.

Hydrogen also does chemical etching during the growth and makes the a-Si:H network more homogenous. When the hydrogen content in the a-Si:H network reaches about 10% atomic weight, the midgap defect states are on the order of $10^{15} \text{ cm}^{-3} \text{ eV}^{-1}$. This gives reasonably good carrier transportation properties such as the carrier lifetime and mobility. Figure 2.2 shows the density of states (DOS) for an a-Si:H network which has been shown in the literature [16]. It generally consists of three different segments. The one with DOS larger than $10^{21} \text{ cm}^{-3} \text{ eV}^{-1}$ is called extended states in which carriers behave like in a crystal. The states follow the extended states are called tail states. They are usually expressed as an exponential function of energy. The slopes of the exponential functions, often called Urbach energy, are about 25 and 50 meV for conduction and valence band tail states, respectively. The final segment is called midgap states which is about $10^{15} \text{ cm}^{-3} \text{ eV}^{-1}$ for high quality a-Si:H. It should be pointed out that this DOS is a simplified version of real materials which usually show more complicated distribution of the states.

The doping of a-Si:H is achieved by introducing dopants such as boron and phosphorus during the growth. The dynamics of the doping process in a-Si:H is very complicated due to the defective nature of a-Si:H and research in this subject encounters difficulties. Usually, there are two positions that the dopant atoms can go. When the dopant atoms replace the Si site in the network, they are electrically active. Due to the random nature of the network, the dopant can also occupy sites in which the bonds of the dopant atom are satisfied by appropriate numbers of Si bonds. The dopant is therefore electrically inactive and results in defect states instead. At normal growth conditions, only few percent of the dopant

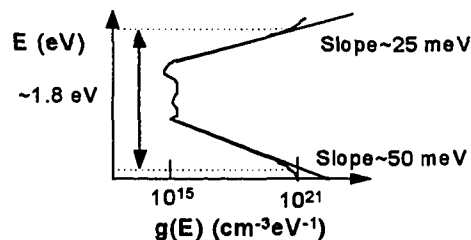


Figure 2.2. The density of states of a-Si:H network.

in the network serve as electrically active centers while the majority of the dopants are buried in the network as defect centers.

Due to the difference in the tail states, a-Si:H is easier to dope n-type than p-type. As a result, the activation energy of n-type a-Si:H is smaller than that of p-type a-Si:H. Table 2.1 lists general quantities of intrinsic, n- and p-type a-Si:H that are the most important for device applications [17].

Table 2.1 Common electronic and optical properties of a-Si:H material.

Intrinsic a-Si:H		Doped a-Si:H	
Tauc's Gap	1.7 eV	B Concentration	10^{-2} ~1 %
E_{04} *	1.8 eV	Conductivity	10^{-4} ~ 10^{-2} S/cm
Photo-conductivity **	10^{-4} S/cm	Activation energy	0.3~0.5 eV
Dark-conductivity	10^{-10} S/cm	P Concentration	10^{-2} ~1 %
Activation energy	0.85 eV	Conductivity	10^{-3} ~ 10^{-1} S/cm
Electron Mobility	$1 \text{ cm}^2\text{V}^{-1}\text{S}^{-1}$	Activation energy	0.1~0.3 eV
Hole mobility	$0.01 \text{ cm}^2\text{V}^{-1}\text{S}^{-1}$		
Refractive Index	3.6, $\lambda > 1000 \text{ nm}$		
Absorption	$>10^4 / \text{cm}$, $\lambda < 700 \text{ nm}$		

* Energy band gap at absorption coefficient equal to $10^4 / \text{cm}$.

** Under $100 \text{ mW}/\text{cm}^2$ (AM1.5) Light Intensity

Freshly deposited made a-Si:H films meet the general requirements for electronic and optical applications. However, the quality of the material degrades as the time passes, especially when the film is exposed to energetic species such as light and high speed electrons. It was first observed by Staebler and Wronski [8] that the photo-conductivity of a-Si:H made by glow-discharge deposition decreases under the illumination and so does the dark conductivity. The process is reversible by the heat treatment (100 - 200 °C). Several models have been developed to explain this phenomena. The most common point of view is that the

structure of a-Si:H network is changed due to the energetic species, resulting in the creation of defect states in the midgap. One particular process is shown in Figure 2.3. In the a-Si:H network, the weak bonds are broken by the energetic species, resulting in dangling bonds. Carriers in the vicinity of the dangling bonds tend to be more localized and the transportation properties are therefore deteriorated. At elevated temperature, the migration of hydrogen becomes active and the probability for the hydrogen to meet the dangling bonds is increased. The local charge neutrality is preserved when hydrogen attaches to the dangling bonds.

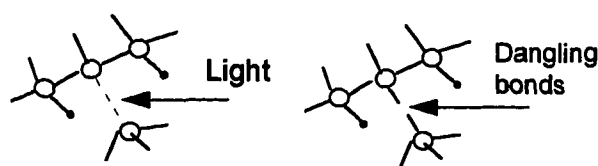


Figure 2.3. The creation of defect states in the presence of energetic source (light) to break the weak bonds, create dangling bonds in the a-Si:H network.

a-Si:H has many unique features that make it suitable for electronic and optical applications, especially for solar cells. However, high performance a-Si:H solar cells rely on the usage of a-Si:H alloys. It has been found that introducing certain amounts of germanium and carbon, which are also column IV materials, can change the electrical and optical properties dramatically. Table 2.2 summarizes some general properties of a-(Si,Ge):H and a-(Si,C):H alloys [18]. One common feature of these alloys is that the electronic transport properties are not as good as a-Si:H. In a-(Si,Ge):H, the weak Ge-H bond makes it difficult

Table 2.2. Common properties of a-(Si,Ge):H and a-(Si,C):H alloys.

	a-Si _{1-x} Ge _x :H	a-Si _{1-x} C _x :H
x	0.4	0.1
E _{Tauc}	1.5 eV	2.0 eV
σ _D	10 ⁻⁹ S/cm	10 ⁻¹² S/cm
σ _L	10 ⁻⁵ S/cm	10 ⁻⁷ S/cm

for hydrogen to be incorporated into the network and leaves a large number of midgap states. In a-(Si,C):H, the strong C-H bond tends to prevent carbon from attaching to Si. This deteriorates the local homogeneity and results in many tail and midgap states. The study of a-Si:H alloys in recent years has advanced our understanding of those materials and good quality a-Si:H alloys are being made to yield high performance tandem solar cells. This raises the hope that thin film solar cells will eventually replace conventional energy sources.

The triode PECVD system

Although many deposition methods have been developed and used to yield high quality a-Si:H material, currently most common deposition method is to use glow-discharge deposition powered by radio frequency (RF) field. This is also called plasma enhanced chemical vapor deposition (PECVD). The resultant material usually has high absorption for visible light, low midgap states, reasonable large carrier diffusion length, and fairly large carrier mobility. Figure 2.4a is a schematic of the triode geometric PECVD system used for this study. The system consists of three major components, a) the vacuum system which includes the chamber and pumps; b) the RF power supply and the matching network; c) the gas system in which various gases for the deposition are guided into the reactor. The physical process of a glow discharge is as follows. Under the RF field, the gas in the chamber is excited. When the pressure of the gas exceeds certain value, the mean free path of the gas is smaller than the distance to excite the gas and the plasma starts to glow by the transfer of the energy between the RF field and the bound electrons. Due to the difference in the area between the cathode and anode, the charges collected by them are not equal and a DC bias is induced. As the loss of electrons from the plasma to the anode is very rapid, a space charge region is developed and those positively charged particles, along with other radicals, are attracted toward the substrate, leading to the growth of the film. Unlike the diode geometry, the triode configuration can minimize the ion collision damage at the surface.

The growth chemistry of a-Si:H by triode PECVD is a complicated process and no complete study has been done. It is generally believed that the growth of a-Si:H occurs in a stacking manner as shown in Figure 2.4b. The silane gas is broken into various radicals and

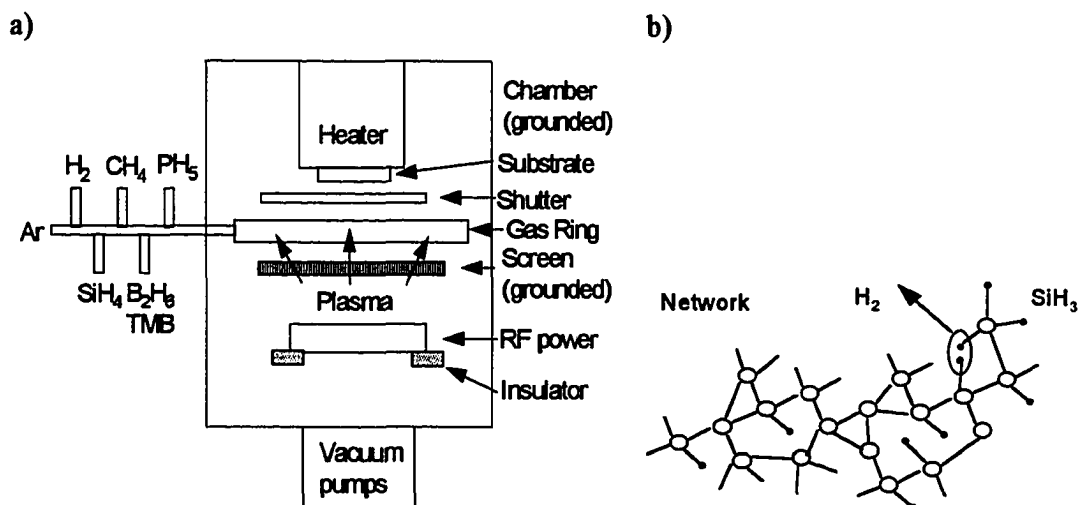


Figure 2.4 Schematic of the triode geometric PECVD system and the major reaction on the surface.

they start to approach the surface of the substrate. Some of the radicals find the place where the bonding is missing and attach to it. Meanwhile, the hydrogen in the network finds its way to combine as H_2 gas and leaves the surface. In the midst of this process, other radicals also exist and they usually have a negative influence on the a-Si:H network by forming clusters and voids. Therefore, the improved techniques to grow a-Si:H should limit unwanted radicals to the minimum. As such, photo-CVD could be used to provide better film since the control of the light energy can be used to break silane into the species that are desired. ECR remote plasma deposition, which controls the radicals arriving at the surface, yields better film as well.

Typical a-Si:H film by triode PECVD

The decomposition of pure silane by an RF field in glow discharge deposition gives the best large area a-Si:H film. It was realized that high quality a-Si:H is obtained at growth temperatures between 250~300 °C. The main reason for this is the balance between hydrogen surface mobility and the surface chemical etching. A film was grown on precleaned 7059 glass by the triode RF glow discharge system. Table 2.3 lists the processing parameters.

Table 2.3. Processing parameters of an a-Si:H film by the triode PECVD system

Temperature	300 °C
SiH ₄ flow rate	8 sccm
RF power	20 W/250 cm ²
Pressure	16 mT
Growth rate	1.3 Å/s
Growth time	90 min

After the film was deposited, the transmission and reflection spectra, along with the optical density which was used to determine the absorption, were measured. The transmission is used to determine the thickness of the film. This is done by using the interference peaks at long wavelength where the refractive index does not change much. A chromium contact was deposited by high vacuum thermal evaporation in coplanar geometry and followed by silver paint. Chromium is a good Ohmic contact to a-Si:H and does not react with silicon to form silicide as aluminum does. After the film with the contact was annealed at 170 °C for 30 min, the photo- (under 100 mW/cm² ELH light) and dark-conductivity were measured. These were found to be 2.1×10^{-5} and 1.8×10^{-10} S/cm, respectively. Activation energy was determined by measuring the dark current under a constant applied voltage for different temperature. The current collected is $i = q(n\mu_e + p\mu_h)$ for intrinsic a-Si:H. Since the electron mobility is much larger than the hole mobility in a-Si:H, the current is determined by electrons or $i \sim qn\mu_e(T)$. The majority of the electrons collected are those in the extended states since the mobility in the tail and middle states is relatively small. The number of the electrons collected depends on the number of the electrons thermally excited in the conduction band and the DOS of the conduction band. The combined temperature dependence of the conduction band DOS and the electron mobility does not show strong variations in temperature while the thermal excitation, usually described by $\exp(-E/kT)$, dominates the temperature behavior. E is the activation energy which is approximately the distance between the Fermi level and the

conduction mobility edge. One can thus extract this activation energy from the temperature dependent dark conductivity, which is 0.84 eV for the film.

The transmission and reflection spectra were measured by a λ -9 spectrophotometer. The measurement is accurate only for large absorption. For small absorption, the light will be either transmitted or reflected and the absorption is too small to be accurately determined. This region is called subgap absorption. Usually, the so called two beam technique [19] is used to measure the subgap absorption. In this technique, a monochromatic light source is introduced on the film to produce photo-current or $i=q(n\mu_e+p\mu_h)$ for intrinsic a-Si:H. Once again, the majority contribution to the current is from the electrons or $i\sim qn\mu_e(E)$. The mobility of electrons depends strongly on the energy position in the band diagram. For electrons in the extended states, the bulk mobility applies. For electrons in the tail and midgap states, the mobility varies. However, when a second DC white beam is applied, the midgap states are filled and the quasi Fermi levels are effectively split. Therefore, the current generated by the signal is directly proportional to the number of the electrons excited from the valence tail states to the conduction band. The number of electrons excited is proportional to the light absorbed, or $I_0(1-e^{-\alpha d})$, where α is the absorption coefficient and d is the thickness of the film. If $\alpha d \ll 1$, then the current measured is proportional to the absorption coefficient. By matching the absolute absorption coefficient obtained from the spectrophotometer in the range of 1.7~1.8 eV where αd is about 0.2 for a 1 μm film, the subgap absorption coefficient can be obtained. Figure 2.5 shows the absorption coefficient of the film as a function of the energy, with a 53 meV slope in the 1.5~1.7 eV range.

As discussed earlier, newly deposited a-Si:H meets the general requirements for electronic and optical applications. However, when a-Si:H is exposed to light or high speed electrons, the quality of the material degrades. When one measures the transient photo-current under illumination, one finds a decrease of photo-current. Figure 2.6 shows the normalized transient photo-current of the a-Si:H film measured under 100 mW/cm² ELH light. A 75 % decrease is observed within the illumination time of 1 hour.

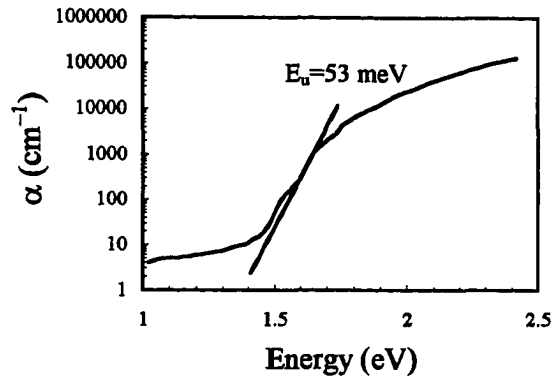


Figure 2.5. The absorption coefficient of the a-Si:H film by λ -9 spectrophotometer and the subgap measurement.

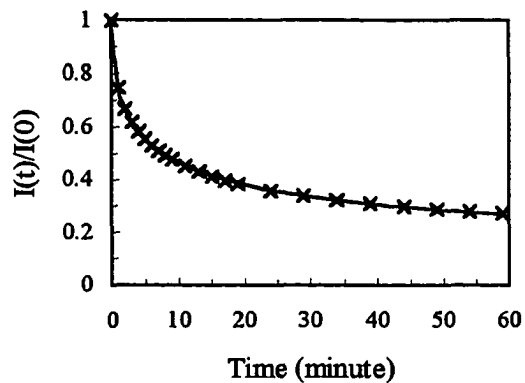


Figure 2.6. The normalized transient photo-current under 100 mW/cm^2 ELH light.

The real degradation requires longer illumination time. Since the light source (ELH lamp operated at 110 V) has limited lifetime, it is appropriate to use concentrated light to accelerate the degradation. The film was then placed under 1 W/cm^2 ELH light. Lenses are used to intensify the light. The calibration of the light intensity was done by placing a standard cell under the intensified light to yield a current reading about 10 times larger than the reading of the standard cell under 100 mW/cm^2 ELH light. The photo-current under 1 W/cm^2 light is measured up to 20 hours, resulting in a 85 % drop in the photo-current shown in Figure 2.7. Another way to see the degradation of an a-Si:H film is to measure the subgap

absorption. The increase of defect states results in a high subgap adsorption. Figure 2.7 shows the measured subgap absorption by the two beam technique for the virgin and 15 hour light soaked film. It is clearly demonstrated that the defect states in the midgap increases by about one order of magnitude. If one integrates the defect states over subgap energy range, the total defect states would increase by one order of magnitude which will result in a decrease of the photo-conductivity by one order of magnitude.

The degraded film was then placed into an oven at 150 °C in the air ambient. Figure 2.8

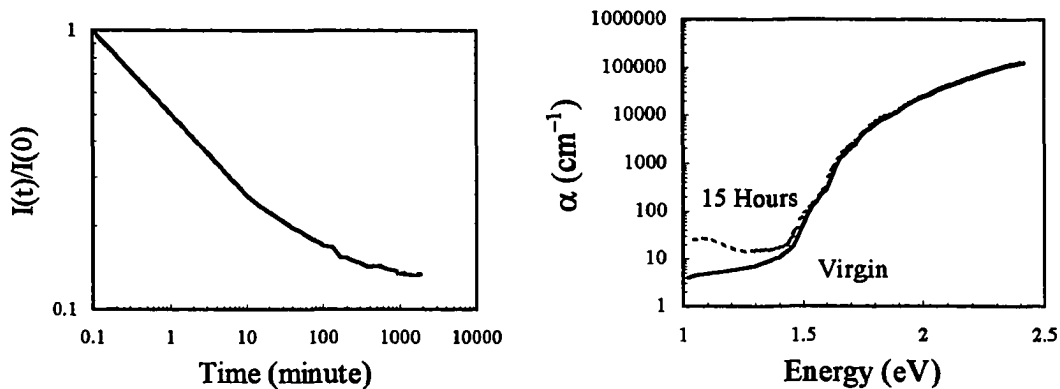


Figure 2.7. The normalized transient photo-current under 1 W/cm^2 ELH light and the absorption coefficient for the virgin and 15 hour light soaked time.

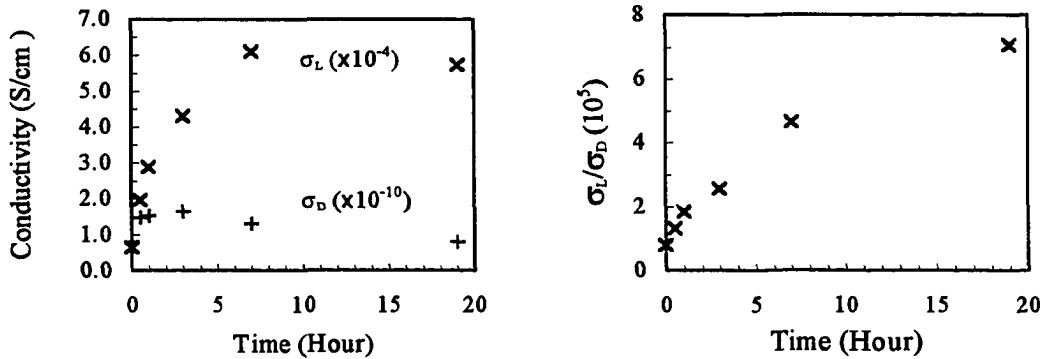


Figure 2.8. The annealing of the dark- and photo-conductivity and the photosensitivity of the degraded film at 150 °C of air ambient.

shows the dark-conductivity, photo-conductivity and photosensitivity as a function of annealing time. One notices that the dark-conductivity and photo-conductivity both increase initially, indicating the recovery of electronic properties. One also notices that a further annealing reduces the dark-conductivity after 3 hours and the photo-conductivity after 7 hours. However, the photosensitivity increases steadily, indicating that more and more dangling bonds are passivated.

The physics of a-Si:H solar cell

The basic requirement of solar cells is to extract energy from the sunlight. They are structures that respond to light to yield a noticeable reaction. The p-n junction is suitable for this purpose [20]. The basic process is that when light enters the material, electrons and holes are generated in the area of the junction. These carriers start to diffuse toward p and n sides due to the carrier density gradient. At equilibrium, an internal electric field is then reached to balance the diffusion. For a-Si:H, the diffusion length of minority carriers in the doped layer is so small that a p-n junction can hardly collect the carriers generated. In order to enhance carrier collection, a thin I layer is inserted into the junction. This results in a device that has a $p^+/i/n^+$ structure. The carriers generated in the I layer have much larger diffusion length and therefore have a better chance of being collected.

There are two approaches to fabricate the a-Si:H $p^+/i/n^+$ solar cell, as shown in Figure 2.9. The first is to start with glass which is coated by transparent conductive oxide (TCO). Then $p^+/i/n^+$ layers are consecutively deposited with approximately thicknesses of 10, 500, and 40 nm, respectively. Finally, a back metal contact completes the device. This structure is usually called a superstrate solar cell. There are several problems with the superstrate solar cell. First, TCO will react with the hydrogen in the plasma at high temperature and leads to an opaque TCO [21]. One solution to the problem is to grow the p^+ at relatively low temperature to prevent the loss of oxygen and then immediately ramp the temperature up. Another problem is the diffusion of boron into the I layer at normal growth temperatures. The solution to this problem is to introduce an a-(Si,C):H layer grown at high temperature which prevents the diffusion. When the carbon content is properly graded, this a-(Si,C):H layer also

reduces the interface states.

The second approach for a-Si:H solar cell fabrication is to start with metal or TCO and follow this by the $n^+/i/p^+$ layers. This structure is usually referred as substrate (down) solar cell. By using this structure, some of the problems of the superstrate structure can be avoided. Some metals do not react with the species in the plasma, so high temperature processing is feasible. The growth of the p layer is the last step and the temperature is ramped down immediately after the p layer is finished. This results in less boron diffusion. The final TCO or semi-transparent metal contacts are usually finished at low temperature.

The physics of the a-Si:H $p^+/i/n^+$ solar cell is depicted in Figure 2.10, along with the equivalent circuit. For a good solar cell, it is required that the diode is of high quality. A good diode is characterized by the following; a) a small saturation current which results from small recombination of carriers; b) a large breakdown voltage which requires good material

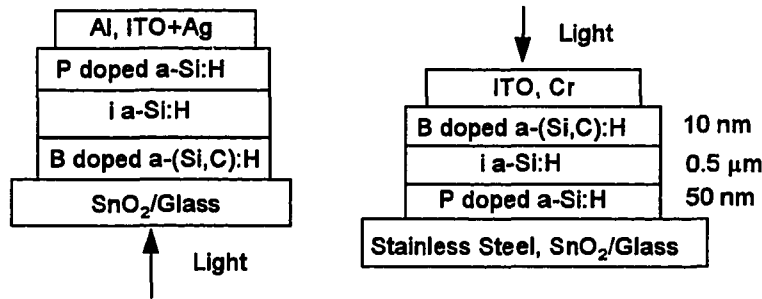


Figure 2.9. Superstrate and substrate a-Si:H $p^+/i/n^+$ solar cell. The typical layer thickness' are also included.

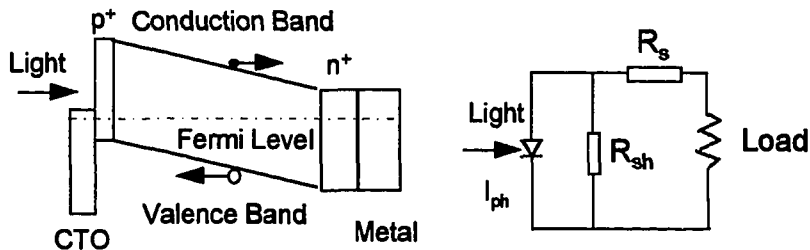


Figure 2.10. Band diagram and equivalent circuit of $p^+/i/n^+$ solar cell.

quality. From the equivalent circuit, the equation that can be used to characterize the solar cell is the diode rectifier behavior with the superposition of an photo-induced current, namely

$$j = j_s (e^{\frac{qV}{\alpha kT}} - 1) - j_{ph} = j_0 e^{\frac{-E_g}{\beta kT}} (e^{\frac{qV}{\alpha kT}} - 1) - j_{ph}, \quad (2.1)$$

where α and β are introduced to account for the non-ideal characteristic of the cell. The photo-generated current, also called short circuit current, depends on the spectrum of the light source, the material response to the light (mostly the absorption) and the collection efficiency of the structure. It can be expressed as

$$j_{ph} = q \int (1 - R) Q(E) \rho(E) dE, \quad (2.2)$$

where R is the reflection coefficient of the material, $\rho(E)$ the spectrum of the light source and $Q(E)$ the collection efficiency of the structure. When the current is set to zero, the voltage across the cell, called open circuit voltage, is given by

$$V_{oc} = \frac{\alpha kT}{q} \ln\left(\frac{j_{ph}}{j_s} + 1\right). \quad (2.3)$$

The I-V characteristics of an a-Si:H $p^+/i/n^+$ solar cell shows the characteristics of a rectifier. There is a point at which the output power reaches maximum. The ratio of the maximum power to the product of the open circuit voltage and short circuit current is called the fill factor

$$F.F. = \frac{I_m V_m}{I_{sc} V_{oc}}. \quad (2.4)$$

The total efficiency of the cell is then determined by the incident light power to the maximum electrical power that can be extracted from the solar cell

$$\eta = \frac{I_m V_m}{\phi_{in}}. \quad (2.5)$$

A good a-Si:H solar cell is characterized by a good fill factor ($\sim 70\%$), a good open circuit voltage (~ 0.85 V), and a good short circuit current (~ 20 mA/cm²). A high fill factor requires a low loss of photo-generated carriers in the I layer and at the interfaces, strong electric field in the I layer, and a good Ohmic contact. A high open circuit voltage requires efficient doping

in the p^+ and n^+ layers, which gives a higher built-in voltage, and good interfaces. A high short circuit current requires good material and good optical design to absorb and trap the light.

For illustration, the characteristics of a superstrate solar cell made by the PECVD system is demonstrated below. The process is listed Table 2.4. The p^+ layer was made by the mixture of diborane, methane, silane and hydrogen at low temperature which is necessary to prevent the reaction between the plasma and the tin-oxide substrate. The temperature was ramped up immediately to 350 °C. Meanwhile, a plasma cleaning process is introduced to reduce the cross contamination. An a-(Si,C):H thin buffer layer (II) is deposited to smoothly connect the p^+ layer and the I layer. The buffer layer also prevents the diffusion of boron into the I layer. The I layer is made by pure silane for about 30-40 minutes. Finally, the n^+ layer is deposited by mixing the phosphine, silane and hydrogen. The RF power used is about 20 W/250 cm² and the gas pressure is in the range of 15~25 mT.

The fresh made superstrate solar cell was then transferred to a high vacuum thermal evaporation chamber for metal contact. Usually, Al and Ag are used because of the high reflection and good Ohmic contact to a-Si:H. However, the post thermal treatment that is

Table 2.4. The process of a 8 % efficient superstrate a-Si:H solar cell by the triode PECVD.

p^+	II	I	n^+
B_2H_6 (*) 17 sccm			PH_3 (*) 18 sccm
CH_4 10 sccm	CH_4 8->0 sccm		
SiH_4 6 sccm	SiH_4 8 sccm	SiH_4 8 sccm	SiH_4 6 sccm
H_2 40 sccm	H_2 40 sccm		H_2 40 sccm
200 °C	350 °C	300 °C	300 °C
3.5 min	5 min	35 min	10 min
15 nm	20 nm	400 nm	40 nm

* 1 % B_2H_6 and PH_3 diluted in H_2

required to improve the adhesion and aggregation of the metal to a-Si:H creates problem for Ag which diffuses into a-Si:H network at elevated temperature. Hence, Al is normally used as the contact.

I-V characteristics were measured as shown in Figure 2.11. The cell has a conversion efficiency of about 8 %. This is reasonably good for a single chamber deposition, which does not include the introduction $\mu\text{-Si } n^+$ and p^+ layers or a high back reflector. In general, there are two regions of the I-V curve that show the qualities of the solar cell. One is the slope of the I-V curve around the open circuit voltage. It reflects the series resistance of the solar cell, and indicates the quality of the Ohmic contact. The other one is the slope of the I-V curve around the short circuit current which reflects the shunt resistance. Usually, this resistance indicates the quality of the a-Si:H I layer. For a high quality solar cell, small series resistance and large shunt resistance are needed. It is seen that the cell displays good qualities, with a 0.8 V open circuit voltage, 15 mA/cm² short circuit current and a fill factor of 67.5 %.

Although the I-V characteristics give general information about the solar cell, the details of the solar cell are determined by the quantum efficiency (QE), also known as spectral response. The QE is defined as the probability that an electron-hole pair created by a photon

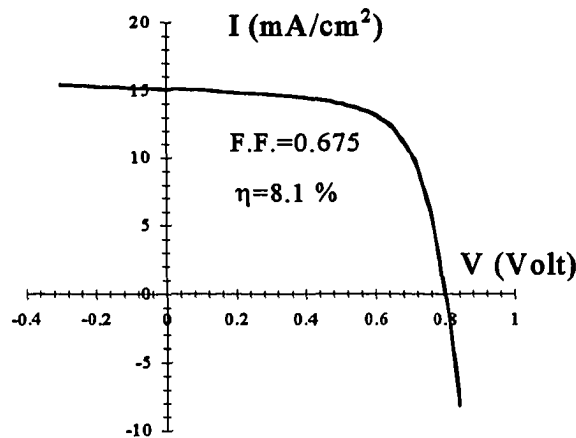


Figure 2.11 I-V characteristics for a 8 % efficient superstrate a-Si:H solar cell by the triode PECVD system.

is collected. To measure the QE, light from a lamp is guided through a monochromator to yield single wavelength light. The monochromatic light then passes through a chopper which is rotating at 13.33 Hz. By using optical lenses and mirrors, the single wavelength light beam is directed on to the device. The photo-current is then measured by a lock-in amplifier which detects only the current with the chopper frequency. A second DC white beam is also directed on to the device to fill up the midgap states so that the quasi Fermi levels of the carriers are split and the carriers collected are from the transition from the valence band to conduction band. A standard cell with a known efficiency as a function of wavelength is then used to obtain the QE.

QE measured at 0 bias determines several important characteristics of the cell. The QE value at short wavelengths (~ 400 nm) indicates the thickness of the p^+ layer. A p^+ layer which is too thick would lead to a very low QE and a too thin p^+ layer would result in a high QE. The general accepted QE value at short wavelength is about 0.6 for a 10 nm thick p^+ . QE values at long wavelengths (~ 700 nm) indicates the collection efficiency of the long wavelength light either by high reflection or the texture of the substrate. It is also related to the material quality of the entire cell. A good reflector, such as the combination of ZnO/Ag, with proper texture structure will yield a QE value above 0.2 at 700 nm for good quality material. Finally, the position of the maximum QE in the spectrum is usually associated with the thickness of the I layer. When the thickness of the cell is thin, the maximum QE position will shift to short wavelength. For a cell with a thickness of about 350 nm, the maximum QE occurs at about 540 nm.

QE measured under bias can give an indication of the electric field profile inside the cell [22]. When the solar cell is under a forward bias, the internal electric field is reduced. As a result, the carrier collection efficiency is reduced since the carrier collection of a-Si:H solar cells relies on the assistance of the electric field to enhance the carrier diffusion length. For a high quality solar cell, the internal electric field is so strong that an applied forward bias will not destroy the established electric field and the assistance of the internal electric field is still available. In addition, the quality of the I layer is so good that the diffusion of the carriers is

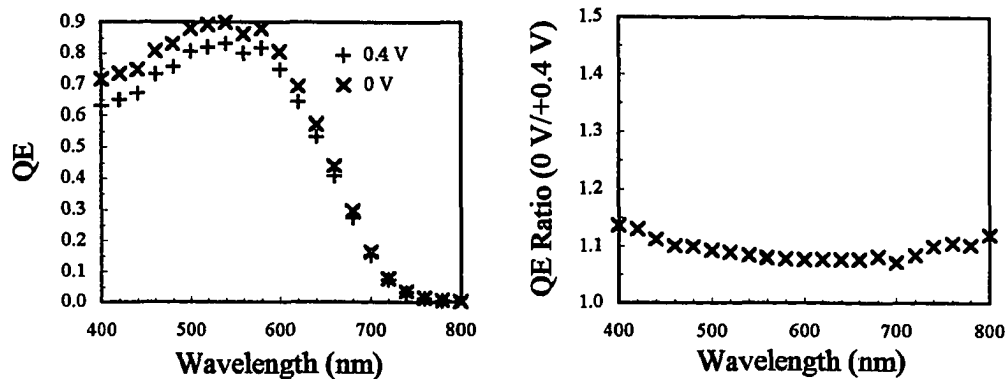


Figure 2.12. QE measurements of the 8 % efficient solar cell in the visible light.

still extended. Figure 2.12 shows the QE of the 8 % a-Si:H superstrate solar cell at 0 and +0.4 bias, and the ratio in the visible light wavelength. It is seen that the cell is properly designed by a small flat QE ratio over the visible light wavelength.

The stability of the cell was tested by accelerated light soaking under a 1 W/cm^2 ELH light. A fan is mounted to keep the surface temperature of the cell low. The I-V characteristics and QE were measured subsequently. Figure 2.13 shows the fill factor, open circuit voltage, short circuit current and conversion efficiency as a function of the light soaking time. It is seen that they decrease as the light soaking time increases which can be attributed to the deterioration of the material. Figure 2.14 shows the QE ratio (0 to +0.4 V) at different illumination time. A nearly uniform increase in the QE ratio is seen as the light soaking time increases, indicating a unique degradation mechanism which is most likely the degradation of the a-Si:H material. It was shown [23] that the degradation by short wavelength light involves the p^+/i interface since the light is absorbed in that region. The degradation by long wavelength light occurs through the entire cell and reduces the quality of the material. Therefore, a short wavelength rich light source affects the solar cell differently from a long wavelength rich light source.

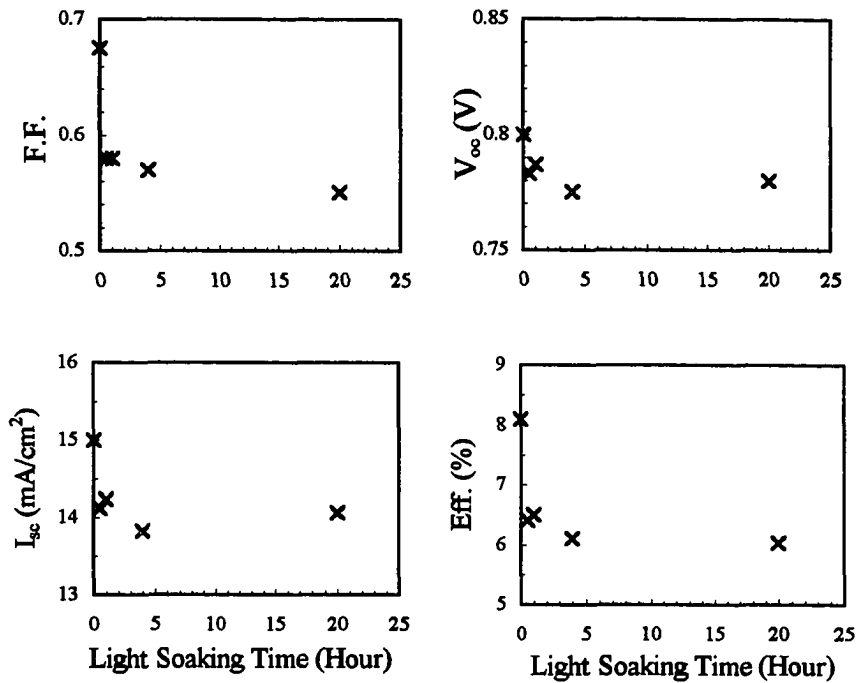


Figure 2.13. The degradation of the fill factor, open circuit voltage, short circuit current and conversion efficiency of the 8 % efficient superstrate a-Si:H solar cell under 1 W/cm² ELH light soaking.

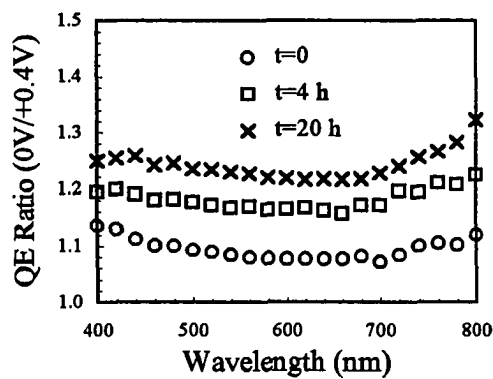


Figure 2.14. The degradation of QE ratio (0V/+0.4V) of the 8 % efficient superstrate a-Si:H solar cell under 1 W/cm² ELH light soaking.

3. SUBSTRATE a-Si:H SOLAR CELL

The advantages of substrate a-Si:H solar cells

Figure 3.1 is the schematic of a substrate a-Si:H solar cell and the corresponding band diagram. The structure allows high temperature deposition for the p^+ or $\mu\text{-Si } p^+$ layer. The reaction of SnO_2 with H_2 in the plasma is severe when the temperature exceeds 200°C , while a high quality a-Si:H material normally requires a deposition temperature of more than 250°C . The formation of μc material requires either high deposition temperature or heavy hydrogen dilution. This makes SnO_2 impossible to start with. It is also known that p^+ $\mu\text{-Si}$ can be deposited easier on a-Si:H than a SnO_2 substrate [24]. Therefore, the arrangement of superstrate solar cells is inappropriate for further improvement of the stability of highly efficient solar cells. Another advantage of the substrate cell is the possibility to reduce the defects that develop due to the large mismatch of the structure of the substrate and the a-Si:H network. Although the a-Si:H random network has in principle no preference to the substrate, the development of defects in the columnar form during the deposition exists [25] and deteriorates the performance of the solar cell, especially the stability. The substrate structural solar cell provides a solution to the problem by allowing a growth of a thick n^+ template layer to bury the defects that can become columnar. To date no experimental evidence has been demonstrated. The current study is intended to prove this idea. A third advantage of the substrate cell is that the boron diffusion problem in the superstrate solar cell can be avoided as the p^+ is the last layer in the substrate structure and the temperature is ramped down quickly.

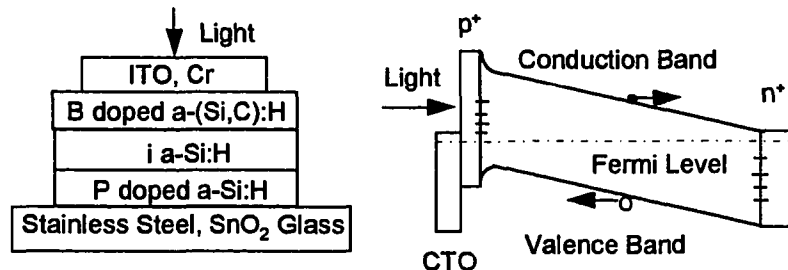


Figure 3.1. The structure and band diagram of a substrate a-Si:H solar cell.

The indium-tin-oxide (ITO) transparent conductive film

Indium-tin-oxide (ITO), a transparent conductive oxide (TCO), has a high energy band gap and shows very low absorption for visible light. It is a n-type material in amorphous form when fabricated at low temperatures. Similar to SnO_2 , ITO has also been found to be reactive with a hydrogen plasma [26] for temperatures exceeding 220°C . Good ITO demonstrates optical and electronic properties suitable for the application of solar cells. The transmission of an ITO film ($\sim 200\text{ nm}$) is above 80 % for visible light, and it has a conductivity of about 10^{-4} S/cm . The deposition of ITO has been successfully accomplished by CVD [27], thermal evaporation [28], DC and RF magnetron sputtering [29]. Each of these techniques results in comparative qualities. Since the ITO is deposited on the thin p^+ layer, low temperature deposition is required to avoid the possible damage to the a-Si:H network.

This research uses a DC/RF magnetron sputtering system which is depicted in Figure 3.2. The principle of the sputtering is as followings. The target material is bombarded by Ar ions created by either a DC or a RF field. The magnetic field provided by magnets bends the ions toward the target and knocks the target element out. As in glow-discharge, a DC bias is induced between the sample which is grounded and the target which is connected to the RF power. The deposition occurs when the element of the target reaches the surface of the sample and becomes condensed. The target used in this study is a mixture of 10 % $\text{SnO}(2)$ and 90 % $\text{In}(2)\text{O}(3)$ in atomic weight.

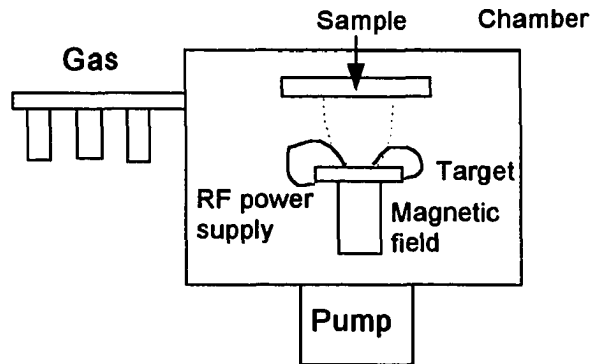


Figure 3.2. Schematic of the DC/RF magnetron sputtering system for the ITO.

Three different gases which contain different oxygen contents are used for this study, 1) pure argon gas, 2) Ar gas with 100 vppm O₂, and 3) Ar gas with 1 % O₂ by volume. These three different gases result in very different films since the oxygen content is very critical to the electronic and optical properties. Figure 3.3 shows the resistivity and average transmission of visible light (400-800 nm) for a 200 nm thick ITO films deposited on glass under different conditions. The conductivity was measured by four point probe and the transmission by a λ -9 spectrophotometer. Good resistivity ($\sim 10^{-4} \Omega\text{cm}$) and transmission ($\sim 80\%$) are obtained for low pressure and low RF power growth. In general, a low oxygen background benefits the quality of ITO film for the target used for this work.

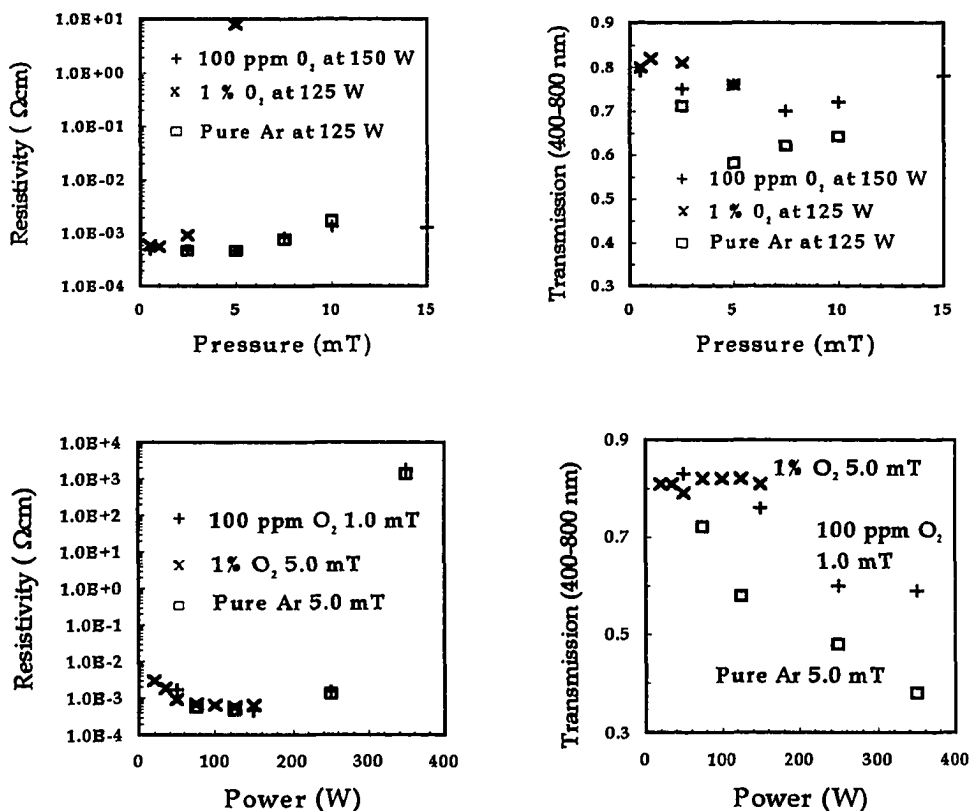


Figure 3.3. Effects of RF power, gas and gas pressure on the resistivity and average transmission in the visible light of ITO film.

The ITO was then used to make contact to an a-Si:H superstrate solar cell deposited in the PECVD system. Aluminum or silver was subsequently deposited to enhance the reflection and to reduce the series resistance. Figures 3.4 and 3.5 show the I-V characteristics and QE measurement for different contacts. It is found that ITO not only makes contact to the n^+ layer, but also blocks the diffusion of Ag into the a-Si:H during heat treatment. As mentioned earlier, ITO is a n-type material and it is not surprising to see that it makes good Ohmic contact with n-type a-Si:H. However, one notices that the fill factor for the cell with the ITO contact without the Ag reflector is much lower than the one with the Al contact. The explanation is that there is a contact resistance between the probe and the ITO film. The fill factor for the cell with ITO+Ag is still slightly lower than Al. The explanation for this is that the cell was exposed to air before the ITO contact was made in the present processing. One probably needs a high temperature deposition process to activate some surface reactions. From the QE measurement, an improvement is seen in the long wavelength collection, which also increases the short circuit current from 14 mA/cm² for Al contact to 19 mA/cm² for the ITO+Ag contact.

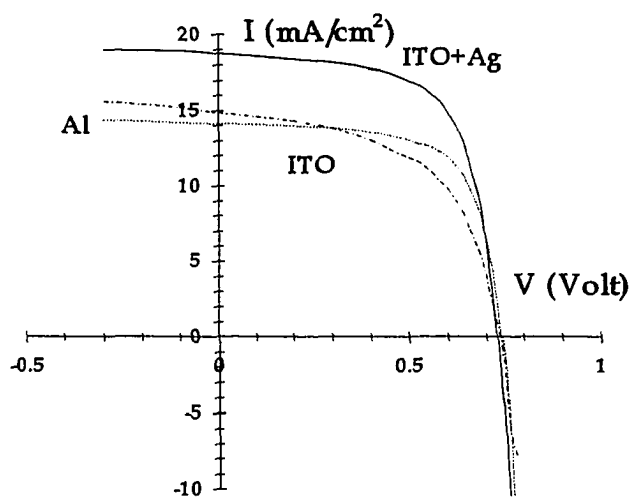


Figure 3.4. I-V characteristics for a superstrate a-Si:H solar cell with Al, ITO and ITO+Ag back contacts.

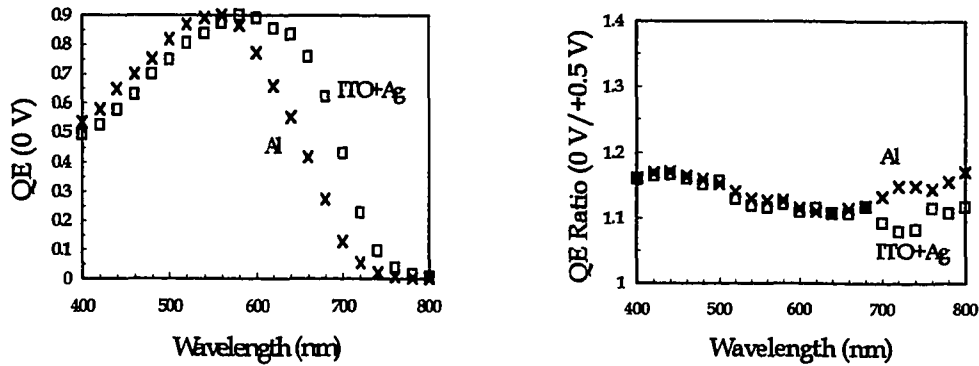


Figure 3.5. QE measurements for a superstrate a-Si:H solar cell with Al and ITO+Ag back contacts.

The substrate a-Si:H solar cell

Two different substrates, stainless steel foil and SnO₂ coated glass, were used in this research. The most important parameters of the substrate for a-Si:H solar cells are the work function relative to the a-Si:H material, the reflection in the visible light, and the resistance to the plasma. The mismatch of the work function will induce a barrier to the photo-generated carriers and the collection is hence degraded. The barrier can usually be made very thin by optimizing the growth conditions so that carriers can tunnel through. The reflection coefficient of the substrate is important because if it is low it will cause a loss of the long wavelength light which is not absorbed in the a-Si:H layer. The resistance of the substrate to the plasma is important as the reaction between the plasma and the substrate can change the material. It is known that metals like Al have work function matching to a-Si:H and their reflections are high. However, these metals are very active and tend to diffuse into a-Si:H network at normal deposition temperatures. Stainless steel is relatively stable at 350 °C in the hydrogen plasma, and has a fairly good reflection (~70 %). SnO₂, on the other hand, reacts with the hydrogen plasma above 200 °C. However, it usually has conductivity about 10⁴ S/cm and transmission of about 80 % for visible light.

Effects of front contacts

The front contact used in this work was either a thin semi-transparent metal or ITO. The semi-transparent metal contact is 10 nm thick Cr which results in about 20 % transmission for visible light. Since ITO is an n-type material, it does not always form a good Ohmic contact to the p-type a-(Si,C):H. Figure 3.6a shows the I-V characteristics and QE measurements for a substrate solar cell made by the triode PECVD system on stainless steel substrate. The processing conditions are listed in Table 3.1. The device shows a good open circuit voltage, 0.83 V, and reasonably good short circuit current (8 mA/cm^2) for a 200 nm ITO contact without light trapping or a back reflector. The fill factor is 38 % for ITO contact and 59 % for Cr contact, well below the standard value of 70 %. From the QE measurements, one sees that the carriers generated by long wavelength light are not effectively collected. This could be due to the following reasons; 1) the reflection of light at the stainless steel surface is reduced, 2) the single chamber deposition of the whole device causes cross contamination of the residual phosphor into the I layer, especially near the region close to n^+ layer. A low reflection causes a loss of long wavelength light which is not absorbed in the I layer and the QE at long wavelength is low. The contamination in the I layer increases the recombination centers for holes. Those holes generated by long wavelength light near the n^+ side are more likely to be killed rather than coming back to p^+ side. Since a-Si:H solar cell is a device which depends on the collection of holes, any loss of holes will deteriorate the performance. One also notices that the ITO contact gives a higher open circuit voltage than Cr, indicating the existence of a barrier between the ITO and the p^+ layer. This barrier can trap hole and therefore increase the open circuit voltage.

The ITO contact on the cell can be improved by varying the sputtering condition and grading the carbon content in the p^+ layer to yield a better contact. One scheme is to reduce the content of the carbon at the surface so that the conductivity of that region is very high and an effective Ohmic contact is possible for the ITO layer. Figure 3.6b shows the contact of an ITO film to a cell when the p^+ layer is properly graded. It was found that low pressure (2.5 mT) and RF power (50 W) sputtered ITO produces better Ohmic contact.

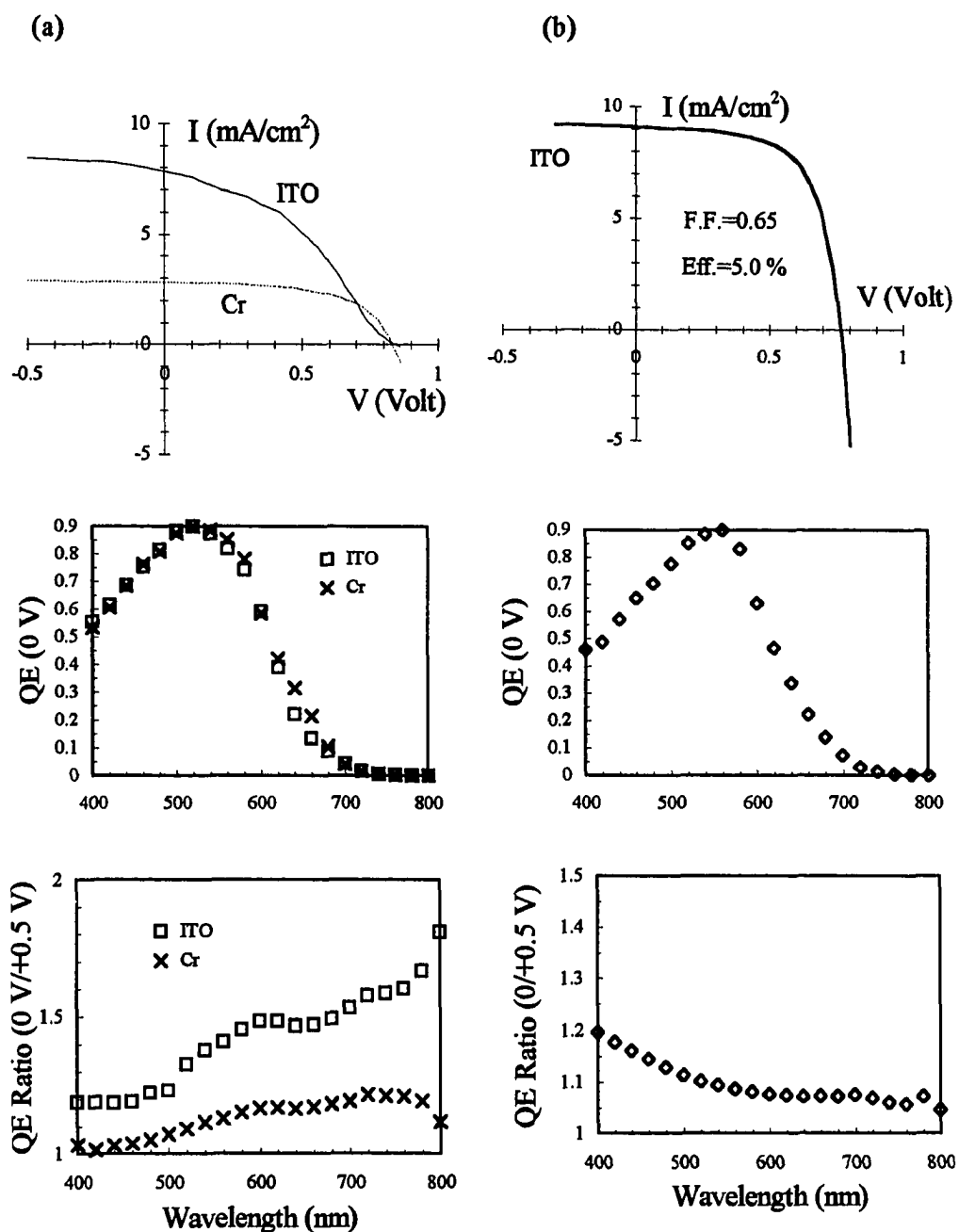


Figure 3.6. a) Comparison of ITO and Cr contacts to substrate a-Si:H solar cells; b) Good ITO contact grown by low pressure (2.5 mT) and RF power (50 W), and with correctly graded surface carbon content in p⁺ layer.

Table 3.1. Process parameters of a typical substrate a-Si:H solar cell by the triode PECVD. The dopant for p⁺ is TMB (B(CH₃)₃).

n ⁺	I	II	p ⁺
PH ₃ 18 sccm			TMB (*) 5 sccm
		CH ₄ 0->6 sccm	CH ₄ 10 sccm
SiH ₄ 6 sccm	SiH ₄ 8 sccm	SiH ₄ 6 sccm	SiH ₄ 6 sccm
H ₂ 40 sccm		H ₂ 40 sccm	H ₂ 40 sccm
250 °C	260 °C	260 °C	260 °C
10 min	30 min	2 min	4 min
30 nm	300 nm	10 nm	15 nm

Effects of p⁺/i interface smoothing

The band structure of boron doped a-(Si,C):H is very different from simple a-Si:H, especially the valence band. When boron doped a-(Si,C):H is brought into contact with an a-Si:H layer, there is a mismatch of the band structure. This mismatch will cause a decrease in the collection of holes. The problem can be solved by introducing a grading layer between the p⁺ and I layer, often called a buffer layer. The grading is achieved by changing the CH₄ flow during the deposition. Two sets of devices were made with different substrates and dopant gases. Among the sets, one has no buffer layer and the other has a buffer layer of about 10 nm. Figures 3.7 and 3.8 show the I-V characteristics and QE measurements for the devices. The contact is 10 nm Cr. From the data, it is clear that the open circuit voltage is increased by 0.05 V in most cases. As previously mentioned, the open circuit voltage depends on the built-in voltage and the quality of the interfaces. The built-in voltage depends mostly on the doping levels, or the activation energies, of the n⁺ and p⁺ layers. The interface, especially p⁺/i interface, depends on the growth conditions and the design. A smooth matching of the band structure throughout the entire device will generally result in a better performance. However, a mismatch at the interface will cause a drop in the open circuit voltage and a reduction of the electric field in the device. It is also seen that interface smoothing not only enhances the open

circuit voltage but also the fill factor, indicating that a strong electric field is created inside the cell by the interface smoothing. When one measures QE ratio, one finds a tremendous enhancement in the hole collection at long wavelength for cells with a buffer layer. For devices that were optimized both with and without the buffer layer (1/1375, 1/928), the increase of the open circuit voltage is the result of the reduction of interface states and the increase of short circuit current is due to the increase of the electric field in the cell.

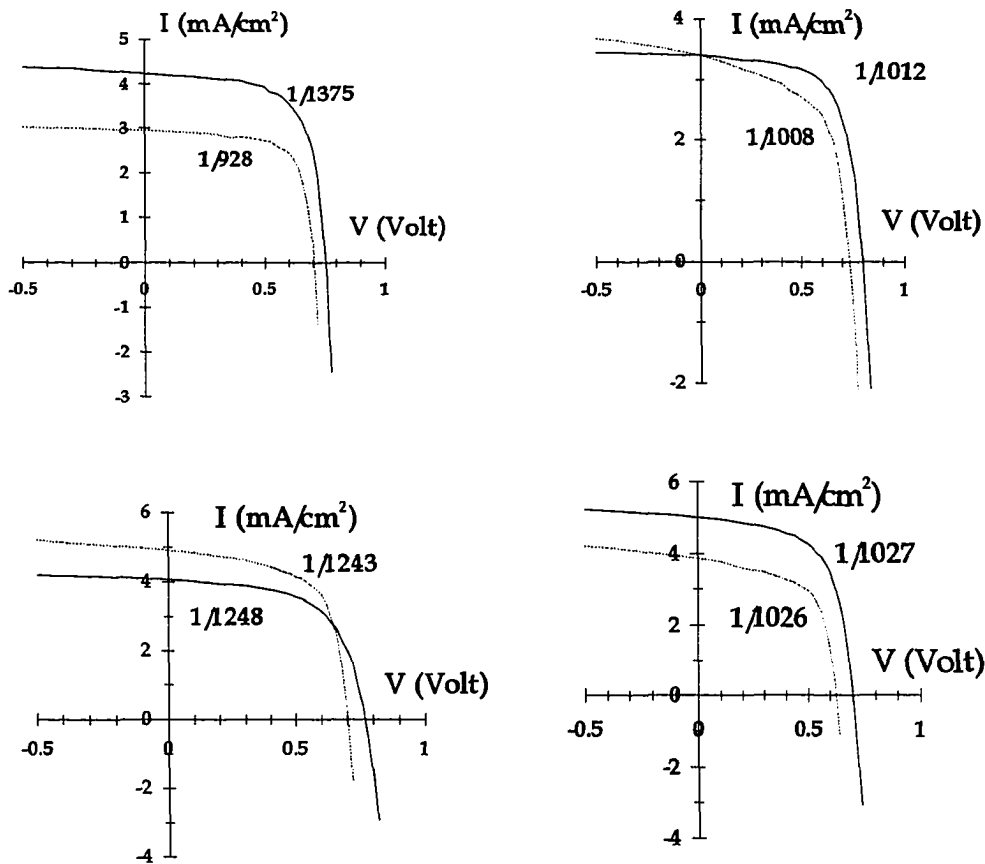


Figure 3.7. I-V characteristics of the sets of substrate a-Si:H solar cells with and without the buffer layer. The substrate is stainless steel for the top devices and SnO₂ for the bottom devices. Devices at the right are doped with B₂H₆, devices at the left are doped with TMB.

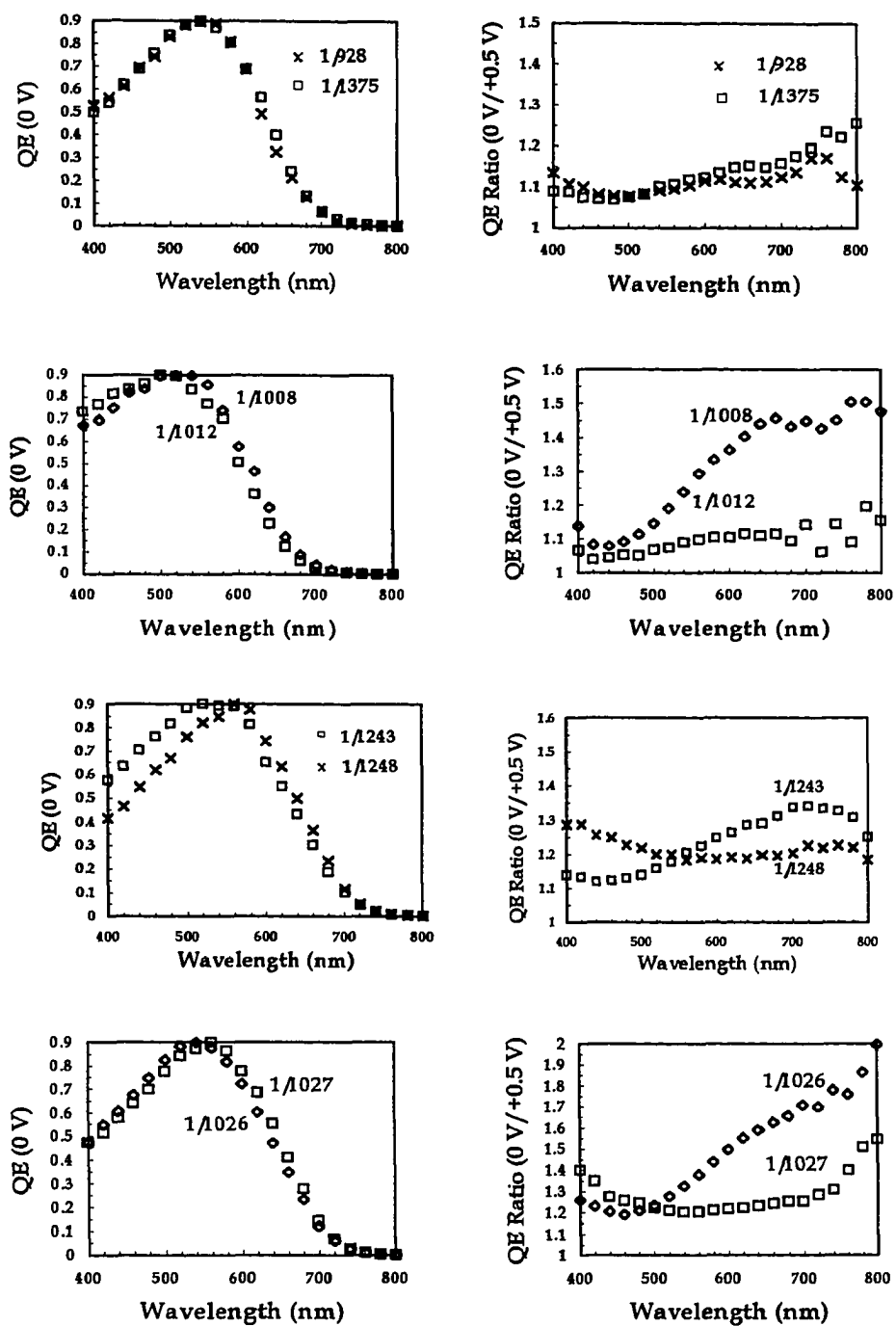


Figure 3.8. QE measurements of the sets of substrate a-Si:H solar cells with and without buffer layer.

To further appreciate the importance of the buffer layer, the stability of one set devices (1/1012 and 1/1008) was tested under 200 mW/cm^2 Xenon light through the Cr contact. The 10 nm Cr contact allows only 20 % of the light to be transmitted, therefore the absolute degradation was not tested. However, if a set of devices is degraded under same condition, the relative stability can still be compared. Figure 3.9 shows the degradation of the fill factor, open circuit voltage, short circuit current and conversion efficiency as a function of light soaking time. It is seen that the device with the buffer layer is far superior to the device that does not have the buffer layer, in almost every respect.

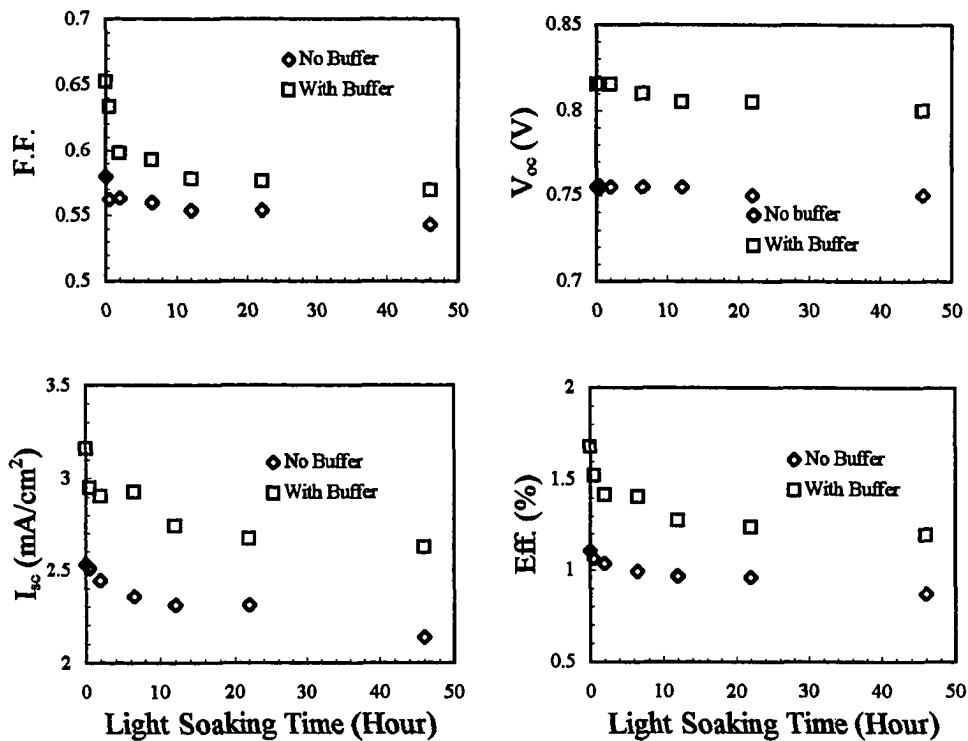


Figure 3.9. Degradation of the fill factor, open circuit voltage, short circuit current and conversion efficiency of a set of devices with and without the buffer layer under 200 mW/cm^2 Xenon light soaking.

The effects of I layer thickness

The thickness of the I layer is critical to the performance of a-Si:H solar cells. As indicated previously, the collection of the photo-generated carriers, especially short lived holes, depends on the electric field inside the cell. The electric field inside the cell depends on first doping concentration in the p^+ and n^+ layers and the structure of the cell, including the smoothing of the p^+/i interface. The thicker the I layer, the smaller the electric field inside the cell, especially in the middle of the cell where the transport of the photo-generated carriers is very important to the performance of the cell. Although thick I layers help the light collection and therefore give higher short circuit currents, the reduction of the internal electric field strength limits the collection of the carriers and leads to a poor fill factor. To illustrate this, several cells with different I layer thicknesses were made. Table 3.2 lists a set of devices and the initial performance of these devices. It is seen that the device with a thin I layer has a high fill factor, but small short circuit current. The open circuit voltages of both devices are comparable.

Table 3.2. Performance of two devices with different I layer thickness. The contact is 10 nm Cr. The dopant gas is TMB.

I layer thickness (nm)	F.F.	V_{oc} (V)	I_{sc} (mA/cm ²)
300 (1/1012)	0.68	0.80	3.2
500 (1/1013)	0.58	0.815	3.6

The reason that a thick I layer device gives poor F.F. can be understood by the fact that an a-Si:H solar cell is a field-assisted device. When the field is small, the holes generated near the n^+/i interface cannot make the trip to the p-layer since the $\mu\tau$ product of the hole in the a-Si:H only allows it to travel about 0.3 μm for high quality material. When the film is contaminated by donors like oxygen and nitrogen, the distance a hole can travel is even less. Therefore, an electric field is needed for efficient hole collection at the backside of the cell. It is easier to build a high electric field for a thin solar cell than a thick one when the n- and

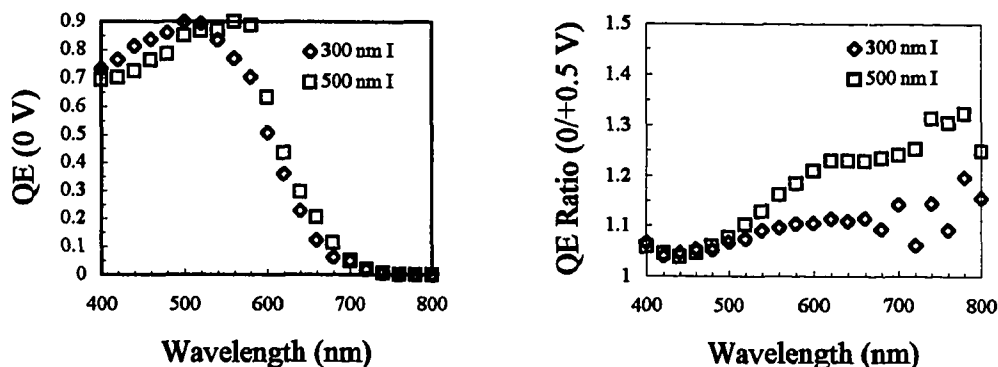


Figure 3.10. QE measurements of devices with different I layer thickness'. The dopant gas is TMB.

p-layers are kept the same. Hence, the hole collection is usually more efficient in a cell with a thin I layer than the corresponding cell with a thick I layer. Figure 3.10 shows the QE measurements of the cells. It is clearly seen that the cell with a thick I layer has a hole collection problem for long wavelength light which penetrate deeper into the cell.

The stability of the cells with different I layer thicknesses was tested under 200 mW/cm^2 Xenon light through Cr contacts. Figure 3.11 shows the fill factor, open circuit voltage, short circuit current and conversion efficiency as a function of the light soaking time. It is seen that the fill factor of the cell with thin I layer saturates at a higher value than the corresponding thick one. The opposite is true for the short circuit current. The open circuit voltages and the conversion efficiency, on the other hand, saturate at about same level. Therefore, thin cell design is of advantages for the improving stability because the short circuit current can always be enhanced by reflecting the light back and absorbed it on the second or even third path. In addition, if the cell is a tandem cell, the unabsorbed light will be collected by the second cell which has the right energy band gap. Hence, the stability of the fill factor becomes the most important factor. As described previously, a good device usually has a fill factor of about 70 %. If a 10 % degradation is allowed, a saturated fill factor of about 63 % would be expected. It is very difficult to achieve such a high saturated fill factor.

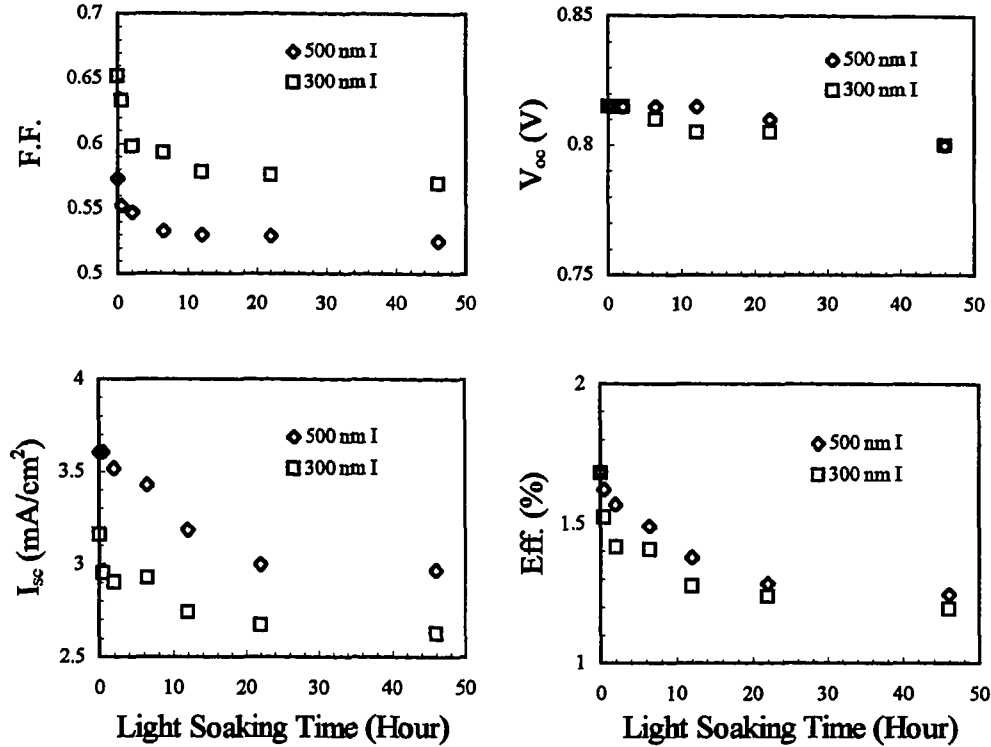


Figure 3.11. The degradation of the fill factor, open circuit voltage, short circuit current and conversion efficiency under 200 mW/cm² Xenon light soaking for devices with different I layer thickness'. The dopant gas is TMB.

Similar devices were made by using diborane as the dopant gas. Table 3.3 shows the initial performance of the devices. High fill factor is seen again for the thin cell and high current for the thick cell. The open circuit voltages for both devices are again comparable. The difference in the short circuit current is now much less than the previous case. This is due to the fact that a 0.4 μm thick I layer usually can absorb most of the light, and a further increase of the I layer does not help the light collection dramatically. Figure 3.12 shows the QE measurements for these devices. These measurements indicating once again that the hole collection problem for long wavelength light. However, the thick device shows more a severe long wavelength hole collection problem which explains the fact that the thick device has a lower fill factor.

Table 3.3. Performance of devices with different I layer thickness'. The contact is a 10 nm Cr. The dopant gas is B_2H_6 .

I layer thickness (nm)	F.F.	V_{oc} (V)	I_{sc} (mA/cm ²)
400 (1/1375)	0.67	0.795	3.3
600 (1/1376)	0.61	0.775	3.4

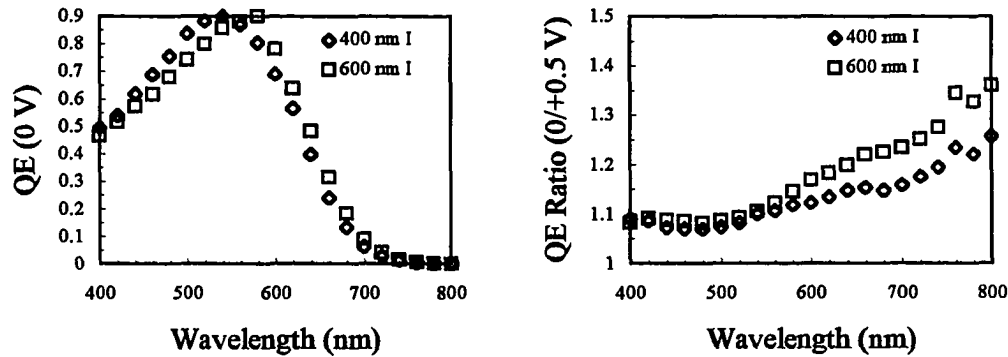


Figure 3.12. QE measurement of two cells with different I layer thickness' made by B_2H_6 dopant.

The stability of the cells was also tested under 200 mW/cm² Xenon light through the Cr contact. Figure 3.13 shows the fill factor, open circuit voltage, short circuit current and conversion efficiency of these cells as a function of the light soaking time. One sees again a higher fill factor for the thin cell and a higher current for thick cell. One also sees the difference in the conversion efficiencies is close to the difference of the open circuit voltages for this particular set of devices. One should not be misled by the small relative changes of the fill factor and open circuit voltage of the device with the thick I layer. As a whole device, the initial performance is not excellent due to the poor hole collection at long wavelengths by the small contamination from P. The defect states induced by the initial light exposure would only add to this background level. When more and more defect states are created by prolonged light exposure, the fill factor does not show a severe reduction and the same is true for the open circuit voltage.

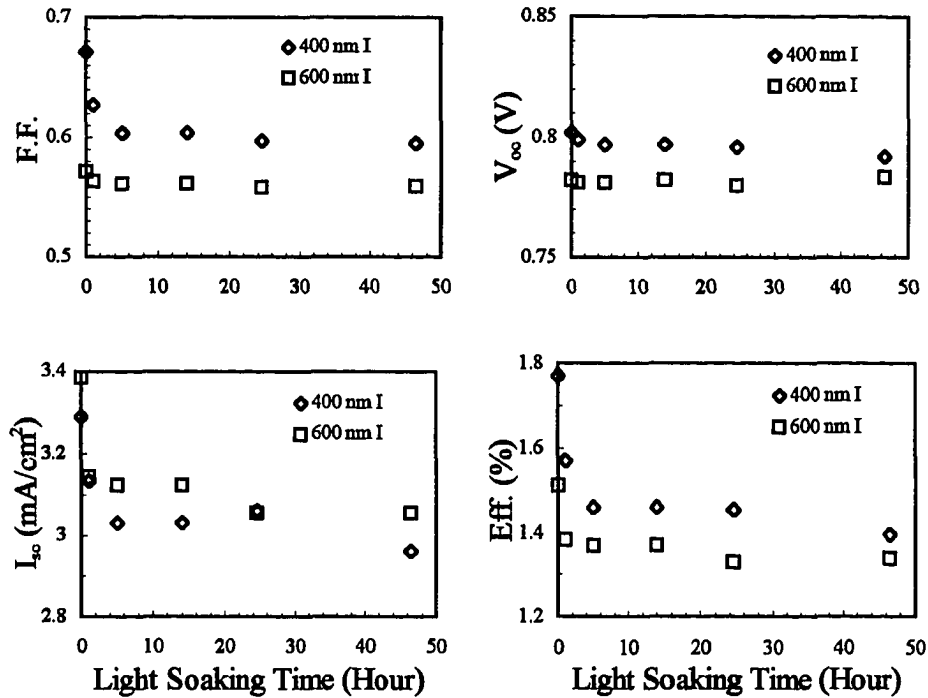


Figure 3.13. The degradation of the fill factor, open circuit voltage, short circuit current and conversion efficiency under 200 mW/cm^2 Xenon light soaking for devices with different I layer thickness'. The dopant gas is B_2H_6 .

Effects of ppm boron compensation in the I layer

As mentioned earlier, the process applied in this study was done in a single reactor chamber. The reactor is not ideal. There is always small leakage of air into the reactor during the operation. Cross contamination in the chamber also exists and could be very severe if care is not taken. Although gas purging and plasma cleaning are routinely used to minimize the contamination, it can never be eliminated completely. The leakage of air into the system results in the presence of O_2 which is an n-type dopant. In the superstrate solar cell, it is an advantage that the p^+ layer is deposited first. The chamber is coated with boron doped film, and the boron can be brought out during the growth of the I layer to compensate for the oxygen donors. For the substrate solar cell, the first layer deposited is the n^+ layer, and the

compensation in the superstrate solar cell does not exist. Therefore, boron has to be introduced during the growth of substrate cells. For this purpose, B_2H_6 diluted in H_2 to 10 vppm is used. Four devices were made with different 10 vppm B_2H_6 flow rates during the deposition of the I layer. Figure 3.14 shows the fill factor and open circuit voltage of these devices. It is clearly seen that the low concentration boron compensation indeed improves the device significantly. The fill factor as well as the open circuit voltage increases as a result of boron doping. The QE measurement, shown in Figure 3.15, also indicates that the long

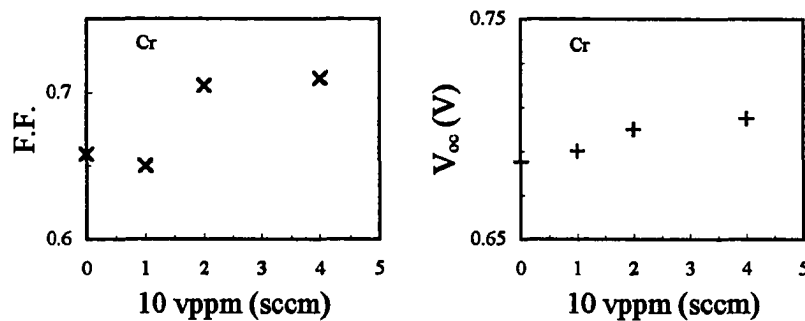


Figure 3.14. Fill factor and open circuit voltage of cells with different ppm boron compensation in the I layer during the growth.

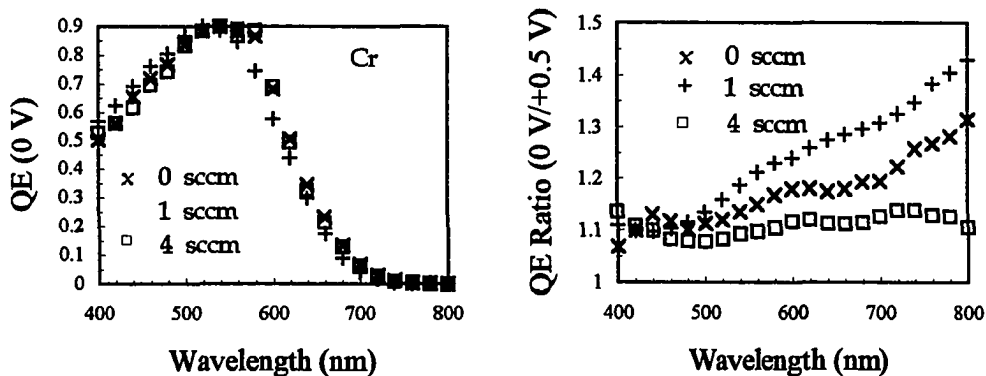


Figure 3.15. QE measurements of devices with different low concentration boron compensation in the I layer.

wavelength hole collection is improved significantly as the diborane flow rate increases.

The cells were then placed under 1 W/cm^2 ELH light for degradation. Figure 3.16 shows the degradation of the fill factor, open circuit voltage, short circuit current and conversion efficiency of two cells with different low concentration boron compensation in the I layer. It is seen that the fill factors of both devices reach about same level after 10 hour light soaking. However, the open circuit voltage shows opposite behavior with the device of high boron compensation in the I layer showing an increase.

When one measures the QE as shown in Figure 3.17, one finds an increase of QE at short wavelength for the cell with high boron compensation, indicating a different degradation process for the compensated a-Si:H. It is likely that the incorporation of the low

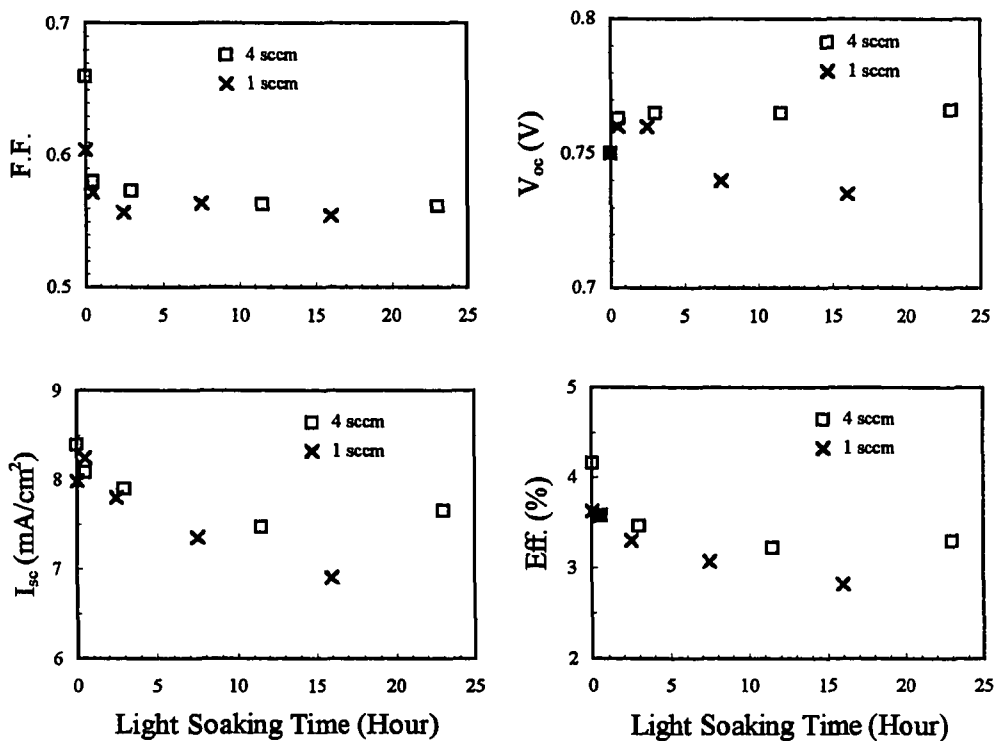


Figure 3.16. The degradation of the fill factor, open circuit voltage, short circuit current and conversion efficiency under 1 W/cm^2 ELH light soaking time for devices with different low concentration boron compensation in the I layer.

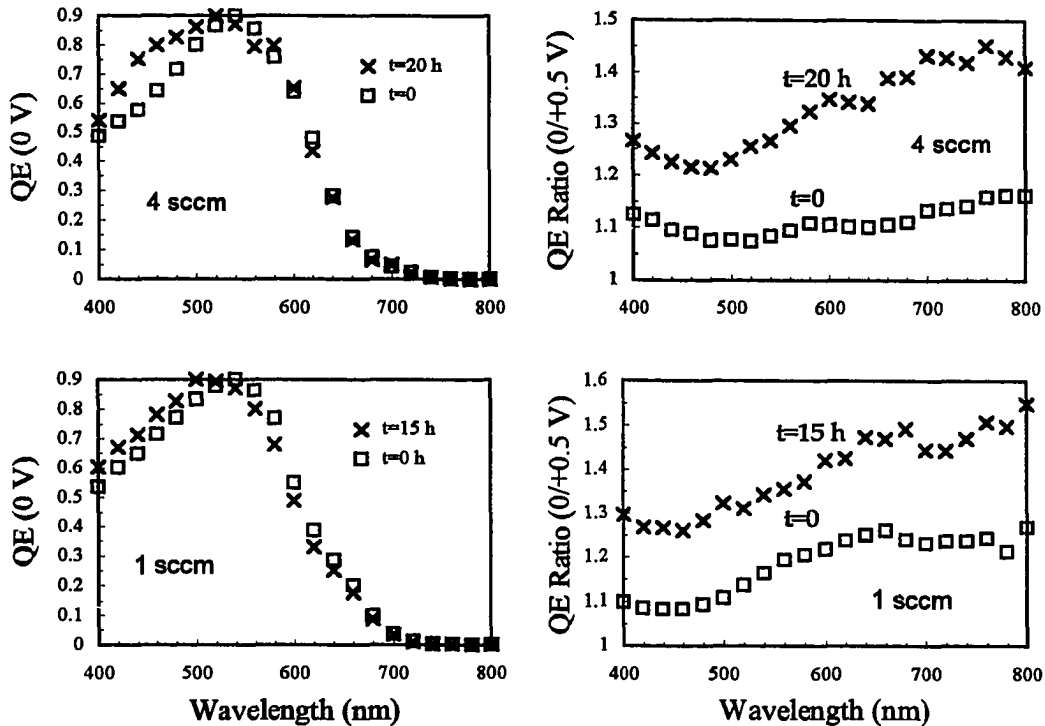


Figure 3.17. The QE measurements of two substrate a-Si:H solar cell with different low concentration boron compensation in the I layer at different light soaking time. The light intensity is 1 W/cm^2 ELH light.

concentration of boron changes the band structure near the p^+/i interface. It slightly moves the Fermi level, which favors the smoothing of the band structure in the presence of increasing defect states.

Effects of temperature grading

If an additional electric field is introduced in the I layer, the collection of the photo-generated carriers, especially the holes, will be enhanced. The time that the hole spends in going through the entire device is less and therefore the probability that it will recombine is reduced. To implement an electric field, one needs to engineer the band structure of the I layer. The energy band gap of a-Si:H is a function of the hydrogen content which depends on the growth temperature. The change of temperature during the deposition could lead to an

additional electric field inside the cell. To show the effect of the growth temperature on the cell, two devices were made at 260 °C and 340 °C with otherwise similar conditions. Table 3.4 compares the initial performance of these devices. It is seen that the open circuit voltage is larger for the lower growth temperature. This is a result of the increased energy band gap of the material as more H is incorporated into the film at low temperature. On the other hand, the short circuit current displays an increase upon the increase of the growth temperature, which is consistent with the fact that the film grown at high temperature has low energy band gap and allows the absorption of more light. Figure 3.18 also shows the QE measurements for these devices. One notices a slight change in QE (0V) at short and long wavelengths. This is attributed to the fact that the growth rate varies for different growth temperature. One also notices a dramatic change in the QE ratio for these two devices. This could be due to fact that the applied voltage (+0.5 V) is relatively large (close to the open circuit voltage) for

Table 3.4. Devices made at growth temperature of 260 °C and 340 °C by the triode PECVD. The contact is 10 nm Cr.

Temperature	F.F.	V_{oc} (V)	I_{sc} (mA/cm ²)
260 °C (1/1363)	0.622	0.79	3.2
340 °C (1/1364)	0.616	0.66	3.4

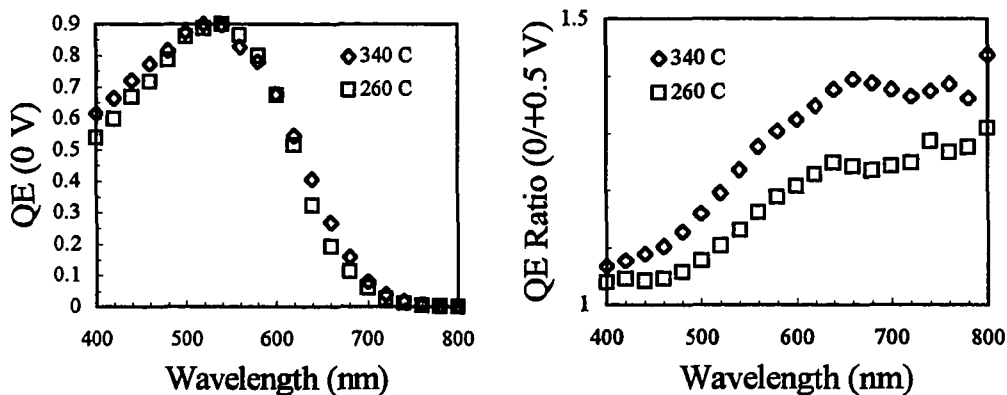


Figure 3.18. QE measurements of the devices made at low and high temperatures.

for the cell grown at high temperature. It is also possible that the matching of the p^+/i interface is actually a little bit better for the device made at low temperature than that grown at high temperature. This is due to the fact that the incorporation of the carbon, as well as the boron, into the a-Si:H network is temperature sensitive.

For a cell with a thickness of 0.5 μm , if the band gap is graded by 0.2 eV throughout the cell, one would get an additional 4×10^3 V/cm electric field, which is very appreciable in comparison with the electric field in a normal cell, which is on the order of 2×10^4 V/cm [30]. However, the electric field profile in the cell is highly non-uniform and the weakest electric field usually occurs in the middle of the cell. The collection of holes from the middle of the cell is extremely important since the solar spectrum is centered at a wavelength that penetrates deep into a 0.5 μm cell. Ideally, the grading should be as follows: at the vicinity of the n^+ layer, the band gap should be small (less H content) to enhance the absorption of long wavelength light, and then smoothly increase to high band gap (more H content), leading to a change of the valence band and an electric field. Therefore, both the field and absorption are simultaneously taken care of. However, the quality of the buffer layer, the I layer, and the non-ideal factors of the system alter this situation.

Several devices were fabricated with the only change being the deposition temperature. This was done to determine the best temperature grading. Table 3.5 lists the scheme of the grading and the corresponding initial cell performance. The total temperature grading is about 70 degrees (250-320 $^{\circ}\text{C}$) which gives about 0.1 eV difference in the band gap [31]. Since the thickness of the cell is about 0.4 μm , one would expect an electric field about 2.5×10^3 V/cm in the cell. It is noticed that the temperature grading scheme of device 1/1375 gives the best results. Figure 3.19 compares the QE measurement for these devices. It is interesting to see that the zero biased QE's are almost identical. However, the QE ratio (0/+0.5 V) increases steadily at the long wavelength for these devices, indicating different hole collection at the back of the devices. It is also noticed that the QE ratios of these device are very similar to each other for short wavelength, indicating similar band grading for the p^+/i interfaces.

Table 3.5. Devices made by three different temperature grading in the I layer by the triode PECVD. The contact is 10 nm Cr.

Temperature Grading	F.F.	V_{oc} (V)	I_{sc} (mA/cm ²)
260(n ⁺)→263→300(p ⁺) °C (1/1373)	0.549	0.775	3.1
280(n ⁺)→300→250(p ⁺) °C (1/1374)	0.57	0.815	3.6
270(n ⁺)→325→253→290(p ⁺) °C (1/1375)	0.67	0.795	4.8

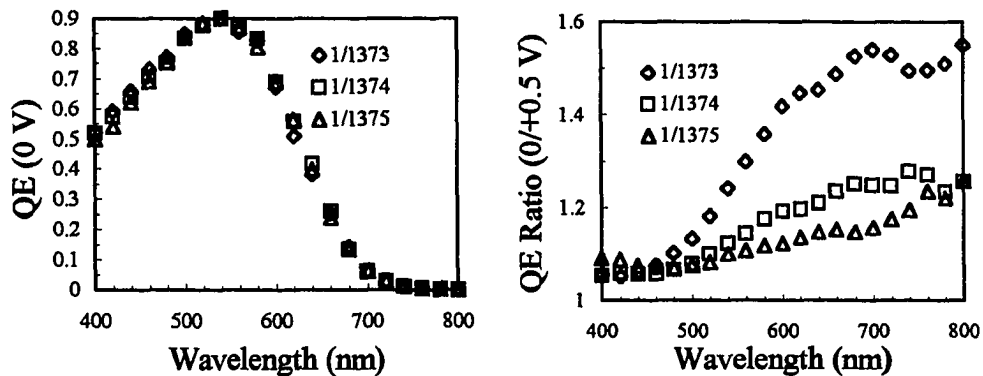


Figure 3.19. QE measurement for devices made at different temperature grading scheme.

To understand what happens to these devices, one needs to look at the band diagrams of the I-layer region, shown in Figure 3.20. It is seen that the device with the highest fill factor has the largest electric field available in the middle and at the back of the cell, while the device with the next highest fill factor has less electric field in the middle. This is due to the range of the temperature grading in this device being only about half of that for the device with the highest fill factor. The grading scheme for the device with the poorest fill factor actually reduces the electric field that is needed for the transport of the holes. It would be very interesting to perform some numerical simulations to see quantitatively the electric field profile for these temperature grading schemes. This work is beyond the scope of the current project.

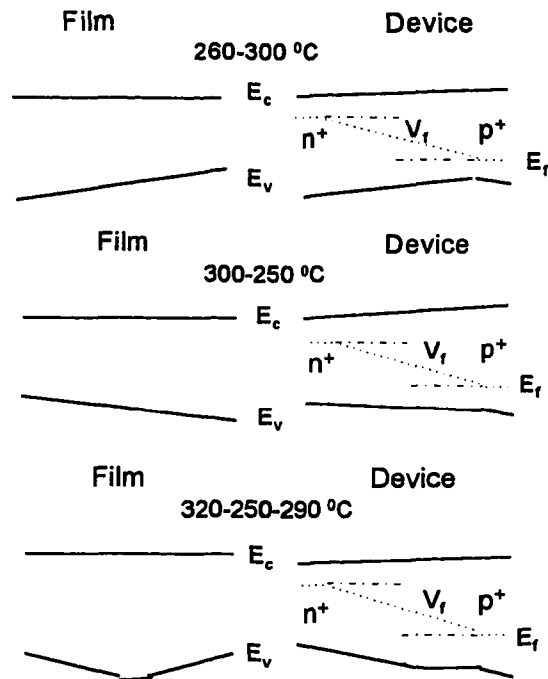


Figure 3.20. The band diagram for film and forward biased device by three different temperature grading.

To further appreciate the effect of temperature grading on the solar cell performance, the devices were degraded under the 200 mW/cm^2 Xenon light through the Cr contact. Figure 3.21 shows the fill factor, open circuit voltage, short circuit current and conversion efficiency of the cells as a function of the light soaking time. It is seen that the fill factor of the device with the right temperature grading saturates at about 60 %, and the overall conversion efficiency degraded only by 21 %. It is known that the best superstrate single junction a-Si:H solar cell has an initial efficiency about 10-12 % and will saturate at 8 % of below after prolonged light exposure. This is about 20-30 % drop in the efficiency. Therefore, the cell of our design has small degradation, largely because of the improved p^+/i interface and the existence of the electric field inside the cell. The comparison above is valid because the fill factor and the open circuit voltage are comparable to a good superstrate cell. The only difference is the low short circuit current due to the use of semi-transparent metal

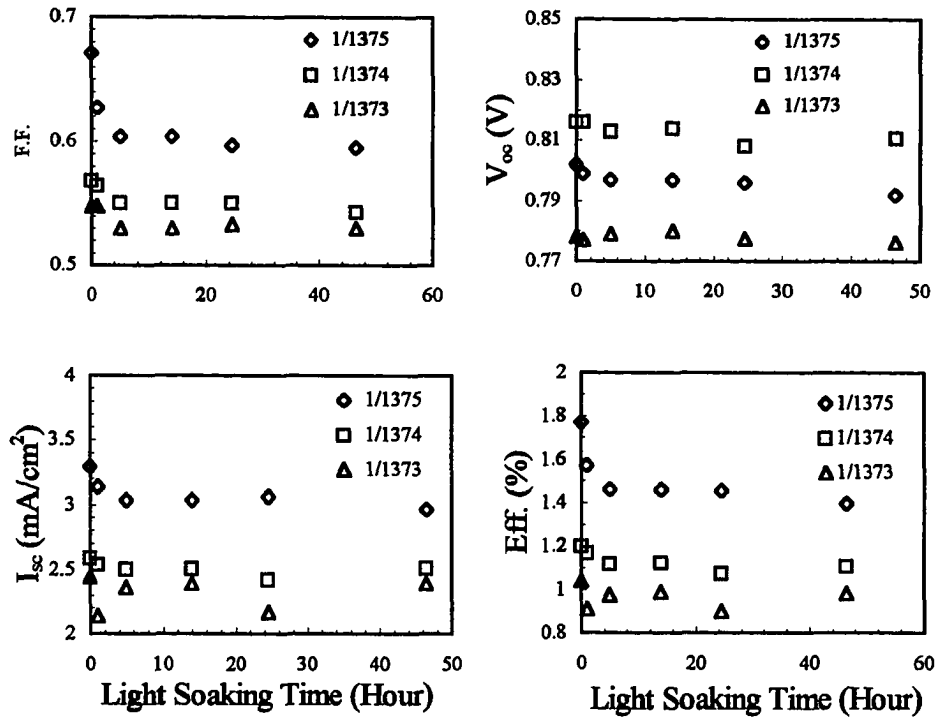


Figure 3.21. The degradation of the fill factor, open circuit voltage, short circuit current and conversion efficiency under 200 mW/cm^2 Xenon light soaking for devices with different growth temperature profiles.

contact, leading to a low conversion efficiency.

The effects of the n^+ layer

In the substrate structural solar cell, the first layer of the device is an n^+ layer. Unlike the superstrate solar cell where the thickness of the p^+ layer must be as thin as possible to avoid the loss of the light, the thickness of the n^+ layer has no limit if the light comes through the p^+ layer. The n^+ layer has several effects on the performance of the device. The most important effect is that as the thickness of the layer increases, the active part of the device is on the top of a template layer which can give a good a-Si:H network as shown in Figure 3.22. The defects that can develop in the columnar form are buried in the thick n^+ layer. This is

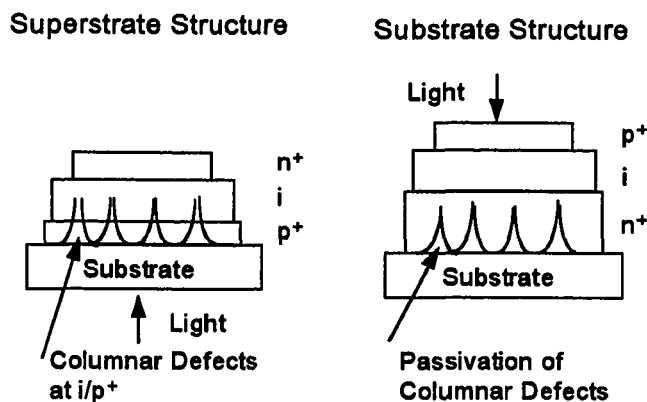


Figure 3.22. The comparison of superstrate and substrate solar cell under the influence of the columnar defect developed near the substrate.

significant when the stability of the device comes into picture as the degradation of the device is largely due to the bulk material and the p^+/i interface. In the superstrate structural cell, the p^+ layer is so thin that the p^+/i interface is still buried in a region where the columnar defects are not passivated. Therefore, the device is degraded a lot under prolonged light exposure, especially under short wavelength rich spectrum. For example, the fill factor of the 8.1 % cell decreases to about 78.6 % of its original value under the degradation of 300 mW/cm^2 Xenon light soaking, which is short wavelength light rich source. From the QE measurements, it was also seen that the cell is degraded much more severely near the p^+/i interface. For the substrate structural solar cell, on the other hand, a good quality p^+/i interface can be made at high temperature and on a thick template layer.

Different n^+ layers were grown on the stainless steel substrate for various times prior to the growth of the I and p layers. After the n^+ layers were made, the system was cleaned and recalibrated. The devices were then made by reloading the substrate with n^+ layer into the chamber. By doing this, the cross contamination problem by phosphorus was eliminated. The growth conditions were controlled very carefully to yield same devices except for the thickness of the n^+ layer. The identity of the devices were checked by growing an additional device which repeats the initial one. This is very important as the change of the growth condition can result in different cell and consequently lead to different degradation behavior

which comes from factors other than the quality of the material. One would also argue that the exposure of the substrate to the air could affect the performance of the device. This can be prevented if the device is regrown at reasonably high temperature, at which the oxide layer could be diffused through or the H in the plasma would etch the surface oxide away.

Furthermore, the performance of the cell largely depends on the hole collection, and the electron collection efficiency is always an order of magnitude higher. Therefore, the n^+/i interface is not as crucial as the p^+/i interface. The thickness of the n^+ layer was varied by changing the deposition time from 20 to 240 minutes, corresponding to a thickness about 0.1 and 1 μm . This was confirmed by the optical measurement of an n^+ layer grown for 120 minutes, which is about 0.5 μm . Table 3.6 lists the initial performance of a set of devices that

Table 3.6. The performance of a set of devices with different n^+ layer thickness by the triode PECVD. Contact is 200 nm ITO.

n^+ layer thickness (μm)	F.F.	V_{oc} (V)	I_{sc} (mA/cm^2)
1 (1/1542)	0.642	0.778	9.5
0.1 (1/1543)	0.637	0.771	10.2
1 (1/1544)	0.639	0.775	9.2

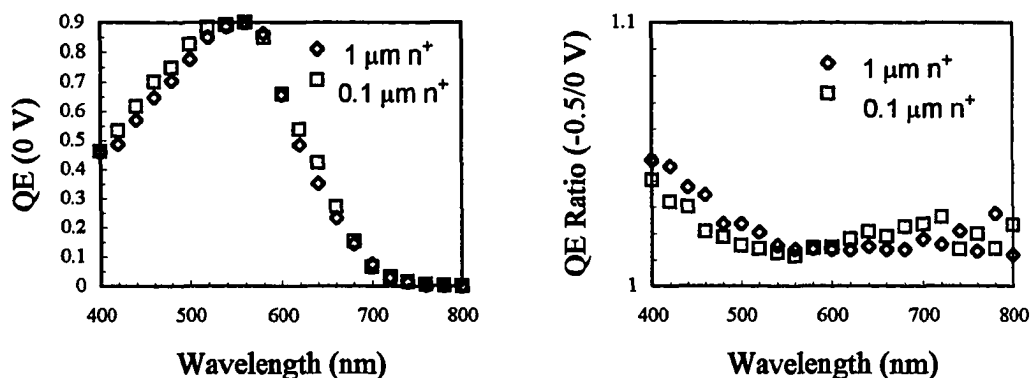


Figure 3.23. QE measurements of the devices with different n^+ layer thickness'.

were grown consecutively. Figure 3.23 shows the QE measurements for these devices. Instead of a positive forward bias, the reverse bias was applied to measure the QE ratio (-0.5/0 V). Since the interest is the stability of the bulk material, the reverse bias would help to distinguish the material properties from other factors. From the QE measurements, it is seen that the initial performance of the devices are quite comparable to each other.

To further study the difference of the a-Si:H network for the devices with different n^+ layer thicknesses, the devices were degraded under 200 mW/cm^2 Xenon light through the ITO contact. Figure 3.24 shows the degradation of the fill factor, open circuit voltage, short circuit current and the conversion efficiency as a function of the light soaking time. It clearly demonstrates that the device with a thick n^+ layer has a very stable fill factor (only a 6 % drop). The overall efficiency is also very stable (a 10 % drop). On the other hand, the device

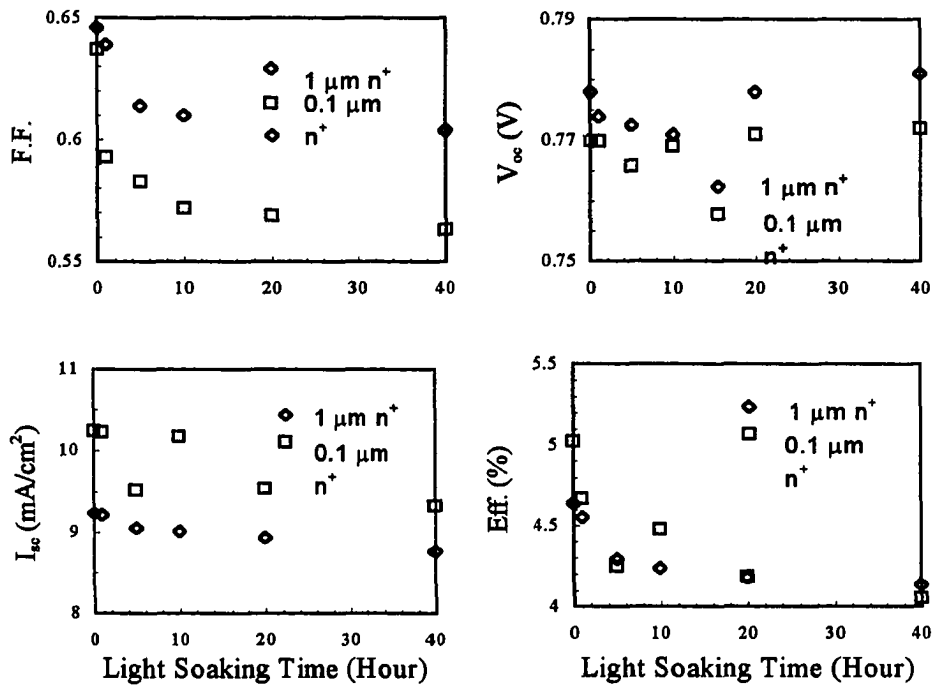


Figure 3.24. The degradation of the fill factor, open circuit voltage, short circuit current and conversion efficiency under 200 mW/cm^2 Xenon light soaking for devices with different n^+ layer thickness?

with thin n^+ layer has a 12 % drop in the fill factor and a 20 % drop in efficiency.

To understand the difference for the degradation of the cells with different n^+ layer thicknesses, it is instructive to look at the QE ratio after the devices were degraded. Figure 3.25 shows the initial QE ratio and the QE ratio after 40 hours under the 200 mW/cm^2 Xenon light soaking. It is clearly seen that the long wavelength collection of holes gets worse in the case of thin n^+ layer. This reflects the fact that the material in the thin n^+ layer device degrades faster. Since the only difference for these two devices is the n^+ layer thickness, it is very natural to attribute this phenomena to the fact that the template layer does improve the quality of the material by passivating the inhomogeneity developed in the growth.

To confirm the result and also see the effects of the buffer layer, another set of devices with a thinner p^+/i buffer layer was made. The new p^+/i buffer layer is only $3/4$ of the previous set. All other growth conditions were kept exactly the same as the previous ones. A too thick p^+/i buffer layer will reduce the strength of the electric field in the cell as the quality of a-(Si,C):H is always not as good as a-Si:H. A too thin p^+/i buffer layer will not be able smoothly connect the p^+/i as the transition of different material cannot happen suddenly. Table 3.7 lists the initial performance of the cells. It is seen that the fill factors are less than the devices with a thick p^+/i buffer layer. The QE measurements, shown in Figure 3.26,

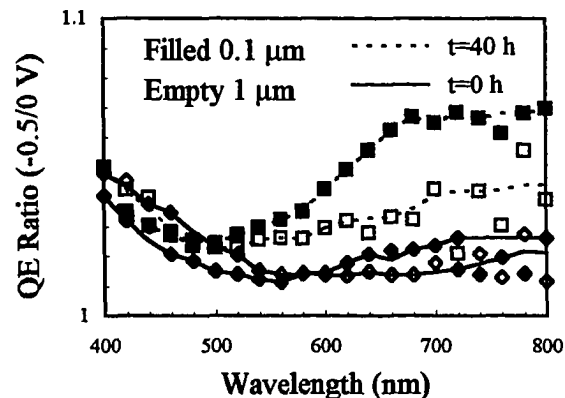


Figure 3.25. QE ratio for the devices with thick and thin n^+ layers at 200 mW/cm^2 Xenon light soaking time 0 and 40 hours.

Table 3.7. Performance of the devices with different n^+ layer thickness by the triode PECVD. The contact is 200 nm ITO. The p^+/i buffer layer is 3/4 of that of Table 3.6.

n^+ layer thickness (μm)	F.F.	V_{oc} (V)	I_{sc} (mA/cm^2)
0.1 (1/1545)	0.614	0.787	9.6
1 (1/1546)	0.600	0.791	10.8

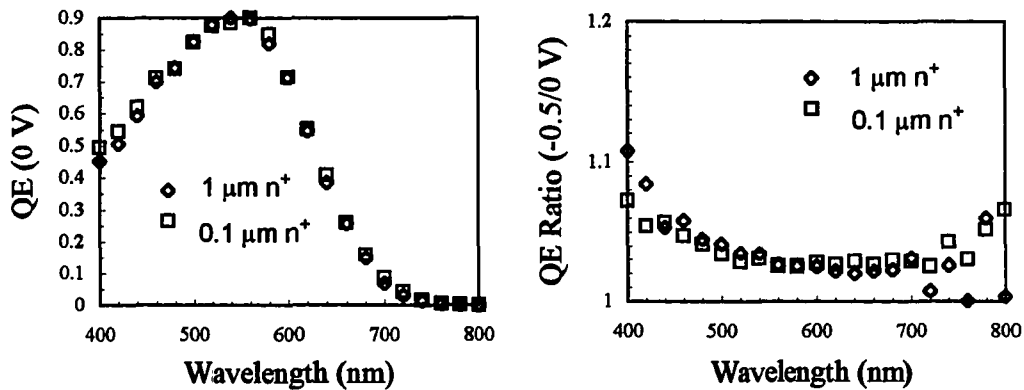


Figure 3.26. QE measurements for devices with different n^+ layer thickness'.

indicates again that the devices are very similar to each other. However, the internal electric field strength is reduced as seen by a high QE ratio.

The stability of these devices was also tested. Although the initial fill factors are not very good, it is the difference between these devices that is interesting to the project. Figure 3.27 shows the degradation of the fill factor, open circuit voltage, short circuit current and conversion efficiency under $200 \text{ mW}/\text{cm}^2$ Xenon light soaking. It is seen again that the fill factor of the device with a thick n^+ layer saturates at a high value and so does the conversion efficiency. It is also seen that the open circuit voltage of both devices first decreases and then increases. This could be due to the defect states induced by prolonged light soaking changing the Fermi level of the material around the p^+/i interface, resulting a better matching. The QE ratio at different light soaking times is plotted in Figure 3.28. This again shows the difference of the degradation of the materials on top of different template n^+ layers. This is shown by the large ratio at long wavelengths for long light soaking times (40 hours).

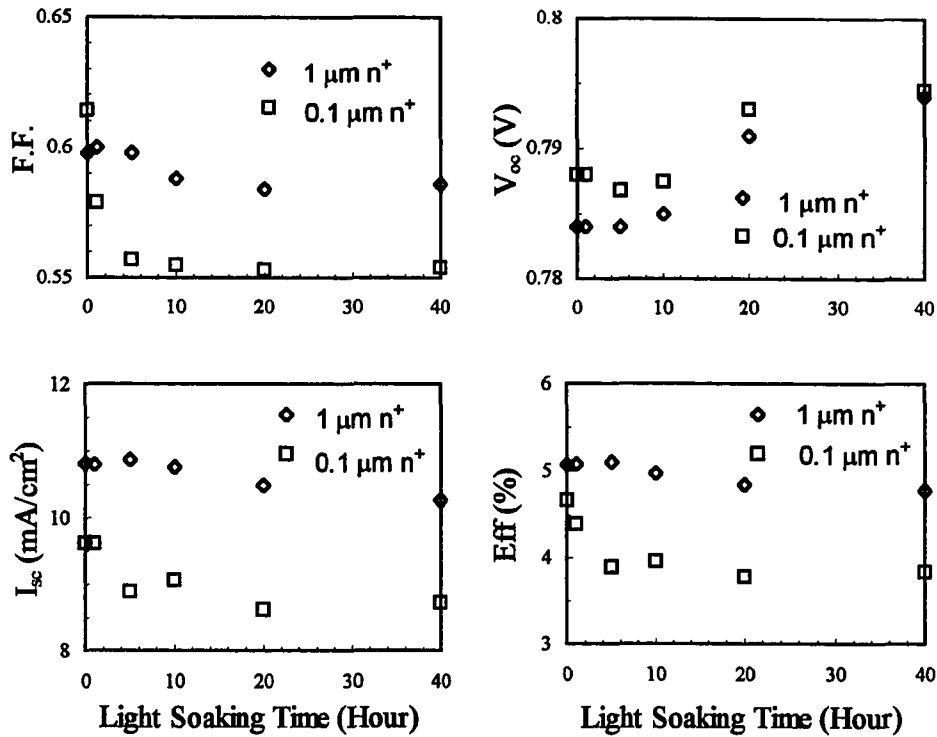


Figure 3.27. The degradation of the fill factor, open circuit voltage, short circuit current and conversion efficiency under 200 mW/cm² Xenon light soaking for devices with different n⁺ layer thickness⁷.

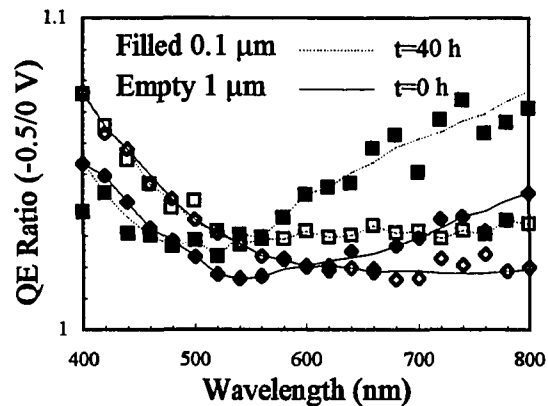


Figure 3.28. QE ratio for devices with different n⁺ layer thickness⁷ at 200 mW/cm² Xenon light soaking time 0 and 40 hours.

4. CONCLUSIONS

The substrate structural $n^+/i/p^+$ solar cell based on a-Si:H and its alloys has been fabricated by a triode PECVD system. The p^+/i interface has been smoothly connected by the compositional variation of the carbon content and it plays a very important role in both initial performance and the stability. The effect of the thickness of the I layer on the performance and the stability were also studied. Low concentration boron compensation in the I layer improves the performance by reducing the contamination from the residual n-type dopant. Temperature grading during the growth was investigated and proven to provide an improvement in the initial efficiency and stability. It is demonstrated that the cell grown on the top of a thick n^+ layer, which meets the needs for a better a-Si:H network, shows a significant improvement in the stability of the performance of the solar cell. In conclusion, the fabrication technique for an a-Si:H substrate solar cell has been developed, the original intuitive idea proven and the development of a more stable solar cell based on a-Si:H material has been shown.

**PART 2. FUNDAMENTAL PROPERTIES OF QUANTUM WELLS WITH
CYLINDRICAL GEOMETRY AND THEIR APPLICATIONS TO
ELECTRONICS AND PHOTONICS**

5. INTRODUCTION

Statement of purpose

This work was aimed to initiate studies of fundamental properties of quantum well (QW) structures with cylindrical geometry, and to propose potential applications of this particular structure in electronics and photonics. QW structures in non-planar configuration have not been seriously studied, either theoretically or experimentally. However, the cylindrical geometry, which alters the coherence of the carriers, could lead to new phenomena. The progress of fabrication technology in last decade now allows the formation of individual QW structures in different geometrical manners, for example the quantum wire (QWI) and quantum dot (QD) structures, so that more fundamental phenomena and useful applications could be explored. It is believed that the trend will continue and expand to yield more functional operations. Specifically, this study investigates the most basic properties, namely the energy levels and tunneling behavior, of electrons in QW structures with cylindrical geometry. The significance of this work is to explore new phenomena and new operations for electronic and photonic devices.

Overview

Fundamentals of semiconductors

The study of semiconductor materials flourished after the discovery of the transistor [32], and the semiconductor laser [33]. The basic principle behind these applications is the electronic and optical properties of semiconductors, especially in the presence of some foreign atoms. Although experimental investigations of these properties gave direct characteristics that could be used for different applications, the really important band theory has played a critical role in understanding and predicting new phenomena. The example could be found in the discovery of semiconductor lasers, in which theory directly guided the lasing in semiconductor materials [34]. Before the discovery of the Bloch theorem [35], the understanding of the material behavior was fragmentary and the explanations of different

phenomena were diverse. It is the Bloch theorem that gives the foundation to develop the band theory to yield a unified explanation to the properties of different materials. Depending on the particular atomic interaction in different materials, band structures have been calculated by various methods from the simplest Kronig-Penny [36] model to the most sophisticated self-consistent methods [37]. The present numerous articles in most leading journals reflect the importance of the state-of-art situation of the understanding of the materials by human beings.

The electronic and optical properties of pure semiconductor materials are dependent on the details of the band structures. However, one particular property of semiconductor materials is the dramatic change of electronic and optical properties by doping. To describe the doping process, one needs to look at the effects of a foreign atom replacing a host atom. It creates some local unbalanced charge inside the material. Under the influence of an external electric field, these local unbalanced charge could be transferred in space, resulting in dramatic change in the electronic properties of semiconductors, from an insulator to a conductor. It is this change of the conductivity, usually in the order of many degrees, that makes semiconductors attractive. In addition to the response to electric fields, semiconductors also respond to light in a very interesting way. When the energy of the light is less than the energy gap, the material is transparent. The same material will turn out to be opaque when the energy of the light is larger than the energy gap. Since semiconductor materials cover the elements of column IV, compound III-V and II-VI in the periodic table, energy gaps have been found to match light from ultraviolet to far infrared, including the most important region, visible light. It is also interesting to understand that some processes are very fast and hence are extremely useful for applications which require short time operation.

The applications of semiconductors are demonstrated by many important devices such as the field effect transistor (FET), the bipolar transistor, light-emitting diode (LED), semiconductor lasers and detectors. With the current technology, especially Si and III-V compounds, the applications of these devices have changed our daily life so much that our thinking started to change. It is the current research interest to use semiconductors as photonic devices. The motivation of this trend is to use the ultimate speed of light to transfer

information, along with the possible low energy consumption. To accomplish this task, new concepts are required and new structures are to be developed. One particular way to achieve this goal is to use the electronic and optical properties of ultrathin layers (in the order of a few nm in thickness) which is usually referred as quantum well (QW). During the last 20 years, this field has been explored extensively.

Fundamentals of semiconductor QW structures

The current large amount of research on semiconductor QW was initiated with a proposal by Esaki and Tsu [38] in 1969. A QW is essentially a one-dimensional potential structure engineered with epitaxy of alternating ultrathin layers. They are usually prepared by molecular beam epitaxy (MBE) and metal-organic chemical vapor deposition (MOCVD). It was theoretically shown that QW structures possess electronic and optical properties of quasi-two(one)-dimensional character in the direction perpendicular (parallel) to the growth axis because the characteristic lengths are smaller than the electron mean free path. A negative differential resistance in I-V characteristic of a GaAs-AlGaAs superlattice (SL) was first observed by Esaki et al [39]. Since then the improvement in growth techniques during the last two decades has made high-quality QW with designed potential profiles as well as impurity distributions in interatomic spacing region. Remarkable progress has been made in this new frontier of semiconductor physics [40].

A typical semiconductor QW structure is illustrated in Figure 5.1. An ultrathin layer with different energy band gap is inserted in a host semiconductor. The heterostructure can be classified into the following four different categories: Type I, type II-staggered, type II-misaligned, and type III. Examples of type I are GaAs-AlAs, GaSb-AlSb, GaAs-GaP, etc., where the energy gap difference $\Delta E_g = \Delta E_c + \Delta E_v$, with ΔE_c (ΔE_v) being the energy difference in the conduction (valence) bands of the two materials. Type II applies to systems like InAs-GaSb, $(\text{InAs})_{1-x}(\text{GaAs})_x - (\text{GaSb})_{1-y}(\text{GaAs})_y$, etc., where the energy-gap difference $\Delta E_g = |\Delta E_c - \Delta E_v|$, and electrons and holes are confined in different materials. Type III is exemplified by HgTe-CdTe where the energy band is more like metal with zero or negative

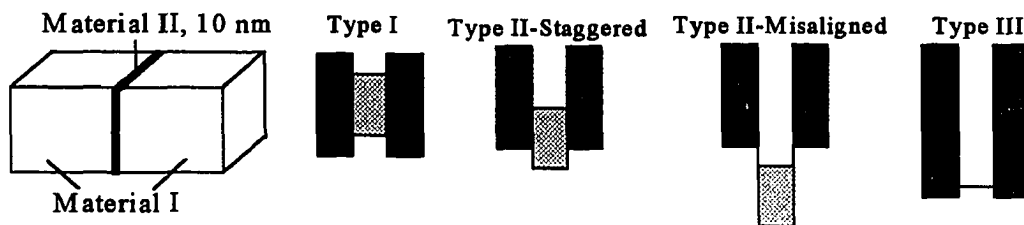


Figure 5.1. A typical QW structure which is an ultrathin layer embedded in a second material. The resultant band structures are also illustrated.

energy gap.

QW structures possess many novel properties including resonant tunneling [41], carrier and exciton confinements [42], non-linear optical properties [43], and quantized Hall effect [44]. Resonant tunneling was observed by Chang et al [41] in double-barrier QW structure. It was found that the resonance is achieved at certain bias voltages when the Fermi level of electrons in the electrode aligns with the energy of the quasi-bound states in QW. The first observation of the confinement states in QW was reported by Dingle et al [42] from optical absorption measurement. Several exciton peaks, associated with different quantum levels of electrons and holes, were also resolved. Tsu et al [45] measured the photo-current for GaAs-GaAlAs superlattice (SL) subject to an electric field. A series of peaks in the photo-current spectrum have been observed which correspond to the transitions between different quantum states in the valence and conduction bands. Therefore, the quantum nature of the structure was confirmed.

Since the discovery of semiconductor QW structures, the majority of the structures studied so far are concerned with the planar structure owing to the planar nature of the fabrication techniques. No matter how perfect the planar layers are, the real structures from this category could never be surface defect free as the boundaries of the layers are not terminated. When the QW is further modified into small structures, this problem becomes worse. However, a special configuration, the cylindrical structure, can in principle eliminate this problem. Figure 5.2 shows a hypothetical structure of such nature. It also consists of layers, in cylinder shape, with lower energy band gap sandwiched in material with higher

energy band gap. This type of structure is a challenge to the current fabrication techniques. Despite the lack of proper fabrication techniques, the structure is still interesting enough to study. The structure is interesting because of the fundamental different coherence of the carrier wavefunction involved and possibility to lead to new devices that operate on new principles.

In addition to new coherence and the reduction of the surface area, another particular interest of the cylindrical QW (CQW) is the response of the structure to an external magnetic field. It is known that the coherence length of the carrier in high quality semiconductor materials exceeds $1 \mu\text{m}$. Therefore, when a magnetic field is applied to a CQW less than that size, strong modulation to the wavefunction can happen to the carrier. The magnetic field has limited effects to the planar QW as the symmetry of the structure would not couple with the field effectively. On the other hand, the magnetic field couples with CQW strongly as the quantum number of the angular momentum comes into picture due to the fact that the boundary is now completely closed.

It is known that an abrupt potential occurs at the interface of two different materials with matched crystal structure due to the potentials contributed by different atoms. This abrupt potential could exist macroscopically in cylindrical geometry as shown in Figure 5.2. Although this abrupt potential fluctuates in the lattice constant scale due to the crystal structures of most semiconductors, it is smooth to the first order if the dimension of the structure is large compared to the lattice constant. Assuming that the well and barrier are

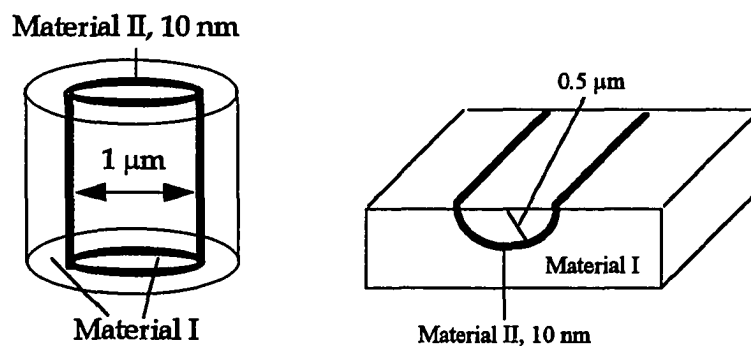


Figure 5.2. The schematic of a QW with cylindrical geometry.

constructed by GaAs and $\text{Al}_x\text{Ga}_{1-x}\text{As}$, the general phenomena associated with planar QW can be studied in CQW as well.

To date, there is no experimental attempt to fabricate a CQW, largely because of the difficulties involved in the growth and regrowth processes. Since the structures are somewhat similar to a QWI, it is instructive to discuss the common fabrication techniques for a QWI [46]. Most growths start with a QW and a QWI is then patterned by chemical etching techniques. The resultant structures usually display high surface states which alter the quantum effect considerably. Combined with the dimensional variation, they could suppress any effect originated from quantum phenomena. When consecutive layers, as in a double CQW, are required, one can imagine that these layers will have no distinguishable quantum effects. Unless techniques such as chemical etching and regrowth are developed within single atomic layer precision in any geometry, the fabrication of the proposed structure is very difficult. The second approach to fabricate a QWI is to use the epitaxial growth on shaped substrates. The layers deposited conform to the curvature of the substrate and the QWI is formed when the curved region is filled. This approach is more suitable for the half cylinder structure shown in Figure 5.2. However, one has the tension problem and the possible variation of the layer thickness, and the difficulties in making contacts.

Previous techniques have been well demonstrated in III-V semiconductors. There is a less known method to fabricate tiny metal wire, the so called nanotube technique [47]. Some porous glass and ceramic materials, when fabricated under certain conditions, can form hollow cylinders. By injecting other materials into the hollow, cylindrical wires could be made. This was successfully done for metals, and has recently been done for semiconductor materials [48]. It is not clear yet how to incorporate different semiconductor materials into the same hollow with control over the layer thickness. Nevertheless, this approach seems more promising to the whole cylinder structure.

6. BASIC THEORY

The band structure of III-V semiconductor compounds

Some III-V semiconductor compounds have a direct energy gap and others have an indirect energy gap. GaAs and $\text{Al}_x\text{Ga}_{1-x}\text{As}$ ($x < 0.4$) with direct gap [49] are the most common materials for fabrication of QWs. Their band structures near the Brillouin zone center are shown in Figure 6.1, where Γ_6 , Γ_7 and Γ_8 indicate symmetries which reveal the most optical and transport properties. The valence bands of light- and heavy-holes are degenerate at Γ_8 point, and the Γ_7 valence band is split by the spin-orbit coupling. The most useful parameters for GaAs and AlAs are listed in Table 6.1. In the table, m^*_e is the effective mass of electron, m^*_{lh} and m^*_{hh} are the effective masses of light- and heavy-holes in units of m_0 the free electron mass, ϵ is the dielectric constant, γ is the Luttinger parameter which is used for band structure calculation and E_g and Δ are the energy gap and the spin-orbit split in the unit of eV.

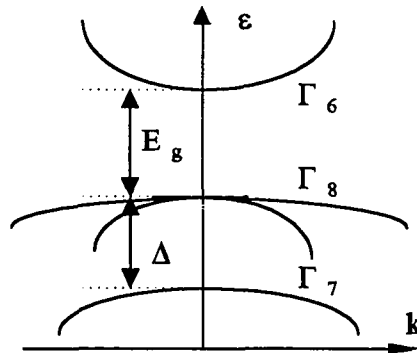


Figure 6.1. Band structure of a direct gap III-V semiconductor in the vicinity of the Brillouin zone center.

Table 6.1 Typical parameters for GaAs-AlAs.

	$m^*_e (m_0)$	$m^*_{lh} (m_0)$	$m^*_{hh} (m_0)$	ϵ	γ	$E_g (0K) (eV)$	$\Delta (eV)$
GaAs	0.067	0.08	0.45	12.5	1.20	1.52	0.34
AlAs	0.124	0.02	0.48	12.5	0.12	3.13	0.275

The envelope function approximation

To describe the band structure of a QW, the Envelope Function Approximation (EFA) [50] has been developed based upon the following two facts in III-V semiconductors; a) most of the host materials display similar band structures, and the periodic part wavefunction of the Bloch function at the band edges does not differ much from one material to another; and b) the relevant electronic structures of heterostructures are often close to the band extreme of the host materials. Thus, only a small fraction of the host Brillouin zone participates in the building of the heterostructure states.

According to the basic band theory, the potential seen by an electron inside a perfect crystal is a periodically changing function in space and the wave function of the electron can be generally written as:

$$\psi = \sum_{A,B} e^{ik_1^A r} u_{nk}^{A,B}(r), \quad (6.1)$$

where A and B represent the species of the compound materials and k is the electron wave vector. $u_{nk}^{A,B}(r)$ is the electron wave function of a unit cell and n is the index of energy bands.

When an ultrathin layer is introduced inside a perfect crystal, the potential seen by the electron is modified by the new species of the layer. Although the periodicity for a perfect crystal does not exist when the ultrathin layer is introduced, the local distortion of the potential allows the EFA, which assumes that the wave function is modulated by the presence of the layer as

$$\psi = \sum_{A,B} e^{ik_1^A z} u_{nk}^{A,B}(z) \chi_l(z), \quad (6.2)$$

where k_1 is the electron wave vector perpendicular to the growth direction and l is an index to characterize different levels. As a result of this approximation, $\chi_l(z)$ is actually determined by simply considering the standard text book quantum mechanics problem, or

$$\left\{ -\frac{\hbar^2}{2} \frac{\partial}{\partial z} \left(\frac{1}{m(z)} \right) \frac{\partial}{\partial z} - V(z) \right\} \chi_l(z) = \epsilon \chi_l(z), \quad (6.3)$$

which differs from 1-d Schrodinger equation by the coordinator dependence of the mass $m(z)$.

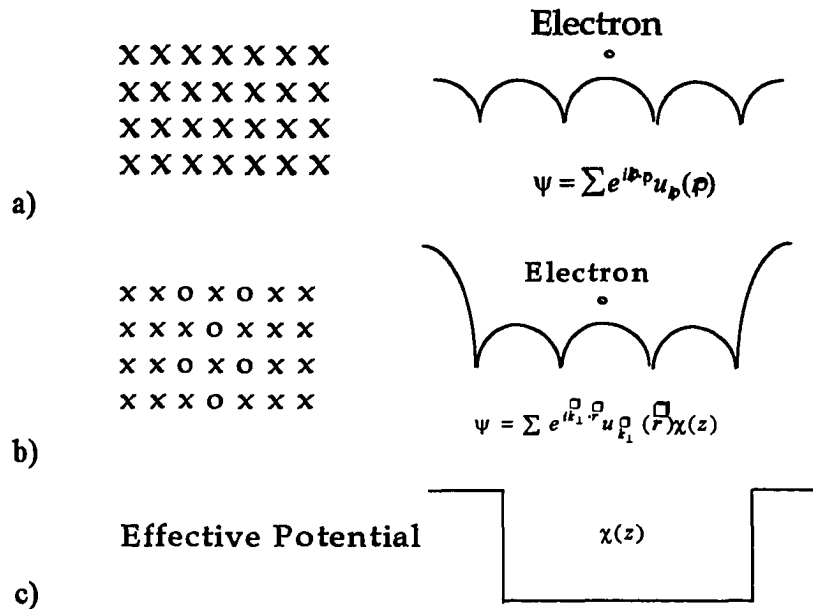


Figure 6.2. Microscopic picture of the QW and the application of the EFA: a) the host structure b) the QW structure c) the effective potential.

The boundary conditions are the continuance of $\chi_l(z)$ and $m^{-1}(z)(\partial\chi_l(z)/\partial z)$ at the interfaces. Figure 6.2. demonstrates the microstructure and the concept of the EFA.

The above theory can be generalized into the cylindrical geometry as shown in Figure 6.3. Instead of a regular arrangement of the atoms with planar geometry, the atoms could be arranged regularly in space to form a pseudo circular shape. Microscopically, the potential is very irregular. However, as one looks at the picture macroscopically, the average potential

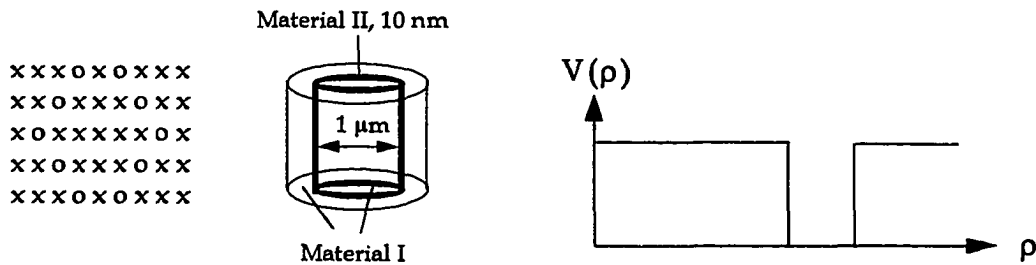


Figure 6.3. The generalization of EFA in CQW.

seen by electrons could be an effective potential that is very similar to the case of the planar structure. The rigorous derivation from basic band structure theory is out of the scope of this study and is left to the band structure specialist.

In analog to the planar QW, the wavefunction of an electron in a CQW is written as

$$\psi = \sum_{A,B} e^{ik_{\perp} \cdot \rho} u_{nk}^{A,B}(\rho) \chi_l(\rho, \phi), \quad (6.4)$$

within the scheme of EFA. The energy levels are determined by

$$\left\{ -\frac{\hbar^2}{2} \left[\frac{1}{\rho} \frac{\partial}{\partial \rho} \left(\frac{\rho}{m(\rho)} \frac{\partial}{\partial \rho} \right) + \frac{1}{\rho^2} \frac{\partial^2}{\partial \phi^2} \right] + V(\rho) \right\} \chi_l(\rho, \phi) = \epsilon \chi_l(\rho, \phi). \quad (6.5)$$

The boundary conditions are the continuance of $\chi_l(\rho, \phi)$ and $(m(\rho))^{-1}(\partial \chi_l(\rho, \phi) / \partial \rho)$ at interfaces.

Basic properties of QW

From basic quantum mechanics [51], the following characteristics are present for a particle inside a potential well: a) energy levels are quantized, as the solution of the Schrodinger equation only exists for certain energies; b) particle is confined in the quantum well, as the wave function decays exponentially outside the well; c) the density of states (DOS) display two dimensional characteristics, as the particle possesses only two degrees of freedom.

Figure 6.4 shows the basic directions that an electron can move in QW structure, I)

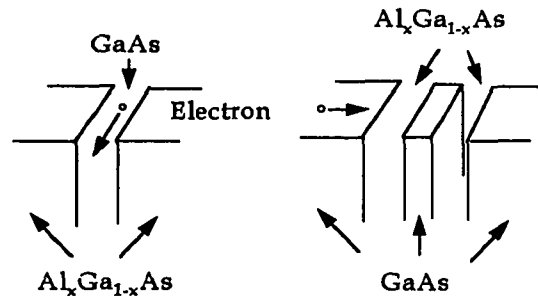


Figure 6.4. Two transport directions of electrons in the QW structure.

perpendicular and II) parallel to the growth direction. In the former case, the carrier is moving only along the direction perpendicular to the growth direction. One astonishing property is the high mobility [52]. The mobility in most semiconductors is limited by the scattering processes [53], for example the interaction between phonons and carriers, and the scattering of impurities. Carriers are usually introduced by dopants in the bulk semiconductor, and inevitably scattering centers appear. In the case of QW, however, the dopants can be located outside the active region (QW) and carriers diffuse into the QW. Therefore, those carriers are free from the scattering of dopant atoms. The mobility is only limited by the phonon scattering and few defects in the structure, for example the interface roughness.

For the transportation in the parallel direction to the growth direction, it is the quantum tunneling that dominates. It was the first dramatic property discovered in the QW structure. Here, classical electron transport theory fails and one has to consider the wave nature of electrons that cause the current under the influence of an applied bias [54]. In addition, the quantum tunneling is so strong that it can be easily observed at room temperature.

The QW structure is fundamentally different from the bulk material, especially for the optical properties. Since the carriers are confined in the growth direction, their response to light is very different from the bulk. One distinguishing difference is the DOS which leads to very dramatic optical properties for the QW. Figure 6.5 compares the DOS for 2- and 3-dimensional systems. In the 3-dimensional case, the DOS is a continuous function which extend to the bottom of the conduction band. In a QW, the quantized nature of the structure forbids the optical transition below the first subband. The entire spectrum will shift due to the absence of allowed states at the bottom of the conduction band. In addition, the step change

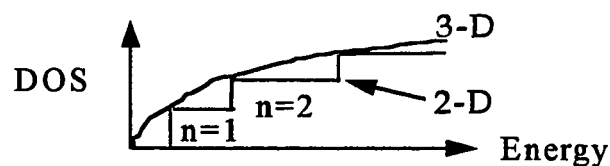


Figure 6.5. DOS of 2- and 3-dimensional systems.

in DOS induces a series of peaks in the optical spectrum.

Another important property of QW structures is the electron-hole pair, also called an exciton, as shown in Figure 6.6. At room temperature, the exciton usually does not exist in most semiconductor bulk materials due to the relatively weak coherence. In the QW, the quantum confinement localizes the electrons and holes and results in a large wavefunction overlapping between the electron and hole. Therefore, exciton transition can be observed even at room temperature [43]. As a result of the strong excitonic effect, most optical devices based on QW structures have to consider the effects from excitons.

Carriers in the bulk material respond to light by certain speed which is mainly determined by the dynamic processes in the material, for example the diffusion of carriers and the interactions the carriers are experiencing. The interaction between carriers usually finishes very fast and the diffusion process in most bulk material is not fast due to the fact that a large carrier concentration gradient is difficult to create. In QW structure, on the other hand, the sharp heterostructure provides a large gradient for the carriers. Therefore, the capture of carriers into QW is fast as shown in Figure 6.7. Along with the fast capture, the captured

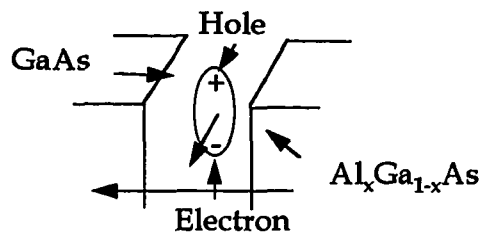


Figure 6.6. An electron-hole pair, also called exciton, in QW.

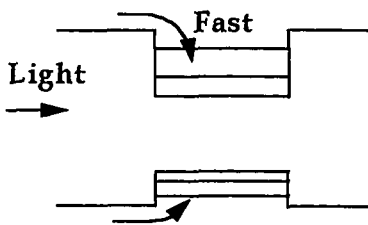


Figure 6.7. The fast capture of the carrier excited in the barrier into well region.

carriers usually have fast dynamics due to the strong spatial coherence inside the QW. This is important to the future applications in the fast opto-electronics and electro-optics [55].

Applications of QW structures

Electronic devices based on parallel transport

The superior electronic properties of the carriers on the plane of heterojunction has led to some very important electronic devices. One of them is called high electron mobility transistor [56]. The basic working principle is shown in Figure 6.8. By using the high electron mobility in the channel, the speed of the device is very fast. It has been reported that the speed of the devices is well over 100 GHz [57].

Electronic devices based on perpendicular transport

For the transport in the perpendicular direction, quantum tunneling comes into picture. Figure 6.9 shows a so called double-barrier tunneling diode (DBTD) which utilizes the transport

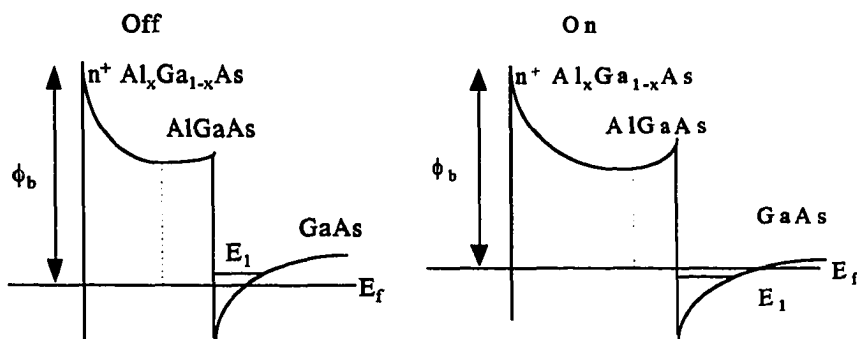


Figure 6.8. Band diagram of a high electron mobility transistor at on and off states.

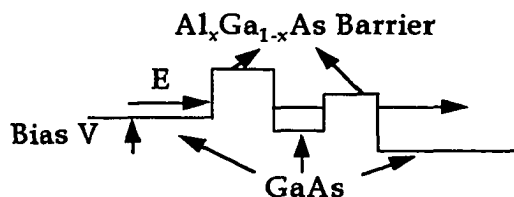


Figure 6.9. Band diagram of a double-barrier resonant tunneling structure.

properties in the perpendicular direction [58]. When the applied bias aligns the Fermi level of the electrode on the left to the quasi-level in the well, the carriers would tunnel through the structure and get collected by the electrode on the right side. Therefore, the I-V characteristics show a strong peak where negative differential resistance was found. The speed of this device is also very high since the tunneling process in semiconductor is extremely fast.

QW laser

The particular properties of QW structures opened a door to better semiconductor laser [59]. Figure 6.10 shows the basic principle of the QW laser. Spontaneous quantum efficiency in QW materials is better than the corresponding double-heterostructure (DH) material, due to the enhancement of the 2-dimensional radiative recombination, and diminished nonradiative recombination. This enhanced efficiency leads to enhanced inversion of carriers at a given injection. The particular DOS of QW increases the gain at low injection and lower absorption coefficient in unexcited QW layer than in a DH layer. Therefore, semiconductor laser with extremely low threshold and long operating time has been achieved.

Long wavelength detector

Light detector is becoming important for the information era. The information that light can carry is much more than electrons. In addition, the speed of the electron in most material is one order less than that of the light. Therefore, the ultimate fast device would be a device operating on the transfer of light, also called photon. It is relatively difficult to make long wavelength detector, since the small energy involved usually causes noises in the low gap semiconductor material due to the thermal disturbance at room temperature. However, the

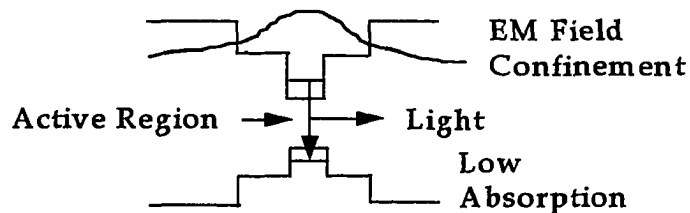


Figure 6.10. Band diagram of semiconductor QW Laser.

transition between subbands of the QW allows the detection of signals with long wavelength [60]. The signal can excite the transition between different subband levels. When the cascade mechanism is used as shown in Figure 6.11, the detection of the signal can be achieved.

Modulator

In bulk semiconductors, the carrier DOS is usually not concentrated and exciton is missing at room temperature. Therefore, it is relatively difficult to modulate the properties of the material by light with normal power incident. In the quantum well structure, on the other hand, the carriers in the barriers tend to diffuse into the well and occupy in a relatively large concentrated DOS. In addition, the enhanced coherence helps the existence of exciton. Therefore, the modulation of QW is much easier, for example the modulation of the refractive index is very strong for QW structure by an electric field. Figure 6.12 shows a working QW modulator by external electric field [61].

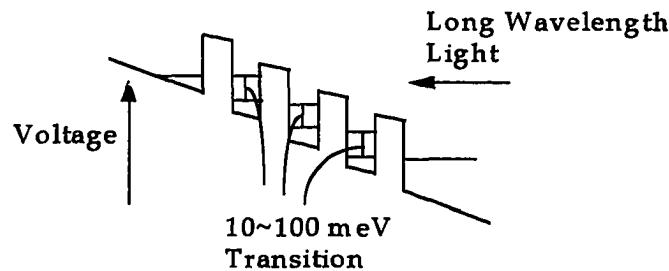


Figure 6.11. Long wavelength detector by the subband transition in QW.

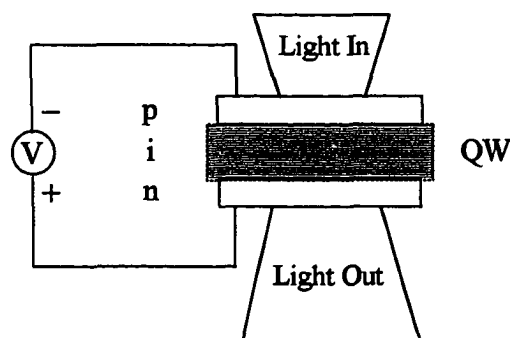


Figure 6.12. Light modulator by the electro-optic effect of QW structure.

7. FUNDAMENTAL PROPERTIES OF CQW

Energy levels of CQW

In a planar QW, energy levels depend on the well thickness and the barrier height. Consequently, these parameters are important to the electronic and optical properties. For a CQW, in addition to these parameters, the size of the structures becomes important too. There are two competitive factors, the technological limits in defining small features and the quantum phenomena at that scale. It becomes much more difficult to define simple geometrical patterns less than $0.1 \mu\text{m}$ by the current technology, and CQWs are limited by this size. On the other hand, as the size of the CQW increases, the particular quantum phenomena associated with this geometry is reduced due to a) the structure is approaching planar one, and b) the loss of the carrier coherence for large distance. In what follows, CQW about $0.5 \mu\text{m}$ in size will be considered. Results of electrons are mainly presented. Energy levels of holes are much more complicated due to the band mixing and non-parabolic bands. However, the large mobility of electrons in most semiconductors favors devices operating by electrons. Furthermore, holes are less affected by a magnetic field due to the heavier effective mass.

Energy levels of CQWs under the influence of a magnetic field were studied for infinite barrier and extremely small structure (400 \AA) [62]. It is practically impossible to fabricate them by the current technology. Therefore, larger structures with finite barriers were studied [63]. The wells and barriers are constructed by GaAs and $\text{Al}_x\text{Ga}_{1-x}\text{As}$. The Hamiltonian of an electron with effective mass $m_{w,b}^*$ (w and b represent well and barrier regions) and charge q , in the presence of a magnetic field, is then written as

$$H = \frac{(-i\hbar\nabla - q\vec{A})^2}{2m_{w,b}^*} + V_{w,b}(\rho), \quad (7.1)$$

with $\vec{A} = \vec{B} \times \vec{r} / 2$ being the vector potential of the magnetic field expressed in Landau gauge.

By writing the wavefunction as $\Psi(\vec{r}) = R(\rho)e^{i(m\phi + k_x z)}$, and defining the following variables,

$$\xi = \frac{eB\rho^2}{2\kappa}, \quad \omega_B = \frac{eB}{m_{w,b}^*}, \quad E_\rho = E - \frac{\eta^2 k_z^2}{2m_{w,b}^*}, \quad (7.2)$$

Eq. (7.1) becomes

$$\xi R' + R + \left[-\frac{\xi}{4} + \beta - \frac{m^2}{4\xi}\right] R = 0, \quad (7.3)$$

with $\beta = \frac{E_\rho - V_{w,b}(\rho)}{\eta\omega_B} - \frac{m}{2}$. The general solution to Eq. (7.3) is

$$R(\xi) = e^{-\xi/2} \xi^{m/2} [AM(a, b, \xi) + BU(a, b, \xi)], \quad (7.4)$$

with $b = |m| + 1$ and $a = -\left(\beta - \frac{|m|}{2} - \frac{1}{2}\right)$. $M(a, b, \xi)$ and $U(a, b, \xi)$ are the confluent

hypergeometric functions [64]. They can be expressed by the following series

$$M(a, b, \xi) = \sum_n \frac{(a)_n \xi^n}{(b)_n n!}, \quad (a)_n = a(a+1)(a+2)\dots(a+n-1), \quad (a)_0 = 1, \quad (7.5a)$$

$$U(a, b, \xi) = \frac{\pi}{\sin \pi b} \left\{ \frac{M(a, b, \xi)}{\Gamma(1+a-b)\Gamma(b)} - \xi^{1-b} \frac{M(1+a-b, 2-b, \xi)}{\Gamma(a)\Gamma(2-b)} \right\}. \quad (7.5b)$$

When the magnetic field is set to zero, the solution becomes

$$\Psi(\rho, z, \phi) = e^{i(m\phi + k_z z)} \begin{cases} [AJ_m(\beta\rho) + BY_m(\beta\rho)] \\ [CI_m(\eta\rho) + DK_m(\eta\rho)] \end{cases}, \quad (7.6)$$

with

$$\beta = \sqrt{\frac{2m_w^*}{\eta^2} [E_\rho - V_w(\rho)]}, \quad E_\rho > V_w(\rho), \quad (7.7a)$$

$$\eta = \sqrt{\frac{2m_b^*}{\eta^2} [V_b(\rho) - E_\rho]}, \quad V_b(\rho) > E_\rho, \quad (7.7b)$$

where $J_m(x), Y_m(x), I_m(x), K_m(x)$ are the Bessel functions. They can be expressed by the following series

$$J_m(x), I_m(x) = \left(\frac{1}{2}x\right)^m \sum_{n=0}^{\infty} \frac{(-x^2/4)^n, (x^2/4)^n}{n! \Gamma(m+n+1)}, \quad (7.8a)$$

$$Y_m(x), K_m(x) = \frac{J_m(x) \cos(m\pi) - J_{-m}(x)}{\sin(m\pi)}, \frac{1}{2} \pi \frac{I_{-m}(x) - I_m(x)}{\sin(m\pi)}. \quad (7.8b)$$

At interfaces, the following quantities $R(\rho)$ and $(m_{wb}^*)^{-1} (\partial \ln R(\rho) / \partial \rho)$ are continuous.

Figure 7.1 shows the development of an iteration relation based on these continuities. For an arbitrary barrier in the structure, two quantities that depend only on the wavefunction and their derivatives are connected by

$$\beta_l = \frac{\alpha_{l-1} \Sigma - \Sigma^l}{\Xi^l - \alpha_{l-1} \Xi} \Big|_{R_l(w,b)}, \quad \alpha_l = \left(\frac{m_b^*}{m_w^*} \right)^l \frac{\Sigma^l + \beta_l \Xi}{\Sigma + \beta_l \Xi} \Big|_{R_l(w,b) + (a,b)}, \quad (7.9)$$

with $l=1, -1$ for the right and left interfaces of the barrier. At the interfaces of the out most buffer barriers, we have

$$\alpha_0 = \frac{m_b^* \Sigma^l}{m_w^* \Sigma} \Big|_{R_0}, \quad \alpha_n = \frac{m_b^* \Xi}{m_w^* \Xi} \Big|_{R_n}, \quad (7.10)$$

where

$$\Sigma = e^{-\xi/2} \xi^{l|m/2} M(a, b, \xi), (J_m(\beta \rho), I_m(\eta \rho)), \quad (7.11a)$$

$$\Xi = e^{-\xi/2} \xi^{l|m/2} U(a, b, \xi), (Y_m(\beta \rho), K_m(\eta \rho)), \quad (7.11b)$$

are used to represent the wavefunction in each barrier and well. In writing Eq. (7.10), the boundary conditions of wavefunction at origin and infinite are used. The energy levels are then obtained by matching the α_n iterated by Eq. (7.9) and the α_n by Eq. (7.10) directly.

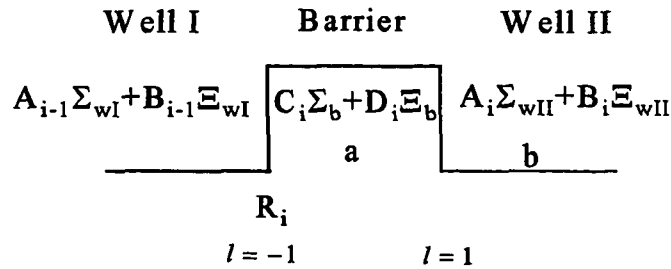


Figure 7.1. The development of an iteration relation by using the continuity of the wavefunction at the interfaces.

First, single and double CQW structures are considered. Figure 7.2 shows the energy levels of an electron in a 50 Å GaAs single and a 100-50-100 Å GaAs-Al_{0.15}Ga_{0.85}-GaAs double CQW embedded in Al_{0.15}Ga_{0.85} buffer material as a function of the azimuth number, m . The radius of the inner buffer barrier, r_0 , is 2500 Å. The following material parameters [65] $m_w=0.067m_0$ and $m_b=(0.067+0.083x)m_0$ are used. The empirical expression, $E_c=1.155x+0.37x^2$ (eV), has been used for the direct gap band difference between GaAs and Al_xGa_{1-x}As. Conduction band offset (barrier height V_0) is taken to be 60% of this difference. From Figure 7.2, it is seen that the energy levels increase non linearly with m as a result of the increase of the angular energy. The energy difference between two consecutive m 's shows an almost linear dependence for large m . For small m , an oscillation is seen and it is very noticeable in the double CQW. This is attributed to the specific coherence of the Bessel function which

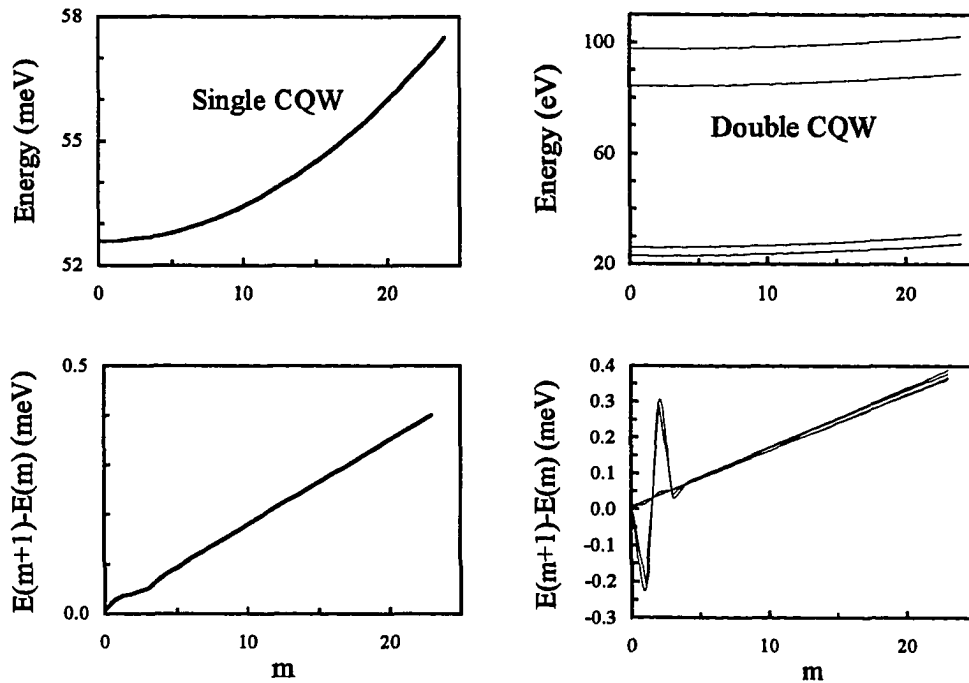


Figure 7.2. Energy levels of an electron in a 50 Å single GaAs and a 100-50-100 Å GaAs-Al_{0.15}Ga_{0.85}As-GaAs double CQW embedded in Al_{0.15}Ga_{0.85}As buffer barriers as a function of the azimuth number, m .

changes significantly for small m .

The energy of an electron in a planar QW can be written as

$$E = E_z(i) + \eta^2 (k_x^2 + k_y^2) / 2m_t, \quad (7.12)$$

and the energy of an electron in a cylindrical QW is

$$E = E_\rho(i, M) + \eta^2 k_z^2 / 2m_l. \quad (7.13)$$

They correspond to 2- and 1-dimensional systems. Figure 7.3 depicts the DOS of the CQW which is characterized by sharp peaks. However, when the difference of the energy for the consecutive m 's are very small such as the case of very large radius, the structure is equivalent to a 2-dimensional system.

When a magnetic field is present, the energy levels shown in Figure 7.2 change.

Figure 7.4 plots the energy levels of the single and double CQW of Figure 7.2 as a function of m for magnetic fields 0.5 and 1.5 Tesla (T). Almost linear behavior is seen, which is similar to the Zeeman splitting of the energy levels of an atom in a magnetic field. For large magnetic field, the number of the bound levels is reduced in the double CQW. It is also interesting to notice that the selection rule of the optical band-to-band transition for the structure requires that $m_e = m_h$ for non-circular polarized light. Since holes and electrons carry opposite charges, the transition energy is nearly a constant for different m , a character which is very important for potential applications of CQW.

Figure 7.5 shows the energy levels of the single and double CQW of Figure 3.2 as a function of the magnetic field for $m = 0, \pm 2$. A steady increase of energy levels is seen as the magnetic field becomes strong. The amount of the increase is as much as 100 meV for the

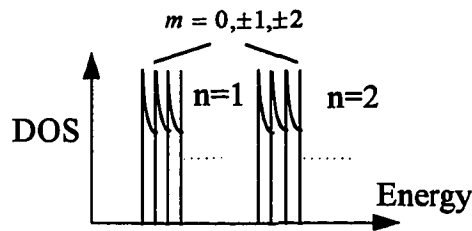


Figure 7.3. The particular DOS of the CQW.

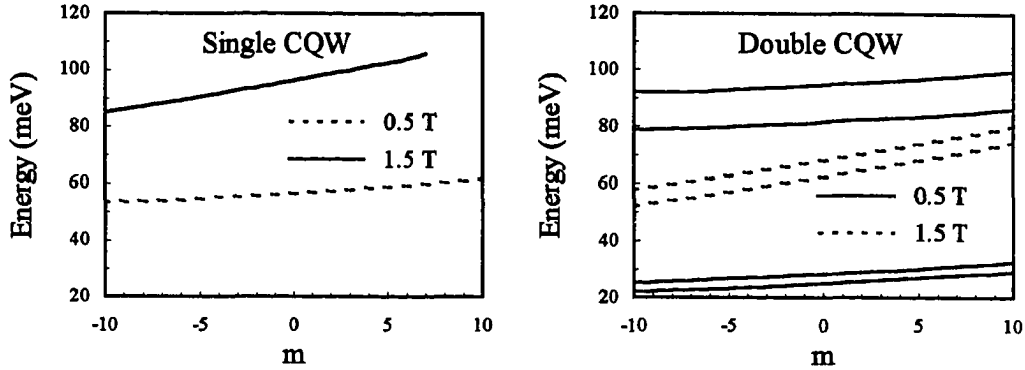


Figure 7.4. The energy levels of an electron in the single and double CQW of Figure 7.2 as a function of m for magnetic field 0.5 and 1.5 T.

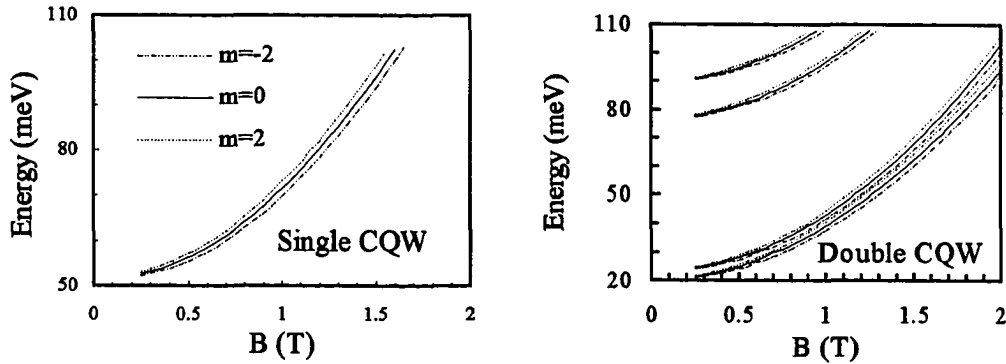


Figure 7.5. Energy levels of an electron in the single and double CQW of Figure 7.2 as a function of the magnetic field for $m = 0, \pm 2$.

first level of the double CQW as the magnetic field increases from 0 to 2 T. Magnetic field is known to have profound effects on the electronic and optical properties of semiconductors macroscopically by microscopically quantizing the band structure or localizing the electrons and holes. When the system becomes small, magnetic field starts to affect the coherence of the particle wavefunction significantly. The magnetic field produces an effective potential to the carriers in the small structure and it changes energy levels. The prerequisite is that the coherence of the electron is preserved.

There is an interesting phenomena associated with the double CQW as the barrier width changes. The coupling between the two wells decreases exponentially as the middle barrier becomes thick. In a double planar QW, the wells are almost identical for very thick barrier, resulting in a degeneracy in the energy levels. For a double CQW, the geometry and the magnetic field break the symmetry and the degeneracy is lifted. Figure 7.6 shows the energy levels and the difference of the coupled energy levels of the double CQW of Figure 7.2 as a function of the barrier thickness for magnetic field 0.5 and 1.5 T. As the thickness of the barrier increases, instead of occurring a degeneracy of the coupled levels, they deviate from each other after reaching a minimum. If one recalls that the effective potential induced by the magnetic field increases as the barrier becomes thicker. One realizes that the competition between the decrease of the coupling and the increase of the effective potential results in a local minimum.

Apart from the magnetic field, another important parameter of the structure is the radius of the inner buffer barrier, r_0 . For large r_0 , the electron coherence is randomized by various scattering during the circulation inside the well, and consequently quantum effects would be weakened. To preserve the coherence, small r_0 is desired because of less scattering during the circulation. Figure 7.7 shows the energy levels of the single and double CQW of

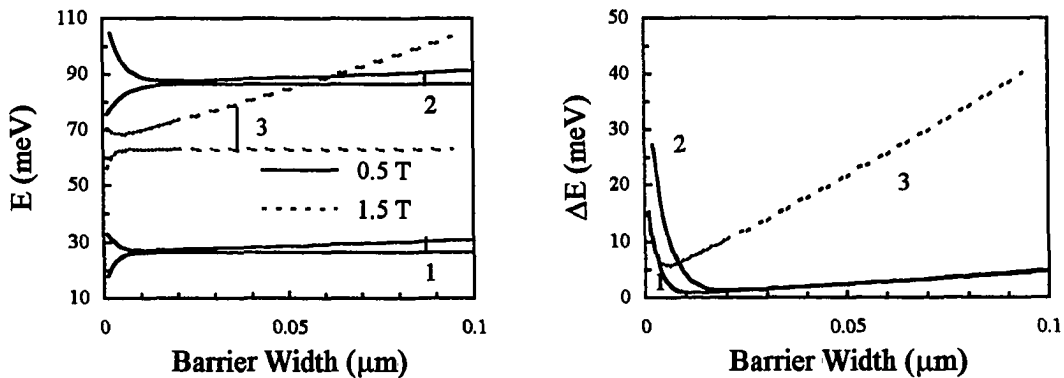


Figure 7.6. The energy levels ($m=0$) and the difference of the coupled energy levels of the double CQW of Figure 7.2 as a function of the barrier width for magnetic field 0.5 and 1.5 T.

Figure 7.2 as a function of r_0 for magnetic field 0, 0.5 and 1.5 T. For the case of the double CQW without magnetic field, only the lowest level is shown. It is seen that the energy levels increase as r_0 increases, and for large magnetic field, the increase is faster. This is understood by the fact that the effective potential produced by a constant magnetic field is proportional to the square of the radius as Eq. (7.3) indicates. However, one should be reminded that this is only true when the carrier coherence is preserved.

The above results could lead to a potential application for a potential *in-situ* tunable semiconductor laser. To tune a laser, one prerequisite is that the emission spectrum consists of the desired lasing energy. By the help of external mirror, this lasing energy can be amplified. For the lasing energy outside the emission spectrum, a new laser structure ought be

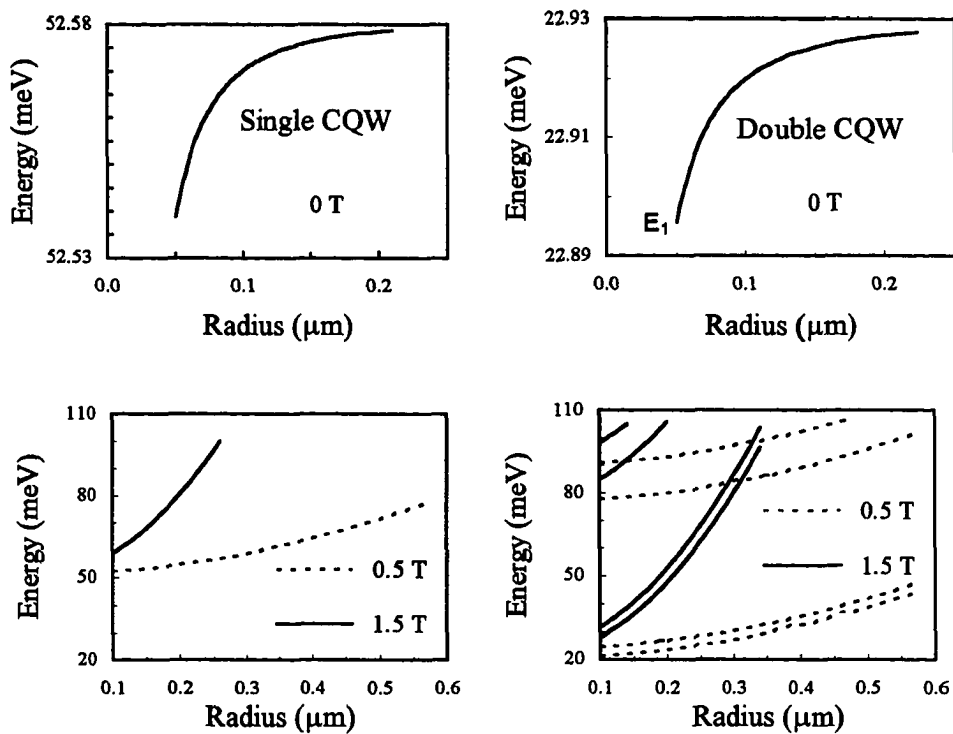


Figure 7.7. Energy levels ($m=0$) of an electron in the single and double CQW of Figure 7.2 as a function of the radius of the inner buffer barrier, r_0 , for magnetic field 0, 0.5 and 1.5 T.

built. By choosing a specific chemical composition for the active region of the laser, the wavelength of the lasing light could be changed in a wide range (roughly from 630 nm to 2 μm) by the current technology. Normally, there is also a tuning section needed. To date, the most promising one is the distributed Bragg reflector (DBR) whose refractive index can be electrically controlled by the carrier plasma in the DBR region. The lasing light can be changed by controlling the tuning section, provide that the spectrum of the active region is rich. It is important in technology and of fundamental interests as well that one can change the operating wavelength in a wide range after fabrication. If the spectrum of a laser extends over a fairly large region, the lasing energy can be tuned easily. However, a broad spectrum means a distribution of energy. When a particular energy is chosen for lasing, other energies are lost. Hence, it is very important to be able to tune a narrow spectrum in a wide range.

It is now very common to fabricate semiconductor laser by QW structure and the size has been reduced toward submicron range. QW laser has a narrower spectrum than that of the corresponding bulk one. The emission spectrum of the active region can be modified by the appropriate choice of materials and designs of the structures, a procedure depending on fabrication processes. To yield *in-situ* tuning, an external force is needed to continuously modify the emission spectrum of the active layer without significantly affecting other useful components. Controlling the emission spectrum through electric field requires additional electrodes which is not desirable for small semiconductor laser. Therefore, magnetic field is an ideal candidate to achieve such task. The magnetic field induces an effective potential that can change the emission spectrum as shown before, and it can also preserve the coherence of the carrier. As long as the time takes for the carrier circulation is less than the spontaneous radiative lifetime, the carrier will respond to the magnetic field. Furthermore, the selection rule of the optical band-to-band transition for the structure and the fact that holes and electrons carry opposite charges lead to a nearly constant transition energy for different m . As the magnetic field strength increases, this energy difference increases and so does the lasing light. One additional advantage of the CQW structure is the 1-dimensional DOS which further enhances the optical transition.

Tunneling in CQW

I-V characteristics of DBTD with cylindrical geometry

DBTD, the device demonstrated the importance of QW structure, has been drawing a great deal of attention because tunneling is the fastest charge transportation phenomena in semiconductors. Many important properties, such as negative differential resistance, oscillation or instability, have been discovered [66]. In device fabrication, high quality DBTD of planar geometry is achieved by MBE or MOCVD. DBTD with cylindrical geometry has not been attempted experimentally. Theoretically, they have been studied by Ping and Dalal [67] for absolute zero temperature. Interesting features, originating from the geometrical property of the structure, have been revealed in the transmission spectra and I-V characteristics. More studies have recently been done by Ping [68] for the effects of the temperature, structural parameters and geometrical configurations on the properties of the radial tunneling.

There are many approaches to study the tunneling behavior. The most successful method so far is the transfer matrix formalism. The simplest version of the transfer matrix approach is to consider the wells and barriers separately and match them according to the boundary conditions. This method is unsatisfactory to reproduce experimental results of planar DBTD, due to the neglect of: 1) quantum repulsion from the barrier on carrier distribution; 2) the non-equilibrium nature of the process; 3) the effects of phonons and defects. Much more realistic and sophisticated techniques, such as the self-consistent method including the effects of phonons and defects, have been introduced [69]. However, the transfer matrix method can provide the most basic features of the I-V characteristics of DBTD.

The cylindrical DBTD (CDBTD) to be studied and the simplified band diagram are schematically shown in Figure 7.8. In the figure, ρ_c , b and a are the radius of the first barrier, the well width and barrier thickness, respectively. V_0 and V_a are the barrier height and applied bias. Two contacts ($R_1 < \rho_c$ and $R_2 > \rho_c + 2a + b$) are introduced in the structure to collect and eject carriers. It is assumed that carriers are thermalized at these contacts and the speed of thermalization is fast enough to produce a uniform distribution of the carriers at the surface of contacts. Under these

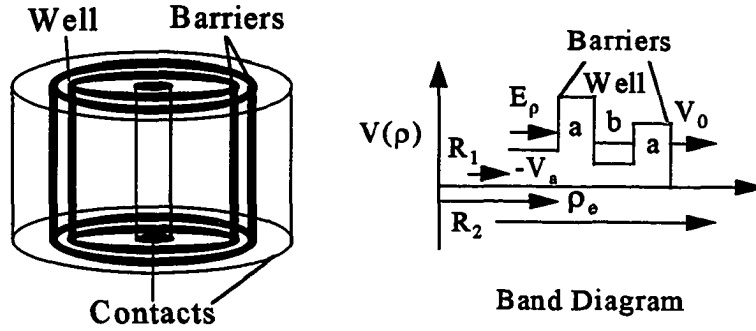


Figure 7.8. Schematic and band diagram of CDBTD.

assumptions, the time-dependent Schrodinger equation for an electron with effective mass $m^*(\rho)$ in the region between the contacts is written as

$$i\eta \frac{\partial \Psi(\rho, t)}{\partial t} = H \Psi(\rho, t) \quad (7.14)$$

with

$$H = -\frac{\eta^2}{2} \left[\frac{1}{\rho} \frac{\partial}{\partial \rho} \left(\frac{\rho}{m^*(\rho)} \frac{\partial}{\partial \rho} \right) + \frac{1}{\rho^2} \frac{\partial^2}{\partial \phi^2} + \frac{\partial^2}{\partial z^2} \right] + V(\rho) \quad (7.15)$$

which will be solved.

In the following, we use m_w for the electron effective mass of the emitter, well and collector (GaAs); and m_b for the electron effective mass of the barriers ($\text{Al}_x\text{Ga}_{1-x}\text{As}$). In lieu of a self-consistent solution of the Poisson equation, we assume that the potential is constant in each well and barrier and the total voltage drop is distributed equally at each of the heterointerfaces. Thus, the potential profile is written as

$$V(\rho) = \begin{cases} \frac{(1-i)}{2} V_a; & i = 1, 2, 3; \\ V_0 - \frac{(j-1)}{2} V_a; & j = 1, 2, \end{cases} \quad (7.16)$$

where $i=1, 2, 3$ represent the emitter, well and collector and $j=1, 2$ the two barriers. In writing Eq. (7.16), the band bending due to carrier redistribution has been neglected. Following standard variable separation, the wavefunction is written as $\Psi(\rho, \phi, z, t) = \theta(\rho) Z(z) e^{i l \phi} e^{-i E t / \eta}$. Then

$\theta(\rho)$ is determined by

$$\frac{\partial^2 \theta(\rho)}{\partial \rho^2} + \frac{1}{\rho} \frac{\partial \theta(\rho)}{\partial \rho} + \left\{ \frac{2m_w b(\rho)}{\eta^2} [E_\rho - V(\rho)] - \frac{l^2}{\rho^2} \right\} \theta(\rho) = 0, \quad (7.17)$$

where $E_\rho = E - E_z$ is the radial energy. the states with $E_\rho > 0$ are interested as they produce the current. In the z direction, it is assumed that the ends of the CDBTD are far apart and the potential of the wall is infinitely large. Therefore, there are only stationary states in this direction and no current exists. Since the carriers flow in and out the contacts and the thermalization there is assumed to be fast, current flow circle is defined. We have simplified the whole problem to the extent that the mathematics involved is easy to handle. The traveling wave solutions to Eq. (7.17) in different regions are

$$\theta(\rho) = \begin{cases} H_l^{(1)}(k_1 \rho) + R H_l^{(2)}(k_1 \rho); & R_1 < \rho < \rho_e, \\ A_1 I_1(\eta_1 \rho) + B_1 K_1(\eta_1 \rho); & \rho_e < \rho < \rho_e + a, \\ C_1 H_l^{(1)}(k_2 \rho) + D_1 H_l^{(2)}(k_2 \rho); & \rho_e + a < \rho < \rho_e + a + b, \\ A_2 I_1(\eta_2 \rho) + B_2 K_1(\eta_2 \rho); & \rho_e + a + b < \rho < \rho_e + 2a + b, \\ T H_l^{(1)}(k_3 \rho); & \rho_e + 2a + b < \rho < R_2, \end{cases} \quad (7.18)$$

with

$$k_i = \eta^{-1} \sqrt{2m_w(E_\rho + eV_a(i-1)/2)}, \quad i = 1, 2, 3, \quad (7.19a)$$

$$\eta_j = \eta^{-1} \sqrt{2m_b(V_0 - E_\rho - eV_a(j-1)/2)}, \quad j = 1, 2. \quad (7.19b)$$

Here, $H_l^{(1,2)}(x)$, $I_l(x)$ and $K_l(x)$ represent the Hankel functions and modified Bessel functions of the first and second kind. The radial current density, for an electron with energy $E = E_\rho + E_z$ and the azimuth number l , can be quantum mechanically calculated by

$$j_\rho = \frac{e\eta}{2im_w} [\psi^* \nabla \psi - (\nabla \psi^*) \psi]_\rho = \frac{2e\eta |T|^2}{m_w \rho}. \quad (7.20)$$

Summing for all possible states in the contacts, the total radial current density per unit length is

$$J = \int_0^\infty \frac{4e\sqrt{2m_w} |T(E_\rho, V_a)|^2}{\pi \eta^2 (\rho_e + 2a + b)} dE_\rho \int_0^\infty [f(E_\rho + E_z) - f(E_\rho + E_z + eV_a)] d\sqrt{E_z}, \quad (7.21)$$

where $f(E)$ is the Fermi distribution function. The transmission coefficient, $T(E, V_d)$, can be obtained by the transfer matrix method

$$\begin{pmatrix} 1 \\ R \end{pmatrix} = \begin{pmatrix} M_{11} & M_{12} \\ M_{21} & M_{22} \end{pmatrix} \begin{pmatrix} T \\ 0 \end{pmatrix}, \quad (7.22)$$

which yields $T(E, V_d) = M_{11}^{-1}$. The transfer matrix M is equal to $M(1) * M(2)$ with

$$\begin{aligned} M(i) = & \begin{pmatrix} H_i^{(1)}(k_i \rho_i) & H_i^{(2)}(k_i \rho_i) \\ m_w^{-1} H_i^{(1)\prime}(k_i \rho_i) & m_w^{-1} H_i^{(2)\prime}(k_i \rho_i) \end{pmatrix}^{-1} \begin{pmatrix} I_l(\eta_i \rho_i) & K_l(\eta_i \rho_i) \\ m_b^{-1} I_l'(\eta_i \rho_i) & m_b^{-1} K_l'(\eta_i \rho_i) \end{pmatrix} \\ & \begin{pmatrix} I_l(\eta_i(\rho_i + a)) & K_l(\eta_i(\rho_i + a)) \\ m_b^{-1} I_l'(\eta_i(\rho_i + a)) & m_b^{-1} K_l'(\eta_i(\rho_i + a)) \end{pmatrix}^{-1} \\ & \begin{pmatrix} H_i^{(1)}(k_{i+1}(\rho_i + a)) & H_i^{(2)}(k_{i+1}(\rho_i + a)) \\ m_w^{-1} H_i^{(1)\prime}(k_{i+1}(\rho_i + a)) & m_w^{-1} H_i^{(2)\prime}(k_{i+1}(\rho_i + a)) \end{pmatrix}, \quad (7.23) \end{aligned}$$

and $\rho_i = \rho_e + (i-1)(a+b)$, $i=1,2$. In obtaining Eq. (7.23), continuities of the wavefunction $\theta(\rho)$ and the probability current density $m_{mb}^{-1}(\partial\theta(\rho)/\partial\rho)$ of the electron across the interfaces have been used. Therefore, we can further prove that, by using the above wavefunctions, the probability current density of the electron in the radial direction is conserved which ensures the conservation of the current as well.

The transmission spectra and I-V characteristics are calculated for material parameters used before. The electron Fermi energy, E_f , is 5 meV, corresponding to an electron concentration of about $10^{17}/\text{cm}^3$ near the electrodes of the emitter and collector. Figure 7.9 shows the transmission spectrum of a GaAs-Al_{0.3}Ga_{0.7}As CDBTD with $l=0$ and l , under bias of 0.01 and 0.5 V. The well width (b), barrier thickness (a) and the radius of the first barrier (ρ_e) are 50, 50 and 1000 Å, respectively. For comparison, the transmission spectrum of a planar DBTD with the same parameters is also plotted. It is seen that oscillations appear in the transmission spectrum of the CDBTD, which can be more clearly seen in the enlarged portions (inserts). Mathematically, the cylindrical wave (Hankel function) differs from the plane wave by a more complicated position dependence of amplitude and phase. In addition, the translation invariance of the plane wave is lost in the cylindrical wave. Physically, the phase matching for the transmission has been changed in the

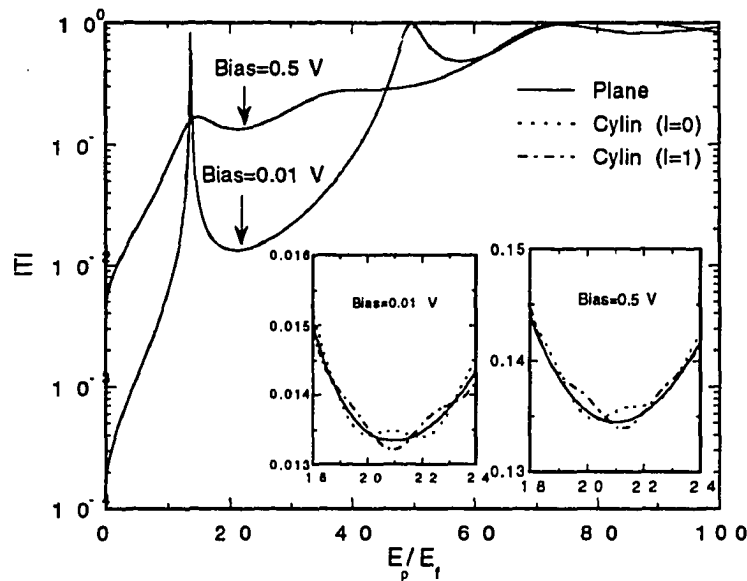


Figure 7.9. Transmission coefficient, $|T|$, v.s. E_p (in unit of E_f) for a GaAs- $\text{Al}_{0.3}\text{Ga}_{0.7}\text{As}$ CDBTD with $l=0$ and 1 states, under bias of 0.01 and 0.5 V. The transmission coefficient for the corresponding planar DBTD is also plotted.

CDBTD. For a CDBTD, the amplitude of the income cylindrical wave at r_0 swings periodically as the energy of the electron, or the argument of the cylindrical wave, changes. This results in the oscillation of the transmission coefficient. As the argument increases, the oscillation decreases and the transmission spectrum of a CDBTD approaches that of a planar DBTD since the cylindrical waves behave more like plane waves.

Oscillation in the transmission spectrum affects the I-V characteristics of the CDBTD. Figure 7.10 plots the I-V characteristics and the conductance of the GaAs- $\text{Al}_{0.3}\text{Ga}_{0.7}\text{As}$ CDBTD of Figure 7.9 with $l=0$, at 0, 100 and 300 K. The corresponding characteristics for planar DBTD are also included for comparison. Except for the oscillation in the CDBTD, both characteristics look very similar. As seen from the calculated conductance, the oscillation is relatively weak compared to the dominant resonant peaks at low temperature, and becomes dominant as the temperature increases, especially around the resonant peaks. To understand the existence of the oscillation at high temperature, one has to realize the asymmetry nature of the oscillation in the transmission spectrum. The oscillation becomes smaller as the energy of the incident electron increases.

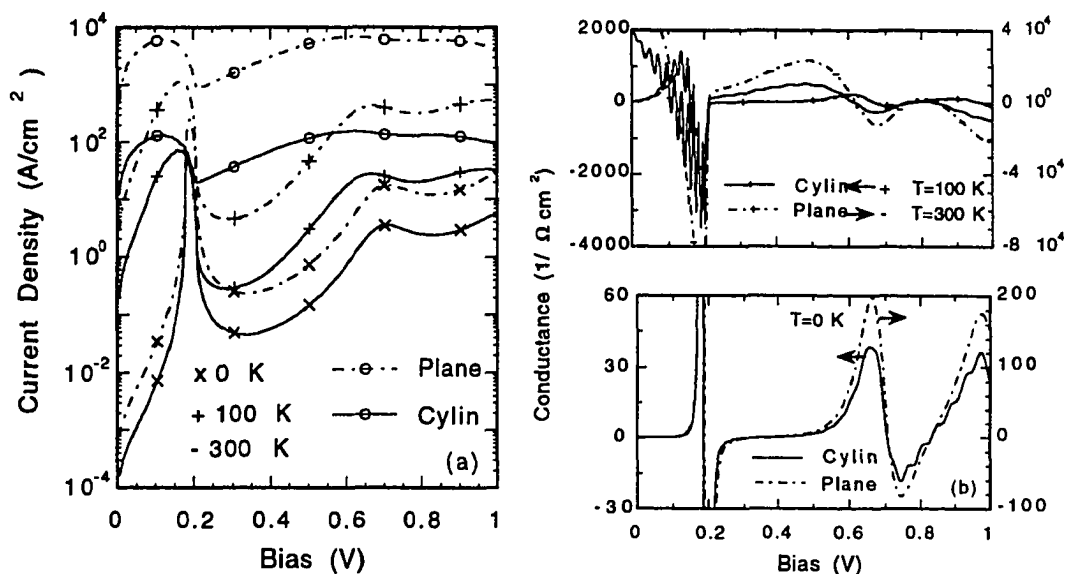


Figure 7.10. I-V characteristics (a) and conductance (b) of the GaAs-Al_{0.3}Ga_{0.7}As CDBTD of Figure 7.9 for $l=0$ state, at $T=0, 100$ and 300 K. The corresponding curves for the planar DBTD are also plotted

Therefore, a distribution of electrons results in a net oscillating current for different bias because the oscillation from low energy electrons dominates the contribution. The voltage difference of one cycle of oscillation, for the parameters studied here, is about 20 mV, which is equivalent to a temperature of 200 K. It is known that (optical and thermal) phonons and other defect scattering affect the tunneling process significantly. Therefore, these oscillations could be smeared out at high temperature by the phonon assisted tunneling and the collisions with defects and quasi-particles. It should be very interesting to study the effects of phonons and defects on the oscillation.

The performance of DBTD is affected by the Al concentration, which determines the barrier height. Figure 7.11 shows the I-V characteristics of the GaAs-Al_xGa_{1-x}As CDBTD of Figure 7.9 for $x=0.1$ and 0.3 , at 0 and 300 K. The wave vector in the barriers depends on the barrier height. Small value of x results in a large difference between cylindrical and plane waves, contributing to strong oscillations for low temperature when electrons mainly occupy the states below the Fermi energy. As the temperature increases, electrons spread into high energy states.

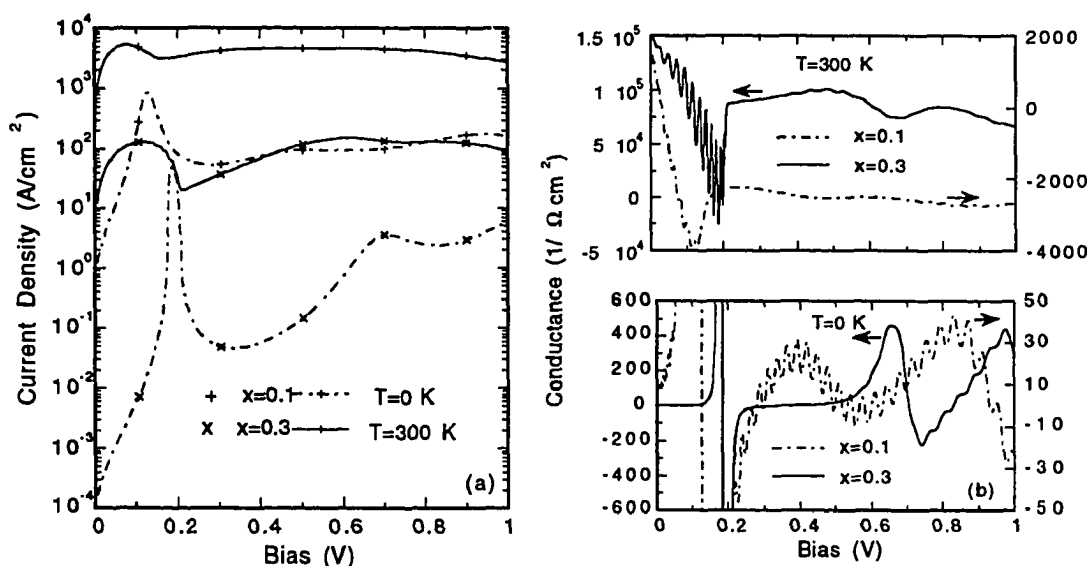


Figure 7.11. I-V characteristics (a) and conductance (b) of the GaAs-Al_xGa_{1-x}As CDBTD of Figure 7.9 with $x=0.1$ and 0.3 for $l=0$ state, at 0 and 300 K.

These electrons travel through the CDBTD with low Al concentration (small V_0 for the barriers) without the tunneling process, eliminating the oscillation. On the other hand, they must still tunnel through a high Al concentration (large V_0 for the barriers) CDBTD, and the oscillation remains.

The I-V characteristics of a DBTD are also affected by the well width and barrier thickness. Increasing the barrier thickness generally reduces current density because of the decreasing of the electron tunneling probability. In the case of a CDBTD, oscillations in the I-V characteristics become weak accordingly. The change of the well width, on the other hand, does not affect the oscillation significantly. Therefore, thin barriers are desired for large oscillations. In planar DBTD fabrication, thin barriers are achieved by decreasing the growth time. For a CDBTD, imperfections of growth techniques and the inherent crystal symmetry impose difficulties in controlling the geometry. A number of atomic layers is needed to compensate these effects and a large well width is preferred as it affects the oscillation less.

The most important parameter of the structure is, perhaps, the radius of the first barrier, ρ_e . Small ρ_e leads to a large difference between cylindrical and plane waves, resulting in large oscillations. However, as the size of the device becomes small, quantization becomes very

important. Typical length of this effect is tens of nanometer for semiconductor devices. In addition to the quantization in the radial direction as the device becomes smaller, the charging effects, e.g. Coulomb blockade, could also affect the oscillation significantly. The capacitance of the proposed CDBTD per unit length can be found in standard electromagnetic textbook as $2\pi\epsilon_0\epsilon_r / \ln(b/a)$, with a and b being the inner and outer radius of the contacts. In our case, R_1 and R_2 are the boundaries. For a $10\ \mu\text{m}$ long cylinder with R_1 and R_2 being 1000 and $5500\ \text{\AA}$, the capacitance is about $4.2\ \text{fF}$. The charging energy is therefore estimated as $E_c = e^2/C = 0.04\ \text{meV}$. From the transmission spectrum of Figure 7.9, a cycle of oscillation is in the order of $1.5 \times 5 = 7.5\ \text{meV}$, which is about two orders of magnitude larger than the charging energy. Therefore, the charging effects would not affect the oscillation in the CDBTD significantly for structures more than $1000\ \text{\AA}$ in size.

Figure 7.12 shows the I-V characteristics of a CDBTD at 0 and $300\ \text{K}$, with $\rho_c = 1000$ and $5000\ \text{\AA}$. It is seen that the amplitude of the oscillation decreases as ρ_c increases which is the result of the asymptotic behavior of the cylindrical wave (more close to plane wave) and the position dependence of the amplitude and phase has now less influence than the case of small ρ_c . Meanwhile, the period of the oscillation decreases as ρ_c increases. The relationship between the

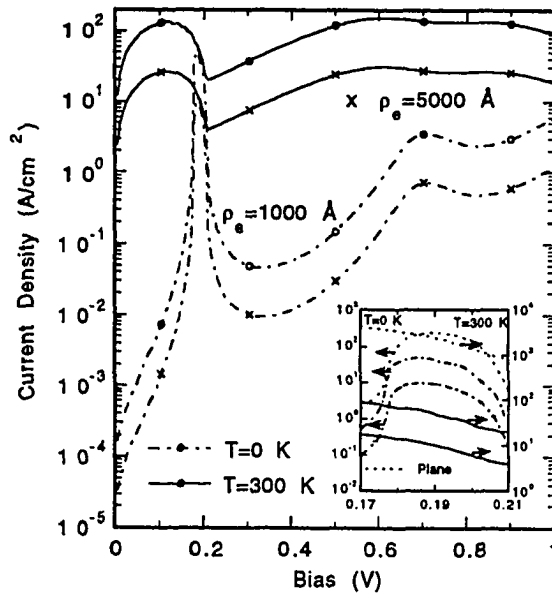


Figure 7.12. I-V characteristics of the GaAs- $\text{Al}_{0.3}\text{Ga}_{0.7}\text{As}$ CDBTD of Figure 7.9 with $\rho_c = 1000$ and $5000\ \text{\AA}$ for $l=0$ state, at 0 and $300\ \text{K}$.

period and ρ_c and other parameters such as the well width, the barrier thickness and the potential height is complicated yet to be investigated. It is very clear that ρ_c plays an important role since the small oscillation of large ρ_c is easily suppressed by effects like contact resistance and the surrounding noise. Therefore, to observe oscillations, different materials and designs which enhance the difference of the cylindrical wave and plane wave are needed.

Electrons ejected from the emitter are not limited to the $l=0, 1$ states. Oscillations associated with high l electrons can also be involved. Figure 7.13 shows the I-V characteristics of the CDBTD of Figure 7.9 for $l=0, 1, 4$ and 5 , at 0 and 300 K. It is seen that 1) odd and even l states have inverse oscillations, and 2) oscillations for high l states shift slightly relative to those of low l states with the same parity (symmetry). This behavior is very decisive in the experimental realization of the structure, and the observation of the oscillation. To avoid destructive interference, limiting the electrons to the same symmetry within a few l states is essential. It is interesting to notice that the odd l solution is ensured in the semi-CDBTD when the surface is appropriately passivated. This can be achieved by coating an insulator layer which gives an approximately infinite high barrier for the carriers.

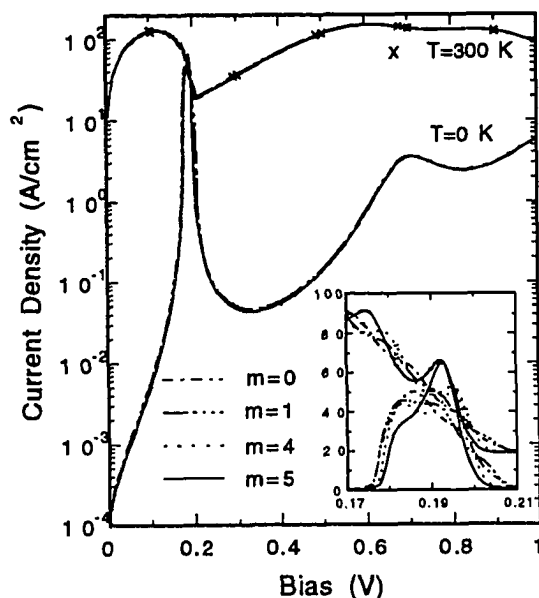


Figure 7.13. I-V characteristics of the GaAs-Al_{0.3}Ga_{0.7}As CDBTD of Figure 7.9 for $l=0, 1, 2, 4$ and 5 states, at 0 and 300 K.

The geometrical characteristics of the structure can lead to interesting devices. Figure 7.14 shows a configuration consisting of two parallel semi-CDBTD. These two parallel semi-CDBTD are electrically connected by a common terminal. Here, we assume again that the thermalization of the carriers at terminals is fast and a uniform distribution of carriers at the surfaces of the terminals is always maintained. Because of the characteristics of the cylindrical geometry, an effective potential difference is induced for the particle waves traveling inward and outward. As the current conservation requires the total amount of current passing through all the terminals being zero, the current of the common terminal is the net difference of the currents that flow through the two half CDBTD. We can therefore calculate the net current by Eq. (7.21) for the CDBTD under different bias configuration.

Figure 7.15 plots the I-V characteristic of the common terminal at 0 and 100 K for $l=1$. Other parameters used are those similar to those of Figure 7.9 except the radius of the first barrier, $\rho_e=2500 \text{ \AA}$, and the Al concentration, $x=0.1$. It is seen that the current of the common terminal displays non-zero net current, especially around the resonant peaks. Similar behavior is obtained for high l states. Therefore, for a general case where the actual wavefunction of the carrier is the superposition of different l , the strong transition of the current could still exist. Since the position dependence of the cylindrical wave is partially compensated, it is seen that the oscillation is relatively small compared to the case when only one CDBTD is considered.

The characteristics for this device might lead to potential applications in fast digital

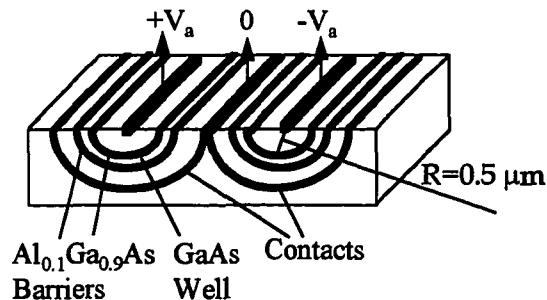


Figure 7.14. Physical structure of the devices which has three terminals and consists of two identical semi-CDBTD.

electronic circuits as the change of the current clearly defines two states. One distinguished characteristic of the device is that common existing problems in a planar DBTD, such as phonon and defect scattering at high temperature, may be reduced. It is known that phonons can affect I-V characteristics of DBTD by the phonon-assistant tunneling, which widens the resonant peaks in I-V characteristics and reduces the peak-valley ratio. If two different planar DBTD's are connected, one also gets effective difference in transmission and expects similar characteristics as Figure 7.15. However, one needs to know the difference of these planar DBTD's in order to get a good operation. The most serious problem for the planar structure is that two different processes are required to achieve different planar DBTD's. In the present device, on the contrary, two identical CDBTD's are required and therefore only one process is needed. As long as the thermalization at terminals is fast enough to randomize the carriers, the CDBTD's will have similar phonon effects. When one also recalls the fact that I-V characteristics of the new device originates from different tunneling processes induced by the structural asymmetry, one would believe that the temperature will have less effects on the new device. Other elastic scattering processes could mostly mix different l states, and the net current is not affected since the characteristics of the device are similar

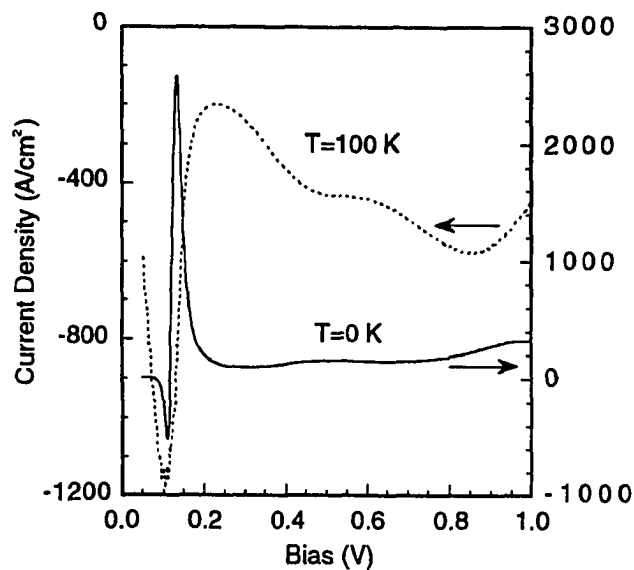


Figure 7.15. I-V characteristics of the common terminal for the device of Figure 7.14.

for all ℓ . This is very important in realizing the operation of many quantum effect devices not only at low temperature, but also at room temperature. It is known that devices based on quantum phenomena are accurate and fast. But they are difficult to maintain at high temperature. By utilizing some symmetry properties, which in principle are independent of the temperature, quantum phenomenon devices, or the so called functional devices, could be achieved more easily.

Tunneling time in cylindrical barriers

Tunneling time is of increasing importance as the size of semiconductor devices, based on quantum tunneling, become smaller and smaller. To define a tunneling time, one faces the following difficulties: 1) the nonexistence of a unique quantum-mechanical operator that gives a time as its expectation value; 2) limits imposed by the uncertainty principle; 3) the fact that a measurement of time may depend on the particular way the measurement was performed. Despite these fundamental difficulties, however, indirect methods are proposed to measure the tunneling time. Among them are the phase delay [70], dwell time [71], Büttiker-Landauer time [72], Lamor time [73], complex interaction times [74], and the group velocity time [75]. The agreement among these times is poor. Experimentally, tunneling time has been measured by the scanning tunneling electron microscope [76], dynamic polarization surface charge [77], metastable states [78], and time-resolved photoluminescence [79].

In a recent study [80], Büttiker-Landauer traversal times have been calculated for single and double barriers with cylindrical geometry. In what follows, the detail of this study will be presented. Figure 7.16 shows a schematic that was used to physically explain the meaning of Büttiker-Landauer traversal time by modulating the incident wave [81].

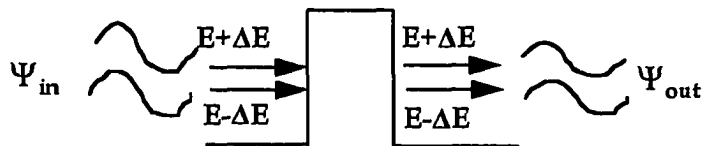


Figure 7.16. Schematic for the Büttiker-Landauer traversal time by the incident wave modulation.

The modulated incident wavefunction by two different energies and wave vectors is

$$\psi_{in} = \left\{ H_m^{(2)} \left[(k_\rho + \delta k_\rho) \rho \right] \exp \left[-\frac{i\Delta E t}{\eta} \right] + H_m^{(2)} \left[(k_\rho - \delta k_\rho) \rho \right] \exp \left[\frac{i\Delta E t}{\eta} \right] \right\} \exp \left[-\frac{iEt}{\eta} \right], \quad (7.24)$$

which basically consists of a modulation part with a frequency $\Delta E / t$ for small ΔE . The outgoing wavefunction is

$$\begin{aligned} \psi_{out} = \exp \left[-\frac{iEt}{\eta} \right] & \left\{ T(E + \Delta E) H_m^{(2)} \left[(k_\rho + \delta k_\rho) \rho \right] \exp \left[-\frac{i\Delta E t}{\eta} \right] \right. \\ & \left. + T(E - \Delta E) H_m^{(2)} \left[(k_\rho - \delta k_\rho) \rho \right] \exp \left[\frac{i\Delta E t}{\eta} \right] \right\}, \end{aligned} \quad (7.25)$$

where $T(E)$ is the complex transmission coefficient for the incoming wave with energy E . For small energy difference, the outgoing wavefunction can be approximated as

$$\begin{aligned} \psi_{out} \approx T(E) \psi_{in} + \Delta E \frac{\partial T}{\partial E} & \left\{ H_m^{(2)} \left[(k_\rho + \delta k_\rho) \rho \right] \exp \left[-\frac{i\Delta E t}{\eta} \right] - H_m^{(2)} \left[(k_\rho - \delta k_\rho) \rho \right] \exp \left[\frac{i\Delta E t}{\eta} \right] \right\} \\ & \exp \left[-\frac{iEt}{\eta} \right]. \end{aligned} \quad (7.26)$$

The time that the wave spends in the barrier compared to the modulation time, a natural time scale, should be proportional to the ratio of the coefficients in Eq. (7.26), or

$$\frac{\tau(E)}{\eta / \Delta E} \sim \frac{\Delta E \partial T(E) / \partial E}{T(E)}, \quad (7.27)$$

which yields

$$\tau_{BL}^E = \eta \left| \frac{d \ln T(E, V_0)}{dE} \right|. \quad (7.28)$$

The second traversal time is obtained by physically modulating the barrier height in time and thus a clock is introduced. Figure 7.17 shows the physics involved. As the barrier is modulated by an external force with frequency of ω , the reflected and transmitted wave will consist of wavefunction of energy $E \pm \eta\omega$. The transmissions for an opaque barrier ($k_0 d \gg 1$) for those energies are

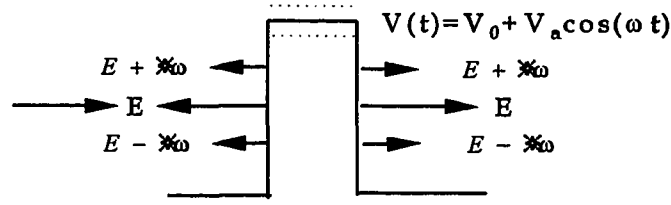


Figure 7.17. Schematic for the Büttiker-Landauer traversal time by the barrier modulation.

$$T_{\pm} = T(E \pm \eta\omega) = (V_a / 2\eta\omega)^2 \left(\exp\left[\pm \frac{\omega md}{\sqrt{(V_0 - E) / 2m}}\right] - 1 \right)^2 T(E). \quad (7.29)$$

There is an interesting quantity, called asymmetry function, which can be defined as

$$F(\omega) = \frac{T_+ - T_-}{T_+ + T_-} \xrightarrow{kd \gg 1} \tanh(\omega md / \sqrt{(V_0 - E) / 2m}). \quad (7.30)$$

The quantity in the bracket has a unit of time which is called as the characteristic time

$$t = \frac{md}{\sqrt{(V_0 - E) / 2m}}. \quad (7.31)$$

If one takes a look at the limitation of Eq. (7.29), one finds

$$\lim_{\omega \rightarrow 0} T_{\pm} = \left(\frac{V_a t}{2\eta} \right)^2 T(E), \quad (7.32)$$

where t is considered as a tunneling time. In general [82], the expression is

$$\tau(V) = \eta \left| \frac{d \ln T(E, V_0)}{dV_0} \right|. \quad (7.33)$$

Eq. (7.28) and Eq. (7.33) are to be used to calculate the tunneling time. The transmission coefficients are obtained by the transfer matrix method as discussed before. The material parameters are those used previously.

Figure 7.18 shows the traversal times, $\tau(E)$ and $\tau(V)$ for incident wave and barrier modulations, of a 100 Å $\text{Al}_x\text{Ga}_{1-x}\text{As}$ single cylindrical barrier embedded in GaAs buffer as a function of the incident energy (in the unit of the barrier height V_0) for the lowest order

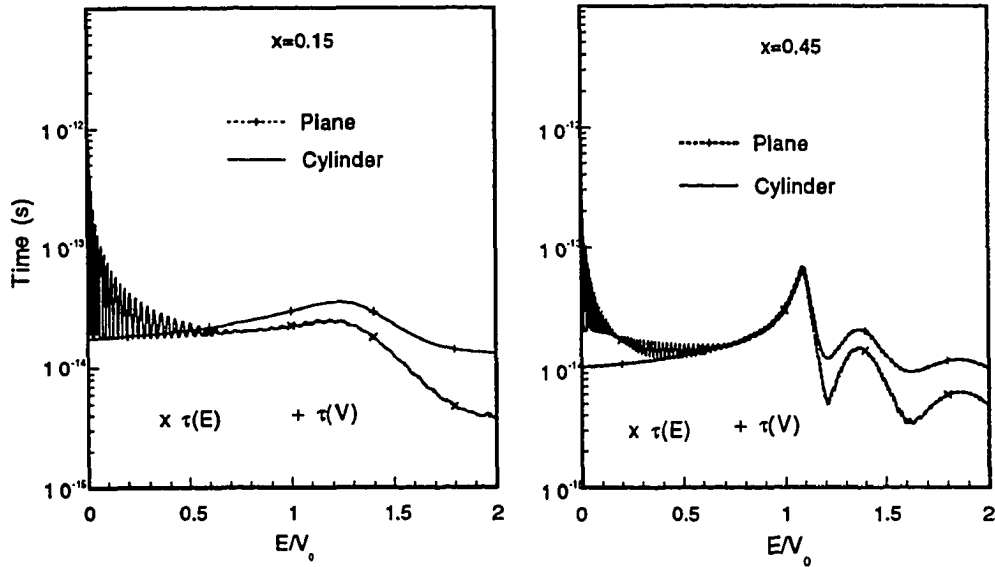


Figure 7.18. Traversal times, $\tau(E)$ and $\tau(V)$ for incident wave and barrier modulations, of a 100 Å cylindrical $\text{Al}_x\text{Ga}_{1-x}\text{As}$ barrier as a function of the incident energy. The planar barrier cases are also plotted for comparison.

traveling wave ($H_0^{(2,1)}(k\rho)$). Two Al concentrations, 0.15 and 0.45, are presented. The radius of the barrier, r_0 , is 2500 Å. For comparison, the traversal times of a planar barrier with same parameters are also plotted. It is seen that $\tau(E)$ of the cylindrical barrier oscillates as a function of the incident energy. The oscillation is very strong for low incident energy. This is due to the strong difference between plane and cylindrical waves for small argument, corresponding to low incident energy. From the figure, it is also seen that the period of the oscillation is small for low incident energy and becomes large as the incident energy increases. This corresponds to the fact that the cylindrical wave approaches the plane wave as the argument becomes large, or high incident energy. It is quite interesting as well to notice that a beat type behavior is seen in the oscillation as the barrier height increases.

While the traversal times obtained by modulating the incident wave in the cylindrical barrier oscillate as a function of the incident energy, the oscillation is negligible small in the traversal time obtained by modulating the barrier height. From the figure, $\tau(V)$ of the

cylindrical barrier is almost identical to that of the planar barrier. If we recall the definition of the traversal times, the phase of the incident wave at the surface of the barrier and its evolution through the barrier are very important to the traversal times. When one modulates the incident wave, the phase of the wave is modulated throughout the whole structure, resulting in noticeable oscillation. For barrier height modulation, however, the phase of the incident wave is only modulated in the barrier and this change of phase is not significant since the wave in the barrier is evanescent for incident energy less than the barrier height, and approaches to plane wave for incident energy larger than the barrier height as the argument of the cylindrical wave is large now. Correspondingly, the oscillation is negligible small.

Figure 7.19 shows the traversal times, obtained by modulating the incident wave and barriers, of a cylindrical $\text{Al}_x\text{Ga}_{1-x}\text{As-GaAs-Al}_x\text{Ga}_{1-x}\text{As}$ double-barrier resonant tunneling (DBRT) structure as a function of the incident energy (in the unit of the barrier height V_0) for the lowest order traveling waves ($H_0^{(2,1)}(k\rho)$). In the calculation for barrier modulation, it is assumed that barriers are modulated simultaneously. For comparison, we also plot the

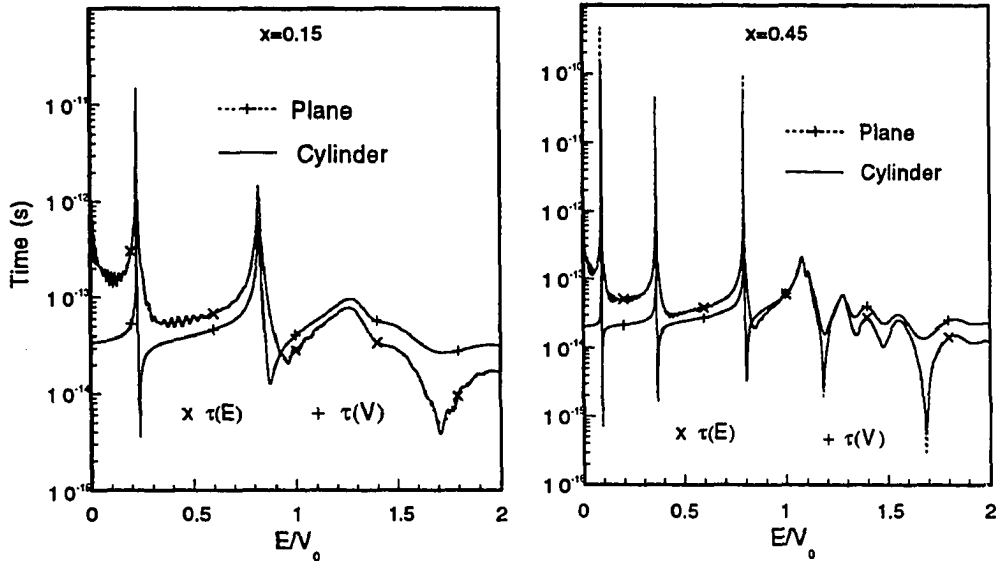


Figure 7.19. Traversal times, $\tau(E)$ and $\tau(V)$ for incident wave and barrier modulations, of a cylindrical 50-100-50 Å $\text{Al}_x\text{Ga}_{1-x}\text{As-GaAs-Al}_x\text{Ga}_{1-x}\text{As}$ DBRT as a function of the incident energy. The planar structure are also plotted for comparison.

traversal times for the corresponding planar structure. The well width and barrier thickness are 100 and 50 Å, respectively. The Al concentrations are 0.15 and 0.45, and the radius of the first barrier, r_0 , is 2500 Å. We see that oscillation appears again in the traversal time obtained by modulating the incident wave, and it is very strong for low incident energy and around the valleys. In the neighborhood of the resonant tunneling peaks, the oscillation is smeared out by the strong peaks. The traversal times obtained by modulating the barrier height do not show noticeable oscillation, similar to the case of single barrier. As the barrier height increases, the beat behavior is seen again, especially at low incident energy and valleys.

We now discuss the significance of the present findings. It is known that the consistency of the tunneling times obtained by various methods is poor, especially for some extreme cases such as low incident energy and incident energy approaching barrier height. Since real experiments are always performed on a spectrum, tunneling times have real meaning only when they are averaged by the spectrum, which may include correlation too. As devices and systems become smaller, spectra associated with these systems are narrowing. Meanwhile, if the temperature of the system, for example a doped semiconductor-metal interface or a double barrier resonant tunneling diode, is kept low enough, the dephasing processes such as the collisions with phonons and defects are suppressed by the quantum phenomena. If the tunneling times of the cylindrical barriers are measured under these conditions, the results can be used to distinguish the correct tunneling time. It is also noticed that the period of the oscillations in the traversal times of present cylindrical structures is about $10^{-2} \cdot V_0$, which is about 1 meV. Therefore, a temperature less than 10 K is required for the observation of such oscillations.

Analog systems in electromagnetism

The features occurring in CQW demands small structures, in the order of 0.5 μm. They are not easy to fabricate. Therefore, analog problems, the transmission of electromagnetic waves in dielectric layer systems with cylindrical geometry, such as single dielectric layer, double-barrier resonant tunneling and multiple period Bragg reflector systems,

have been studied by the author [83]. Interesting features were demonstrated in the transmission spectra, due to the coherence of the propagation waves associated with this geometry. In particular, an increase of the resolution power (sharper transmission peaks) in the double-barrier resonant tunneling system is demonstrated in the cylindrical structures compared to that of the planar structure. Universal behavior, that the transmission at zero frequency limit decreases substantially as the propagating wave changes from plane to cylindrical wave, has been shown in the spectra of these systems. Potential applications in reducing the radiation energy loss for transferring large density alternative current were proposed. These studies are out of the scope of this project. Therefore, the interested reader is recommended to the original article.

8. CONCLUSIONS

Fundamental properties of quantum well structures with a non-traditional geometry, cylindrical geometry, have been studied theoretically. General iteration method and transfer matrix formalism are developed to study the structures. It is shown that CQWs display interesting features that originated from the specific symmetry of the structure. The electronic and optical properties can be changed dramatically by the utilization of a magnetic field. The applications of the new structure include the resonant tunneling devices and *in-situ* tunable semiconductor quantum well laser. It is also proposed quantum devices that operating on the basic symmetry of the structure could lead to a performance that is less sensitive to the thermal effect. The study is of fundamental importance to the basic knowledge of quantum well structures.

GENERAL CONCLUSIONS

To conclude, a few further developments of the subjects studied in this thesis could be mentioned. As described in Part I, the structure proposed in this study and the phenomena observed could be used by the industry for a better product. To provide another direct confirmation to the phenomena, one is suggested to perform structural characterizations of the material of these devices with different template layers. The improvement of the devices in this study, by a better design which utilize the inherent properties of the materials, could be explored further, especially in conjunction with tandem structures.

One ought not be discouraged by the theoretical nature of the structures proposed in Part II. Nano structure physics, including some biological materials, is currently of great interest to the researchers and industries as well. A device that eventually operates on the physical properties of a single molecular is still a challenge ahead of us. Once the scale of the key components is reduced to the nanometer range, a potential revolution will happen. The search for a proper technique and material for nano structures is tough but a must. The study performed in this project provides new information. It also opens a door to further search for useful applications based on particular geometrical structure. In its infant stage still, this subject has yet to be explored. For example, a complete study of the lasing action in the structure would be most interesting. This task is not easy as the effects of the exciton need be addressed simultaneously, which is also a new subject itself.

REFERENCES

- 1) R.C. Chittick, J.H. Alexander, and H.F. Sterling, *J. of Electrochemical Society* **116**, 77 (1969); P.G. LeComber and W.E. Spear, *Phys. Rev. Lett.* **25**, 509 (1970).
- 2) D.E. Carlson and C.R. Wronski, *Appl. Phys. Lett.* **28**, 671 (1976).
- 3) W.E. Spear and P.G. LeComber, *Solid State Commun.* **17**, 1193 (1975).
- 4) Y. Hamakawa, H. Okamoto, and Y. Tawada, *Int. J. Solar Energy* **1**, 125 (1982).
- 5) A. Catalano, R.V. D'Alello, J. Dresner, B. Faughnan, A. Firester, J. Kane, H. Schade, Z.E. Smith, G. Schwartz, and A. Triano, "Attainment of 10% Conversion Efficiency in Amorphous Silicon Solar Cells", *Proceedings of the 16th IEEE Photovoltaic Specialist Conference (IEEE, New York, 1982)*, pp. 1421-1422.
- 6) Catalano, U.S. Patent #4,782376
- 7) M.S. Bennett and K. Rajan, "Stability of Multi-Junction a-Si Solar Cell", *Proceedings of the 20th IEEE Photovoltaic Specialist Conference (IEEE, New York, 1988)*, pp. 67-72.
- 8) D.L. Staebler and C.R. Wronski, *Appl. Phys. Lett.* **31**, 292 (1977).
- 9) S.R. Eliot, *Philos. Mag.*, **B39**, 349 (1979); H. Dersch, J. Stuke, and J. Beichler, *Appl. Phys. Lett.* **38**, 456 (1980); M. Stutzmann, W.B. Jackson, and C.C. Tsai, *Phys. Rev. B* **32**, 23 (1985).
- 10) V.L. Dalal, E.X. Ping, S. Kaushal, M.K. Bhan, and M. Lenard, *Appl. Phys. Lett.* **64**, 1862 (1994).
- 11) J. Meier, R. Fluckiger, H. Keppner, and A. Shah, *Appl. Phys. Lett.* **65**, 860 (1994).
- 12) P.G. LeComber, W.E. Spear, and A. Ghaith, *Electron. Lett.* **15**, 179 (1979).
- 13) E.X. Ping, submitted to *IEEE Trans. Electron Devices*.
- 14) D. Weaire, *Phys. Rev. Lett.* **26**, 1541 (1971).
- 15) M.F. Thorpe and D. Weaire, *Phys. Rev. Lett.* **26**, 1581 (1971).
- 16) N. F. Mott and E.A. Davis, *Electronic Processes in Non-Crystalline Materials*, (Oxford University Press, Oxford, 1979).

- 17) R.A. Street, Hydrogenated Amorphous Silicon, (Cambridge University Press, Cambridge, 1991).
- 18) W. Luft and Y.S. Tsuo, Hydrogenated Amorphous Silicon Alloy Deposition Processes, (Marcel Dekker, New York, 1993).
- 19) C.R. Wronski, B. Abeles, T. Tiedie, and G.D. Cody, *Solid State Comm.* **44**, 1423 (1982).
- 20) S.M. Sze, Physics of Semiconductor Devices, 2nd Ed. (John Wiley & Sons, New York, 1981).
- 21) J.H. Thomas, III and A. Caralano, *Appl. Phys. Lett.* **43**, 101 (1982).
- 22) V.L. Dalal, M. Leonard and J. Booker, *Proc. 18th IEEE Photovoltaic Conf.*, 837 (1985).
- 23) V. Dalal and E.X. Ping, " Influence of light spectrum on high-intensity degradation of a-Si solar cells ", to appear in *Prog. in Photovoltaic*.
- 24) Goldstein, C.R. Dickson, I.H. Campbell and P.M. Fauchet, *Appl. Phys. Lett.* **53**, 2672 (1988).
- 25) J.C. Knights and R.A. Lujan, *Appl. Phys. Lett.* **35**, 244 (1979).
- 26) O. Kuboi, *Janpanes J. Appl. Phys.* **20**, L783 (1981).
- 27) J. Kane, H.P. Schweizer, and W. Kern, *Thin Solid Films* **29**, 155 (1975).
- 28) P. Nath, R.F. Bunshah, B.M. Basol, and O.M. Staffsud, *Thin Solid Films* **72**, 463 (1980); I. Hamberg, A. Hjortsberg, and C.G. Granqvist, *Appl. Phys. Lett.* **40**, 362 (1981).
- 29) J.C.C. Fan, F.J. Bachner, and G.H. Foley, *Appl. Phys. Lett.* **31**, 773 (1977).
- 30) M. Hack and M. Shur, *J. Appl. Phys.* **58**, 1985, pp.997-1019.
- 31) G.D. Cody, in *Semiconductors and Semimetals*, vol. 21 Part B, Chapter 2 (R.L. Willardson and A.C. Beers eds.) (Academic Press, New York, 1984).
- 32) J. Bardeen and W.H. Brattain, *Phys. Rev.* **74**, 230 (1948); W. Shockley, *Bell Syst. Tech. J.* **28**, 435 (1949).
- 33) R. N. Hall, G. E. Fenner, J. D. Kingsley, T.J. Soltys, and R. O. Carlson, *Phys. Rev.*

- Lett. **9**, 366 (1962); M. I. Nathan, W. P. Dumke, G. Burns, F. H. Dills, and G. Lasher, *Appl. Phys. Lett.* **1**, 62 (1962); T. M. Quist, R. J. Keyes, W. E. Krag, B. Lax, A. L. McWhorter, R. H. Rediker, and H. J. Weiger, *Appl. Phys. Lett.* **1**, 91 (1962).
34. N. G. Basov, B. M. Vul, and Y. M. Popov, *Zh. Eksp. Theo. Fiz.* **37**, 587 (1959), *Soviet Phys. JETP* **10**, 416 (1959); W. P. Dumke, *Phys. Rev.* **127**, 1559 (1962).
35. F. Bloch, *Z. Physik* **52**, 535 (1928).
36. R. Kronig and W. G. Penney, *Prog. Roy. Soc. A* **130**, 499 (1931).
37. M.L. Cohen and J.R. Chelikowsky, **Electronic Structure and Optical Properties of Semiconductors** (Springer-Verlag, Berlin, 1988).
38. L. Esaki and R. Tsu, *IBM Res. Note*, RC-2418, Mar. 1969; L. Esaki and R. Tsu, *IBM J. Res. Develop.*, pp. 61-65, Jan. 1970.
39. L. Esaki, L.L. Chang, W.E. Howard, and V.L. Rideout, *Proc. 11th Int. Conf. Phys. Semiconductors*, Warsaw, Poland, 1972, edited by the Polish Academic of Science (PWN-Polish Scientific Publishers, Warsaw, Poland), pp. 431-436.
40. L. Esaki, *IEEE J. Quan. Elec.* **QE-22**, 1611 (1986); C. Weisbuch and B. Vinter, **Quantum Semiconductor Structures: Fundamentals and Applications**, (Academic Press, San Diego, 1991).
41. L.L. Chang, L. Esaki, and R. Tsu, *Appl. Phys. Lett.* **24**, 593 (1974); L. Esaki and L. L. Chang, *Phys. Rev. Lett.* **33**, 495 (1974).
42. R. Dingle, W. Wiegmann, and C.H. Henry, *Phys. Rev. Lett.* **33**, 827 (1974); R. Dingle, A.C. Gossard, and W. Wiegmann, *Phys. Rev. Lett.* **34**, 1327 (1975).
43. S. Schmitt-Rink, D.S. Chemla, and D.A.B. Miller, *Advances in Physics* **38**, 89 (1989).
44. K. von Klitzing, G. Dorda, and M. Pepper, *Phys. Rev. Lett.* **45**, 494 (1980); D.C. Tsui, H.L. Stormer, and A.C. Gossard, *Phys. Rev. Lett.* **48**, 1559 (1982).
45. R. Tsu, L.L. Chang, G.A. Sai-Halasz, and L. Esaki, *Phys. Rev. Lett.* **34**, 1509 (1975).
46. E. Kapon, M.C. Tamargo, and D.M. Hwang, *Appl. Phys. Lett.* **50**, 347 (1987); B.E. Maile, A. Forchel, R. Bemann, A. Menschig, H.P. Meier, and D. Grutzmacher, *J. Vac. Sci. Technol. B* **6**,2308 (1988).

47. Keji Yada, *Acta Cryst.* vol. A27, pp. 659-664, Nov. 1971; V.N. Bogomolov, *Usp. Fiz. Nauk* vol. 124, pp. 171-182, Jan. 1978.
48. V.V. Poborchii, *Japanese J. Appl. Phys*
49. H.C. Gasey and M.B. Panish, **Heterostructure Lasers** (Academic, New York, 1978), part A; **Numerical Data and Functional Relationship in Science and Technology**, O. Madelung ed. Group III, 17, (Springer, Berlin, 1982).
50. S. White and L.J. Sham, *Phys. Rev. Lett.* 47, 879 (1981); G. Bastard, *Phys. Rev. B* 24, 5693 (1981); G. Bastard, *Phys. Rev. B* 25, 7584 (1982); M. Altarelli, *Phys. Rev. B* 28, 842 (1983); M.F.H. Schuurmans and G.W. Hooft, *Phys. Rev. B* 31, 8041 (1985); Y.C. Chang and J.N. Schulman, *Appl. Phys. Lett.* 43, 536 (1983).
51. G. Bastard, **Wave Mechanics Applied to Semiconductor Heterostructures**, (Edition de Physique, Les Ulis, 1988).
52. H.L. Stormer, R. Dingle, A.C. Gossard and W. Wiegmann, *Appl. Phys. Lett.* 44, 665 (1978).
53. D.L. Rode, **Semiconductors and Semimetals**, (R.L. Willardson and A.C. Beers eds.) vol. 10 Chapter 2 (Academic Press, New York, 1975)
54. R. Tsu and L. Esaki, *Appl. Phys. Lett.* 22, 562 (1973).
55. J. Shah, *IEEE J. Quantum Electron.* QE-22, 1728 (1986).
56. H.L. Stormer, K. Baldwin, A.C. Gossard and W. Wiegmann, *Phys. Rev. Lett.* 44, 1062 (1984).
57. A.N. Lepore, H.M. Levy, R.C. Tiberio, P.J. Tasker, H. Lee, E.D. Wolf, L.F. Eastman, and E. Kohn, *Electron. Lett.* 24,364 (1988).
58. T.C.L.G. Sollner, W.D. Goodhue, P.E. Tannenwald, C.D. Parker, and D.D. Peck, *Appl. Phys. Lett.* 43, 588 (1983); T.C.L.G. Sollner, *Phys. Rev. Lett.* 59, 1622 (1987).
59. A. Yariv, **Quantum Electronics**, 3rd Edition (John Wiley & Sons, New York, 1989).
60. B. Levin, K.K. Choi, C.G. Bethea, J. Walker, and R.J. Malik, *Appl. Phys. Lett.* 50, 1092 (1987).
61. D.A. Miller, D.S. Chemla, T.C. Damen, A.C. Gossard, W. Wiegmann, T. Wood, and

- C.A. Burrus, *Appl. Phys. Lett.* **45**, 13 (1984).
62. M. Masale, N. C. Constantinou, and D. R. Tilley, *Phys. Rev. B* **46**, 15432 (1992).
63. E.X. Ping and V. Dalal, *J. Appl. Phys.* **76**, 2547 (1994).
64. M. Abramowitz and I. A. Stegun eds., **Handbook of Mathematical Functions**, (Dover Publications, New York, 1972).
65. R.C. Miller, A.C. Gossard, D.A. Kleinman, and O. Munteanu, *Phys. Rev. B* **29**, 3740 (1984); R.C. Miller, D.A. Kleinman, and A.C. Gossard, *Phys. Rev. B* **29**, 7085 (1984).
66. V.J. Goldman, D.C. Tsui and J.E. Cunningham, *Phys. Rev. Lett.* **58**, 1256 (1987).
67. E.X. Ping and V. Dalal, *J. of Appl. Phys.* **73**, 5289 (1993).
68. E.X. Ping, *IEEE J. Quan. Elec.* **31**, (1995).
69. W.R. Frensley, *Phys. Rev. B* **36**, 1570 (1987); N.C. Kluksdhl, A.M. Krivan, and D.K. Ferry, *Phys. Rev. B* **39**, 7720 (1989); N.S. Wingreen, K.W. Jacobson, and J.M. Wilkins, *Phys. Rev. Lett.* **61**, 1396 (1988); J. Leo and A.H. MacDonald, *Phys. Rev. Lett.* **64**, 817 (1990).
70. L. Eisenbud, Dissertation (Princeton University, 1948, unpublished); E.P. Wigner, *Phys. Rev.* **98**, 145 (1955); D. Bohm, Quantum Theory, (New York, Prentice-Hall, 1951), pp. 257-261.
71. M. Büttiker, *Phys. Rev. B* **27**, 6178 (1983); C.R. Leaven and G.C. Aers, *Phys. Rev. B* **39**, 1202 (1989).
72. M. Büttiker and R. Landauer, *Phys. Rev. Lett.* **49**, 1739 (1982); M. Büttiker and R. Landauer, *Phys. Scripta* **32**, 429 (1985).
73. A. I. Baz', *Sov. J. Nucl. Phys.* **4**, 182 (1967); **5**, 161 (1967); V.F. Rybachenko, *Sov. J. Nucl. Phys.* **5**, 635 (1967).
74. D. Sokolovski and L. M. Baskin, *Phys. Rev. A* **36**, 4604 (1987).
75. A. Khondker, M. Khan, and A. Anwar, *J. of Appl. Phys.* **63**, 5191 (1988); A. Anwar, A. Khondker, and M. Khan, *J. of Appl. Phys.* **65**, 2761 (1989).
76. P. H. Cutler, T. E. Feuchtwang, Z. Huang, T. T. Tsong, H. Nguyen, A. A. Lucas, and T. E. Sullivan, *J. Physique C* **6**, 101 (1987); P. H. Cutler, T. E. Feuchtwang, T. T.

- Tsong, H. Nguyen, and A. A. Lucas, *Phys. Rev. B* **35**, 7774 (1987).
77. M. Jonson, *Solid State Comm.* **33**, 743 (1980); P. Gueret, E. Marclay, and H. Meuer, *Solid State Comm.* **68**, 977 (1988); P. Gueret, E. Marclay, and H. Meuer, *Appl. Phys. Lett.* **53**, 1617 (1988).
78. P. J. Price, *Phys. Rev. B* **36**, 1314 (1987).
79. M. Tsuchiya, T. Matsusue, and H. Sakaki, *Phys. Rev. Lett.* **59**, 2356 (1987).
80. E.X. Ping, *J. of Appl. Phys.* **76**, 2547 (1994).
81. M. L. Haggmann, *Appl. Phys. Lett.* **62**, 199 (1993).
82. C.R. Leavens and G.C. Aers, *Solid State Comm.* **63**, 1107 (1987).
83. E.X. Ping, *J. of Appl. Phys.* **76**, 7188 (1994).

ACKNOWLEDGMENTS

First of all, I thank Prof. Vikram Dalal, my major supervisor, for giving me the opportunity to work in MRC four years ago and his guidance throughout the work. I also thank my committee members, Profs. Stanley G. Burns, Hsung-Cheng Hsieh, Joseph Shinar, Gary Tuttle, and Dr. Howard Shanks for their time and help.

I am grateful to the help I obtained from Dr. Ralph Knox, Miss. Kay Han and Mr. Mark Lenord of a-Si:H photovoltaic group, Mr. Micheal Thomas of Iowa Thin Film Technology, and Miss Frenz Olympia of a-Si:H thin-film-transistor group.

It has been a great pleasure to work in MRC, although some long evenings and weekends could be more interesting than working on the project. I do appreciate the friends that I spent time with in MRC: Dr. Behnam Moradi, Greg Baldwin and Scott DeBoer; Mr. Nabeeh Kandanlaft, Prasad Rachepalli, Prem Chahal, Sanjeev Kasual, Tim Maxson, Abdulaziz Ahmed, Jun Xu and Francisco Martin, former and current student members of a-Si:H photovoltaic group, as well as Mr. Erick Micheal, Joe Fastenau, and Bill Liners, Miss. Chi-di Chen and Sandhya Gupta of MBE group, Jia Xia of thin film resonator group and Russ Bruhn of Microwave group.

Finally, I want to thank my parents deeply, especially my mother who was across the Pacific Ocean and joining me for a year. It is the only fear to me in this world that I may disappoint them by not working hard. My sisters, who live thousand miles away, are always there to encourage me to finish whatever I started.